ACOUSTIC EMISSION AND RELATED
DISPLACEMENTS IN LITHIUM FLUORIDE
SINGLE CRYSTALS

Thesis for the Degree of Ph. D.
MICHIGAN STATE UNIVERSITY
Robert B. Engle
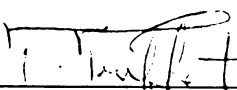1966

This is to certify that the

thesis entitled

ACOUSTIC EMISSION AND RELATED DISPLACEMENTS
IN LITHIUM FLUORIDE SINGLE CRYSTALS

presented by

Robert B. Engle

has been accepted towards fulfillment
of the requirements for

___Ph.D.___ degree in _Applied_ Mechanics

Major professor

Date_October 5, 1966___

O-169

ACOUSTIC EMISSION AND RELATED DISPLACEMENTS IN

LITHIUM FLUORIDE SINGLE CRYSTALS

By

Robert B. Engle

ABSTRACT

ACOUSTIC EMISSION AND RELATED DISPLACEMENTS IN LITHIUM FLUORIDE SINGLE CRYSTALS

by Robert B. Engle

Acoustic emission is the result of lattice vibrations caused by mechanisms that govern deformation of crystalline materials when they are stressed. Observations were made using single crystals of lithium fluoride oriented for easy-glide deformation when loaded in direct shear.

Acoustic emission pulses and displacement pulses derived from rapid step displacements were observed. The largest displacements (10×10^{-6} inches) were found to occur in coincidence with large acoustic emission pulses. Smaller displacements (20×10^{-8} inches) and acoustic emission pulses were observed to occur together, though not in coincidence, throughout the tests. Some large acoustic emission pulses had no displacements associated with them.

On the basis of these results a mechanism for the acoustic emission process is proposed, and is shown to be consistent with the observations of others who have studied acoustic emission in crystalline materials. Estimates of dislocation group velocities are made which agree with previous dislocation velocity measurements in lithium fluoride.

The proposed mechanism involves the interaction between piled-up groups of dislocations and the obstacles that cause the pile-up. The pinning interaction causes an increase in local strain energy stored in the region of the obstacle. When the driving stress on the leading dislocation, composed of the applied stress and additional stress due

to the pile-up itself, is large enough to cause breakaway and acceleration of part of the group, the local strain energy is available to excite lattice vibrations that appear as acoustic emission. A secondary emission process arises during collisions between coherent groups of moving dislocations and obstacles in their slip planes. Finally, an alternate type emission occurs at high stress levels after large plastic deformation when the stress concentrations at the leading edge of dislocation groups causes crack nucleation and propagation.

ACOUSTIC EMISSION AND RELATED DISPLACEMENTS IN

LITHIUM FLUORIDE SINGLE CRYSTALS

By

Robert B. Engle

A THESIS

Submitted to
Michigan State University
in partial fulfillment of the requirements
for the degree of

DOCTOR OF PHILOSOPHY

Department of
Metallurgy, Mechanics and Materials Science

1966

ACKNOWLEDGMENT

I wish to thank Dr. Clement A. Tatro, who interested me in this project, and Dr. Terry Triffet, who assumed the role of major professor when Dr. Tatro went to Tulane University, for their encouragement and guidance.

I gratefully acknowledge many informative discussions with faculty and graduate students of the Department of Metallurgy, Mechanics, and Materials Science and additional support from the department.

TABLE OF CONTENTS

LIST OF FIGURES

iv

LIST OF TABLES

LIST OF APPENDICES

INTRODUCTION

The fact that tin emits sounds when it is deformed has been known for many years. Around 1930 Orowan[1] and Klassen-Nekludowa[2] investigated this phenomenon in tin, that is now associated with the formation of mechanical twins. Other researchers have reported noises occurring with deformation in metals[3,4,5]; however, no great significance was attributed to them.

In 1950 the late Joseph Kaiser[6,7] started experiments to determine if other materials produced acoustic phenomena when loaded. Tests of steel, aluminum, copper, lead, zinc, and wood revealed sub-audible acoustic pulses accompanying deformation. Each material produced a characteristic noise spectrum with amplitude and frequency distributions that correlated with the different regions of the stress-strain curve. He observed that the onset of emission occurred before the macroscopic yield point was reached, emission continued for a period of time when the load was held constant, and the emission process was irreversible. These observations led him to conclude that acoustic emission was related to plastic deformation in favorably-oriented crystals. Friction due to relative motion at crystal boundaries was suggested as the source mechanism.

Subsequent investigations have confirmed the occurrence of acoustic emission from all of the crystalline materials that Kaiser tested, and various others as well, but have associated acoustic

emission with more basic deformation mechanisms. They have not confirmed the rather detailed relationship between stress and the distributions of amplitude and frequency that Kaiser reported, but have exhibited the other characteristics that he observed.

Interest in acoustic emission as a possible tool for non-destructive testing led Professor C. A. Tatro[8, 9, 10, 11] to start investigations while he was at Michigan State University from 1956 to 1962. B. H. Schofield[12-16] at Lessells and Associates, Inc., also started research into the acoustic emission phenomenon late in 1954.

The fact that Kaiser, Tatro, and Schofield have all observed acoustic emission from every material they have tested suggests acoustic emission may itself become a research tool for deformation mechanics, if its sources can be identified and techniques for observation are refined. Both Tatro and Schofield believe the acoustic emission process is intimately related to microscopic mechanisms governing deformation of crystalline structures.

Acoustic emission observed by Schofield characteristically consists of two components: a relatively high amplitude, low frequency, burst-type which occurs randomly with long quiescent periods between bursts; and a high frequency component with smaller amplitude that is continuous in nature, appearing much as broad-band noise in electronic equipment. Both components appear in elastic and plastic regions of the stress-strain curve. Schofield's results indicate there is a minimum strain rate below which the high frequency emission is notably absent. The equipment used at

Michigan State University was capable of only very low strain rates, and the fact that no high frequency emission has been observed there is in agreement with Schofield's observations. If the strain rate is high enough, high frequency emission generally starts before the nominal elastic limit is reached, increases in amplitude as the elastic limit is reached, and then diminishes in amplitude as plastic deformation continues. The emission pulse rate is observed to increase with increasing strain rate, and the frequency spectrum apparently shifts to higher frequencies as plastic strain increases.

The burst-type emission also appears in most of the materials tested. However, the relative contribution of the burst-type is quite small when compared to the high frequency contribution above the threshold strain rate; nor can the total plastic deformation be explained on the basis of total acoustic emission for those tests made at low strain rates when the high frequency emission is not observed.

The largest group of experiments has been run on aluminum alloys and pure aluminum. Schofield[12,13], reporting on tensile tests of specimens machined from 24ST-4 aluminum, characterized the emission as being primarily of the high frequency type; initial pulses were of lower frequency with higher frequency pulses starting at higher stresses with increasing rate. Burst-type emission was present with much higher amplitude, but with much less contribution to the total pulse count. The alloy polycrystalline specimens exhibited more of the burst-type emission than single crystal specimens of pure aluminum. Tests with pure aluminum single crystals produced much the same general behavior for high frequency

emission, with some differences in character that could be related to the orientation of the crystals. The burst-type was notably absent during the early stages of deformation, but did occur during later stages of plastic deformation.

In another series of tests[14,15] single crystals of aluminum were loaded while immersed in an etchant bath so that the surface oxide film would not be a contributing factor. Crystals with the tensile axis in the (100) direction still exhibited high frequency emission in about the same amounts, though its initiation stress was shifted to a higher value. Very little burst-type was seen. On the other hand, single crystals oriented with a Schmid factor of 0.5 gave no emission to strains as high as 20%. Polycrystalline specimens with grain densities ranging from 25 to 160 grains per cm^2 were tested and gave no noticeable difference in emission from the oriented single crystals, thereby ruling out the importance of grain boundaries to the emission process as proposed by Kaiser.

Reports by Tatro[10,11] and Shoemaker[17] on 2024 T-4 aluminum specimens tested at a low strain rate give more information on the burst-type emission because the high frequency component was not present to mask its occurrence. They observed burst-type emission in the elastic range that shifted to higher frequencies with lower amplitude and faster pulse rate in the plastic range, much as the high frequency emission of Schofield; however, the peak emission was recorded before the yield point was reached.

Tests by Liptai[18,19] and Tatro[11] on specimens of 2011 T-3 aluminum were nearly the same, except emission peaks were recorded

in the plastic range. The only surface treatment that restored initial emission activity was electropolishing that removed 0.05 inches from the surface. Electropolishing combined with electron bombardment partially restored initial emission activity, but shifted its onset to higher stress levels.

R. G. Liptai[18,19], testing single crystals of aluminum with a (100) tensile axis, reported burst activity much the same as for the 2011 T-3 specimens; except the activity seemed to be enhanced in the plastic region. He found thick anodized and reacted coatings increased the acoustic activity, while electropolishing afterwards would reestablish the as-received activity of the specimen.

When testing single crystals of zinc, Schofield[13] observed burst-type emission as the salient feature of the emission spectrum. Bursts occurred immediately upon loading at low load rates. Pulse rate and amplitude increased with stress, and emission continued for a period of time if the load was held constant. High frequency emission did not become apparent until gross deformation set in and stopped immediately when the load rate was reduced to zero. The amplitude of high frequency emission increased with deformation. A crystal coated with photoelastic adhesive gave several extremely energetic bursts associated with the formation of twins, though most of the burst-type emission occurred at stresses below that commonly thought of as being required for twin formation. One bi-crystal was observed to give an energetic burst associated with a grain boundary reorientation.

Probing experiments have been run on carbon steel[8-13,17],

tin[12], brass[10,13], magnesium and 40/60 solder[10], copper and lead[13], and pure iron[16]. All were observed to produce acoustic emission.

R. T. Sedgwick[20] tested single crystals of lithium fluoride in (100) compression in the elastic stress-strain region and observed what may be another burst-type emission. Crystals with thick surface films, that tended to raise the elastic stress-strain curve, produced burst-type emission when the films were etched from the loaded crystal. Burst-type emission was also observed in the elastic region during loading for both coated and uncoated crystals. This emission exhibited a delay character by continuing for a while after each increment of load. This is characteristic of burst emission observed by others in metals.

Since the introduction of the concept of the moving dislocation in 1930 by Taylor[21], Orowan[22], and Polanyi[23], dislocation motion and interactions have played a major role in explaining the behavior of materials under load. The importance of dislocation theory in explaining the yield strength, ductility, work hardening, fatigue, and fracture of materials is recognized and supported by many experimental results. There are, however, few techniques that allow direct observation of dynamic behavior of dislocations.

The sources of the acoustic emissions observed to date in crystalline materials are still subject to debate, though all of the present interpretations have one point in common. In each case, the results are most easily interpreted as being due to the motion of groups of dislocations, possibly to the motion of single dislocations. Previously, dislocation behavior has been inferred from metallographic,

X-ray, and electron microscope studies that are inherently limited to observation of events near the surface, or sound attenuation measurements that can measure gross changes but not the details of dislocation behavior. Acoustic emission may be a phenomenon that will allow direct observation of dislocation motion.

The earlier work of Schofield[12,13,14], and the experiments of Tatro, Shoemaker, and Liptai all seem to indicate that acoustic emission is a surface phenomenon, or is controlled by the nature of the surface. Schofield's measurements on aluminum single crystals[12], for example, lead to a remarkably close, though tentative, correlation between the number of high frequency emission pulses and the number of slip lines formed at the surface. Liptai's results with coatings on aluminum[18,19] also strongly indicate that burst-type emission is due to surface effects in crystals. Both, at the time, interpreted acoustic emission to be the result of energy released when piled-up dislocations broke through the surface barrier and left the crystal, causing the formation of new surface accompanied by heat and an elastic wave. This explanation is strengthened by those experiments that investigated the effects surface treatments and films had on the character of the emission. The burst-type in aluminum was observed to increase with coating thickness[18,19]. Shot-peened 1018 steel specimens produced more activity shifted to higher stress levels[11,17]. Aluminum single crystals tested in an etchant bath produced either no emission (0.5 orientation) or high frequency emission that started at higher stress levels for (100) orientation[14,15].

Later tests by Schofield[15] on gold single crystals indicated that some emission is not a surface phenomenon. Gold was chosen

because it does not have an effective surface film. In these tests burst-type emission was much more prevalent, appeared to be partly reversible, and increased in activity with continued plastic strain. The high frequency type started immediately upon loading, peaked at about 0.08% strain, and decreased thereafter. The burst-type emission was much more energetic when specimens were annealed after a test and were then retested. In this condition the crystals had coarse-grained annealing twins in the test section. Etching away a surface layer did not restore or alter the character of the emission as it did for aluminum. Cold work of screw faces or edge faces of the 0.5 crystal did enhance the high frequency emission; and, in this case, surface etching returned the emission to normal.

These results have led Schofield to identify the burst-type emission with the formation of stacking faults in gold and the high frequency emission with the movement of dislocations in the interior of the sample.

Zinc[13] also exhibits burst-type emission which Schofield has tentatively related to the formation of stacking faults (more probably micro-twins) and, in the more energetic cases, to twin formation and grain boundary reorientations.

Schofield explained the relative lack of burst-type emission from aluminum by the fact that the energy required for the formation of stacking faults in aluminum is much higher than the energy required for the formation of stacking faults in gold or for the formation of micro-twins in zinc.

Schofield now feels the acoustic emission process is related to internal deformation processes instead of surface effects. However, in so far as surface condition effects the motion of dislocations in the interior regions, surface condition can alter the acoustic emission process.

The emission that R. Sedgwick[20] observed in lithium fluoride appeared to come from two different sources. The bursts, observed when the surface films were etched away under load, can definitely be attributed to the egress of groups of dislocations that were piled up on a slip plane due to the surface barrier. The fact that the surface coatings tended to raise the stress-strain curve led him to the conclusion that dislocations have some role to play in elastic deformation. He formulated a model depending upon the dislocation network present in the unstressed crystal to provide dislocation segments in favorably oriented slip planes that are pinned at points where they leave the planes. These segments act as Frank-Read sources which are activated by stresses too small to cause dislocations to leave the crystal, but which can contribute to deformation. Yield occurs when the force on the leading dislocation on a slip plane is large enough to cause it to leave the crystal. Back stresses would cause the sources to operate in reverse, so that the process can be thought of as a quasi-elastic one.

According to Sedgwick's model the initial acoustic emission is due to the activation of these Frank-Read sources. Sources with the longest loop length will be activated at the lowest value of stress and will continue to operate until dislocations emanating from them

become blocked and pile up in the slip plane. As stress increases the shorter sources activate. The emission due to the initial dislocation distribution should be symmetric about the activation stress required for the average loop length.

New dislocations produced can also block the operation of the original source distribution, having the effect of shifting the mean loop length to lower values. This secondary effect causes the expected distribution of effective sources to be skewed towards the shorter length, and should, therefore, produce an emission distribution that is skewed towards higher stress as was observed. This mechanism, if verified, may explain the elastic region emission observed by others.

In reviewing the data reported above, it becomes increasingly obvious that there are a multiplicity of mechanisms which can act as sources of acoustic emission. Any process involving a rapid transition between different dislocation configurations within the crystal lattice must also produce an accompanying acoustic emission. Whether or not the emission is detected would depend upon two factors. The first is the rate at which the process proceeds, and the second is the amount of energy dissipated in vibrational modes as the transition occurs.

Acoustic emission pulses have been variously identified with slip line formation, formation of stacking faults, cracking of surface films, release of piled up dislocations, action of Frank-Read sources, twinning, grain boundary reorientation, and motion of individual dislocations in the interior of the specimens. The only estimate of

displacement has been made by Schofield[13], who found that there was nearly a one to one relation between slip line formation in aluminum and the total high frequency pulse count. His estimate was based upon average values of slip line spacing, which are subject to question; these indicated that the average emission pulse corresponds to a displacement of from 50 to 150 x 10^{-8} cm and involves the motion of from 20 to 50 dislocations in aluminum. Similar estimates were made for zinc with the result that the displacement range was from 15 to 50 x 10^{-8} cm, corresponding to the motion of from 5 to 20 dislocations. A direct measurement of the displacements actually involved would greatly assist the positive identification of the acoustic emission mechanisms.

R. L. Sproull[32] has successfully used a capacitance-type transducer to measure displacements on the order of 1 Angstrom. Sproull's device is awkward for measurement of dynamic displacements, but his success indicated a capacitance transducer might provide the sensitivity required to detect small displacements related to acoustic emission. References[33,34] to an ionization transducer utilizing a capacitance sensor looked promising, and efforts were directed towards developing a displacement transducer that would allow the measurement of such small dynamic displacements. If the necessary sensitivity could be achieved, acoustic emission measurements were planned to try to correlate the emission pulses with discrete displacements in order to learn more about the phenomenon.

To identify the source or sources of acoustic emission, it is

imperative that the specimen's deformation modes be severely
limited, and that as much as possible be known about dislocation
motion in the material. Lithium fluoride is ideal for this purpose,
since so much is already known from the experiments of Gilman and
Johnston[24-31]. It is well established from their work that lithium
fluoride deforms plastically by $\{110\}$ <110> slip at room
temperature. Slip is possible on other planes only at elevated
temperature. Appropriate load geometry can limit slip to one or,
at most, two slip planes. By utilizing appropriate orientation and
load geometry to limit the possible deformation mechanisms, it
was felt that it should be easier to relate acoustic emission to
displacement.

When it became apparent that the necessary displacement
sensitivity was possible, work was started on making a direct-
shear loader that would be quiet enough for acoustic emission
studies. The objectives of the research were: first, to determine
whether or not discrete slip displacements accompany acoustic
emission; second, to determine the magnitude of the displacements
if they exist; and third, to determine whether or not acoustic
pulse height can be related to the size of such displacements.

EXPERIMENTAL PROCEDURE

The loading system shown in Figures 1, 2, and 3 was designed to provide noise-free, direct-shear loading to bar-shaped specimens. The system consists of a platform supported by two floats riding in independent water tanks. A pendulum is suspended from a frame that is mounted on the platform. The specimen under test is clamped between the pendulum and the platform. When the water level in one tank is lowered, the component of the pendulum weight down the resulting incline is applied to the crystal.

The pendulum is restrained by the specimen under load, the four support wires, and four lateral wires that prevent sideways translation and rotation about the longitudinal axis of the specimen.

The load system can be tilted to an angle of 30 degrees in ten minutes which gives a load rate of 4.5 pounds per minute. This rate is constant, due to the combined effects of the lateral restraints and the variation in water flow as the tank water level decreases.

The load is transmitted to the crystal by square steel bars (1/2 in x 1/2 in) that also hold the displacement, load, and acoustic emission transducers. Figure 4 shows the detail of the crystal clamps and load bars.

Simple beam theory predicts that bending moments in the specimen will produce a flexural stress of not more than 3.2% of the maximum shear stress or 10% of the average shear stress applied by the loader. The load on the pendulum support wires decreases as the platform tilts. This places an axial load on the specimen

13

A. Water tanks.
B. Flotation tanks.
C. Load valve.
D. Initial water level.
E. Stabilizing counterweight.
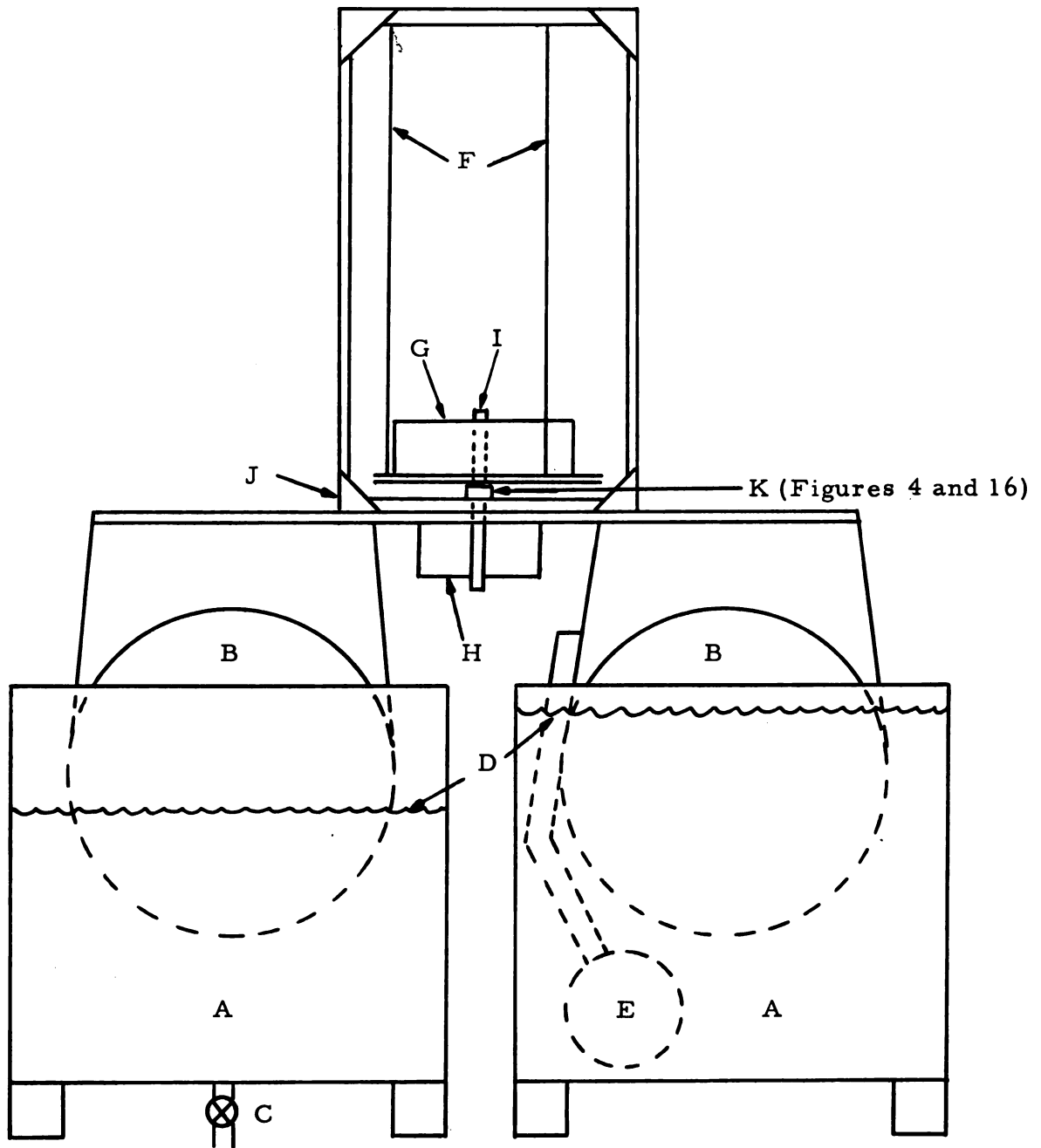
F. Pendulum support wires.
G. Pendulum weight.
H. Bottom clamp assembly.
I. Crystal load bar.
J. Platform.

K. Specimen location.

Figure 1. Loading system.
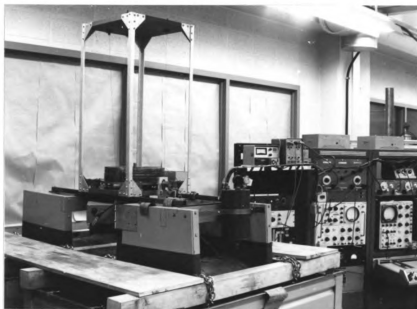
Figure 2. Loading system supported on chains.
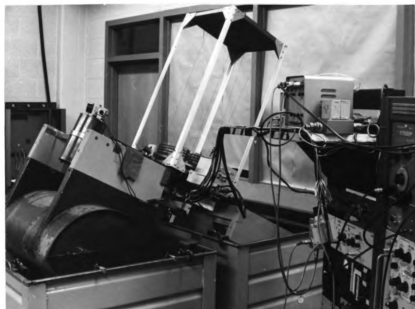
Loader tilted - maximum load

Loader level - no load

Figure 3.   Loading system - floating.
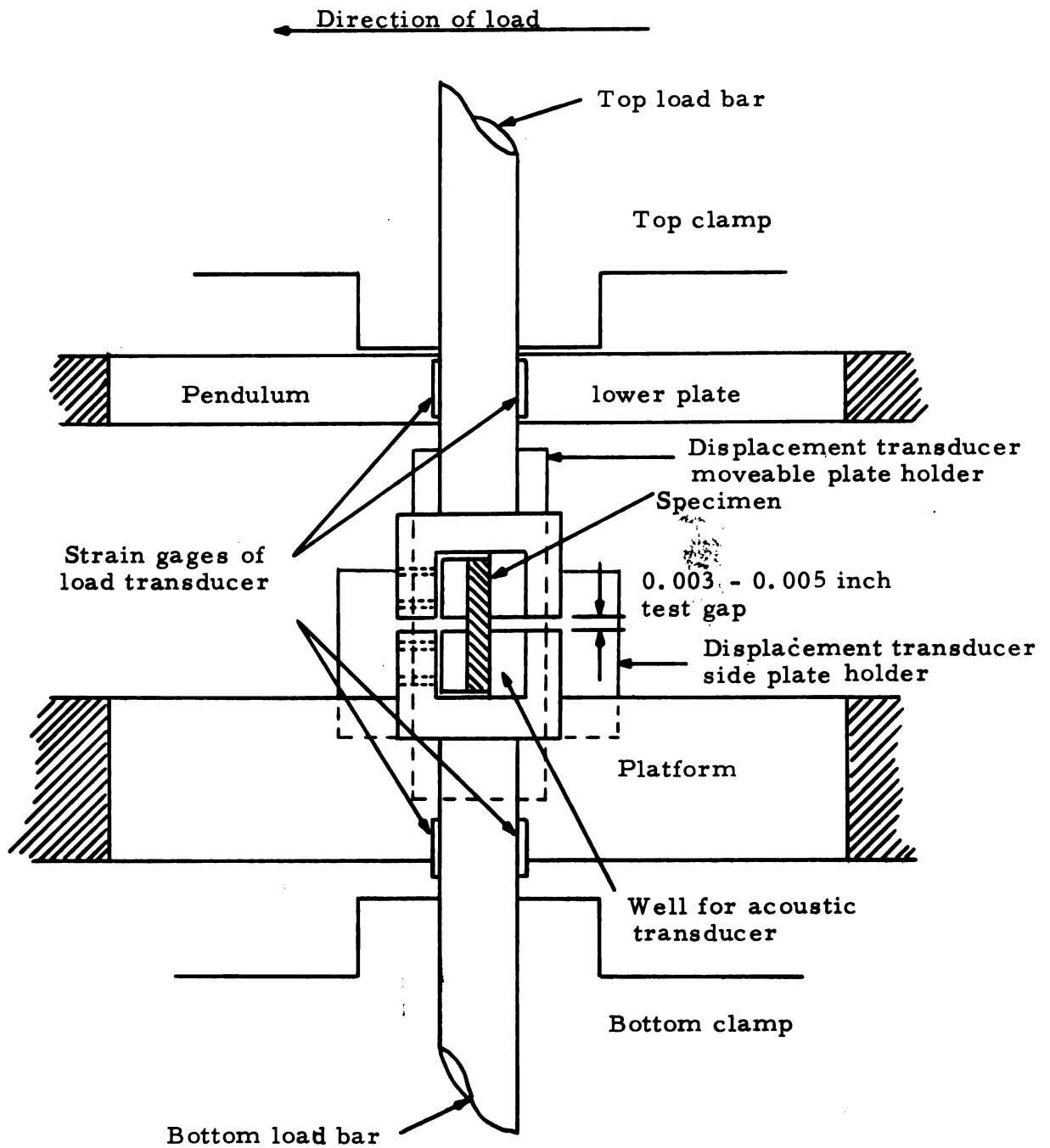
Figure 4. Detail of crystal clamp and load bars.

such that the ratio of average tensile stress to average shear stress increases nearly linearly with the angle of inclination of the loader from a value of zero at 0 degrees to 0.28 at 30 degrees tilt. These extraneous loads caused slip on slip planes oriented at an angle to the load plane of the specimens. The load geometry, described later, severely restricted such undesirable slip in all cases. Furthermore, these additional stresses had no effect on the magnitude of the shear stress on the load plane of easy-glide specimens which were of primary interest.

Acoustic emission, load, displacement, dynamic displacement, and time data were taken with the systems shown in Figures 5 and 6.

During the first few runs, a consistent time reference was provided by recording the output of a time-mark generator on one channel of the tape recorder, and monitoring the recorded time marks with a counter in order to record remarks in the operating log based on test time. In later runs, and for all read-outs, the time marks were also displayed on the oscillograph to allow timewise correlations. These time marks were used to establish time intervals for the electronic pulse height analysis that was run for most of the tests.

The displacement transducer was of the differential capacitance type utilizing a modified Decker Delta unit. Because the Delta unit injected too much noise into the system, it was modified by using batteries to supply filament and B+ voltages to the oscillator. In order to extend the frequency response of the unit and to facilitate its mounting on the loader, the Delta unit follower circuit was duplicated in a custom chassis mounted on the loader. The R. F.

TIME
REFERENCE

ACOUSTIC
EMISSION

DISPLACEMENT

LOAD

```
TIME MARK          ADP            DIFFERENTIAL                    LOAD
GENERATOR         CRYSTAL         CAPACITOR                      BRIDGE

                PREAMPLIFIER      DECKER                         BRIDGE
                                  PROBE                         AMPLIFIER

                  FILTER          CATHODE        PROBE
                                  FOLLOWER      EXCITER

               OSCILLOSCOPE       LOW PASS       POWER
               AMPLIFIER          FILTER         SUPPLY

                                  BUFFER
                                  AMPLIFIER
                                  AND
                                  SIGNAL
                                  CONDITIONER

                              PREAMPLIFIER  PREAMPLIFIER      X-Y
                                                            RECORDER

                                FILTER       FILTER

                              OSCILLOSCOPE             ZERO
                              AMPLIFIER            SUPPRESSION

            SEVEN CHANNEL TAPE RECORDER

   DRIVER        FILTER        FILTER
 AMPLIFIER

                 DRIVER        DRIVER      GALVANOMETER      DRIVER
               AMPLIFIER     AMPLIFIER       MATCH         AMPLIFIER

            MULTI-CHANNEL LIGHT BEAM OSCILLOGRAPH
```

Figure 5. Data electronics, block diagram.
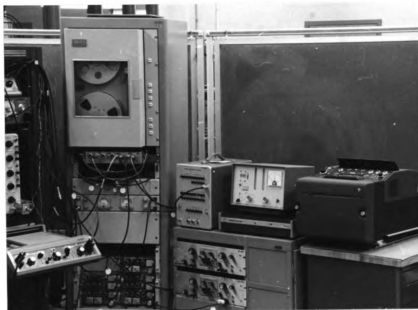
Right side
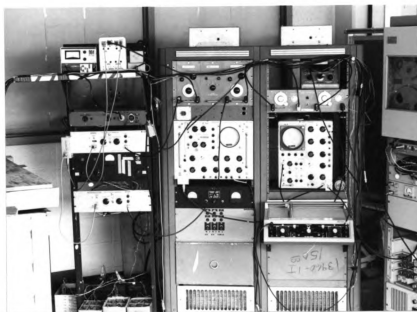
Left side

Figure 6. Data electronics.

excitation was supplied by the oscillator in the original Delta unit. The Decker probe was then connected directly to the cathode follower, thus reducing stray capacitance loading to a minimum with a resulting increase in frequency response. Driven shields were utilized to further reduce the effects of stray capacitance on the frequency response and linearity of the system.

The differential capacitor is shown in Figures 7 and 8. The large central plate operated at ground potential and was attached to the lop load bar so that it would be the moving element. The smaller side plates were mounted on the lower stationary bar.
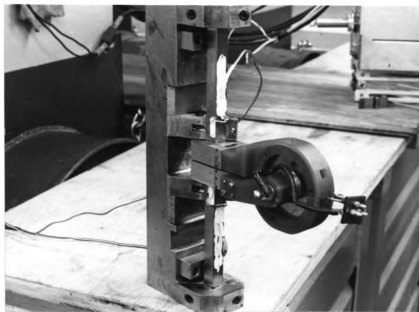
Figure 7. Differential capacitor and load bars in assembly jig.
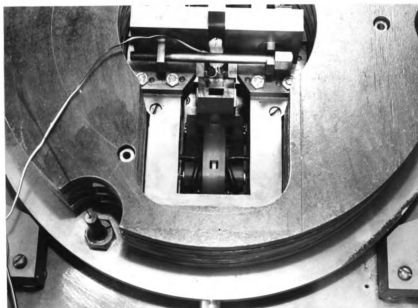
Figure 8. Differential capacitor installed in loader.

The capacitor plates and the spacer used to mount the side plates were made of Invar. This eliminated effects of temperature change on the capacitor spacing and transducer sensitivity. The transducer responds to rotation about a vertical axis through the specimen and lateral displacement due to bending of the load bars (estimated at less than 10×10^{-6} in/lb of load) as well as to relative displacements of the crystal. The pendulum was restrained by lateral wires to prevent rotation. No method was found to eliminate contributions to the displacement due to the bending of the load bars.

The differential capacitor spacing ($d_1 + d_2$, Figure 9) was typically less than 0.030 inches. This spacing gave sensitivities on the order of 2 millivolts per microinch displacement. The edge effects due to the close spacing, slight misalignments, and unavoidable amounts of stray capacitance made the output of the transducer non-linear with displacement. Proper selection of initial settings provided a sufficiently linear output for the range required.

Direction of motion of top load bar

Adjustment screws

Center plate (Invar)

Invar Spacer

d_2

d_1

Epoxy laminated fiberglass

Side plates (Invar)

Specimen position

Center plate holder attaches to top load bar.
Side plate holders attach to bottom load bar.
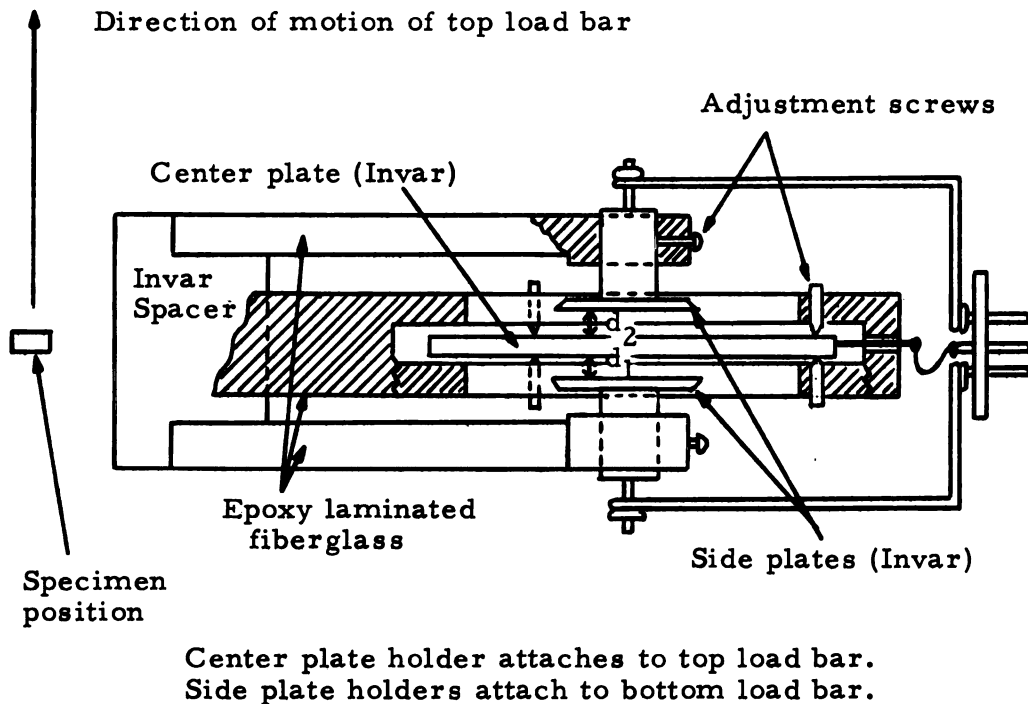
Figure 9. Sketch of differential capacitor.

In-place displacement calibrations were taken after each run in order to measure the transducer sensitivity at every point in the useful range. Figure 10 shows the calibration curve for Run 7. These were made by removing the specimen and translating the pendulum with

a micrometer screw in increments of 0.001 inches over the full range of the transducer. It was possible to locate the initial position of the unloaded crystal on this curve, making the displacement sensitivity known throughout each test.
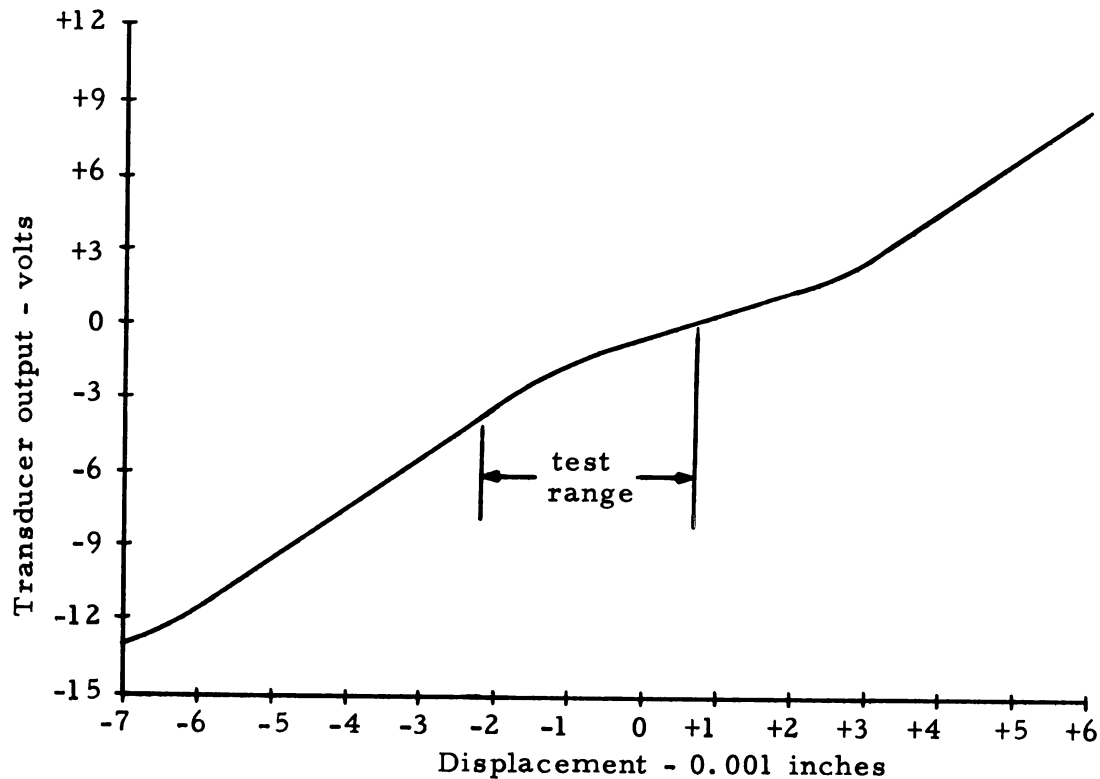
Figure 10. Typical displacement calibration curve.

Initial adjustments of the transducer before installation in the loader were limited to aligning the central plate to be as parallel as possible with the side plates. After the transducer and test specimen were installed in the loader, a capacitance meter was used to adjust the initial capacities to values which would give the necessary sensitivity and linearity. Sensitivities were determined by calibration checks immediately after each test was completed.

The basic transducer output was a differential D. C. voltage. This output was fed to parallel cathode follower amplifiers which provided several outputs for a variety of signal conditioning and data recording purposes. One output was coupled to a preamplifier through a pulse transformer in an attempt to decouple the D. C. level and allow the amplification of dynamic components. This output was called the displacement pulse output.

An alternate output was coupled to a preamplifier with a capacitor. This capacitor was chosen to cause differentiation of the displacement signal which gave a pulse for each step-like change in the displacement. This output, called the step displacement, and the displacement pulse output were amplified, filtered as necessary, and recorded on separate tape recorder channels.

A third coupling amplifier was used to apply the D. C. displacement signal to the X-axis of an X-Y recorder to obtain a load-displacement curve. During later tests this same signal was applied simultaneously to a channel of the oscillograph in order to obtain a load-time record.

When the oscillograph was obtained, the step displacement signal was recorded simultaneously on magnetic tape and the oscillograph. The acoustic emission and displacement pulse signals were recorded on the oscillograph through the tape recorder.

Signal substitution was used to determine the frequency response of the dynamic displacement and acoustic emission channels. The calibration electronics are shown in Figure 11.
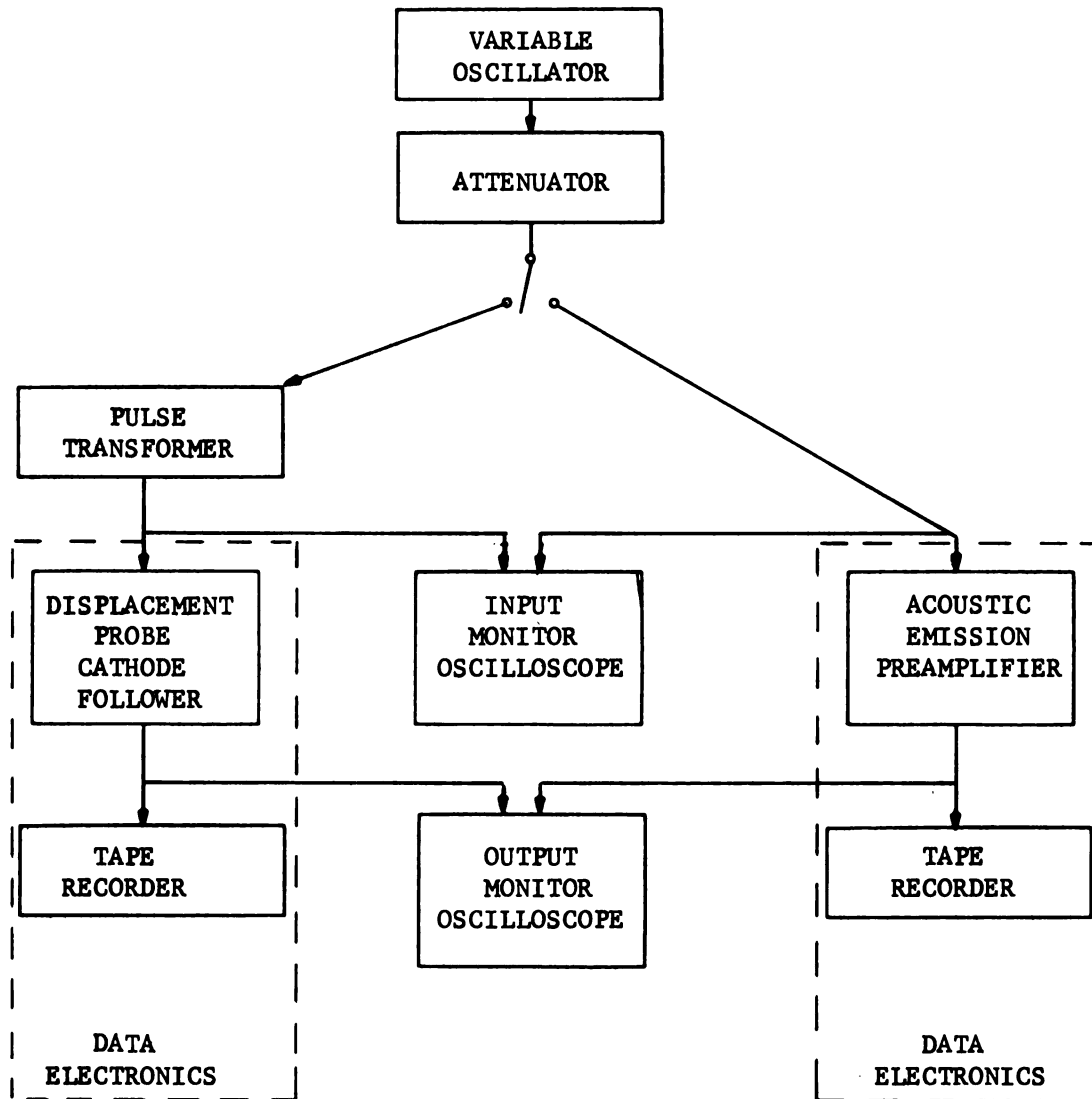
Figure 11. Acoustic emission and displacement pulse frequency response electronics.

The load transducer was a four-arm strain gage bridge applied to the load bars (Figures 12 and 13). Gages 1 and 3 gave positive outputs for tensile strain, while gages 2 and 4 gave positive outputs for compressive strain. The configuration only responds to flexural strains produced by shear loading at the test section. Bridge power, bridge balancing, amplification, scale adjustment, and electrical calibration were provided by the bridge amplifier. The bridge amplifier output was then applied to a galvanometer amplifier for recording on the oscillograph and to the Y-axis of the X-Y recorder to complete the load-displacement curve.

A load calibration was performed using a split specimen and weights (Figure 14). The load bars were positioned and clamped in the loader as they would be during an actual test. The effect of a calibration resistor in the bridge amplifier was noted during the direct calibration, and this standard indication was used to interpret the load transducer output in later tests.

The acoustic transducer, shown in Figure 15, was the same ADP crystal stack used by Liptai[18] and Sedgwick[20]. It was placed directly against the specimen in the well in the specimen clamp heads opposite the displacement transducer. The transducer location is illustrated in Figures 16, 17, and 18. The transducer was held in place with silicone vacuum grease, which also provided acoustic coupling between the transducer and the crystal under test.

Figure 19 shows the acoustic amplifier, which was mounted on the loading frame, as close as possible to the acoustic crystal, to reduce attenuation of the acoustic output by capacitance loading. The
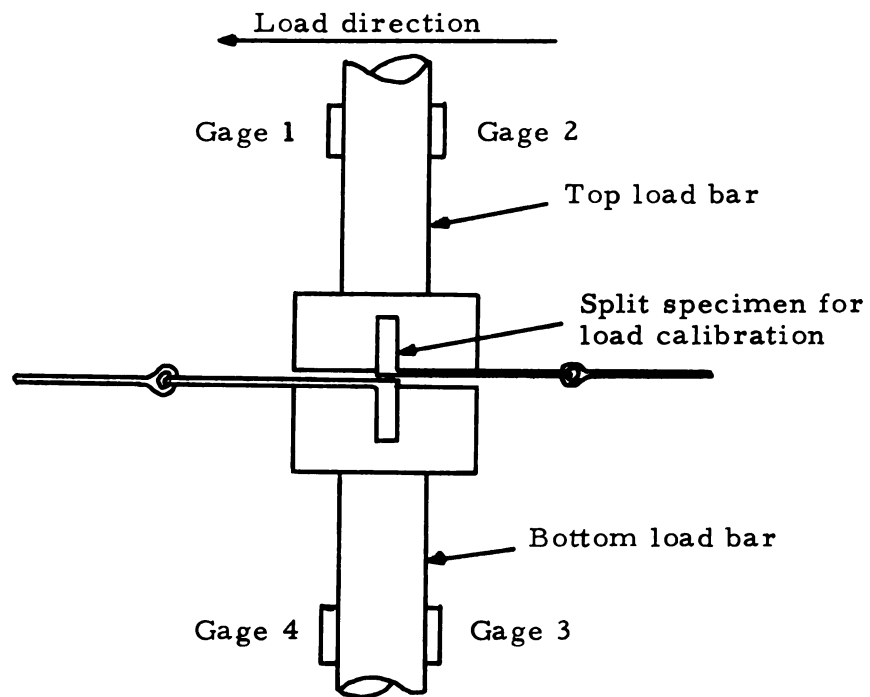
Figure 12. Load transducer gage locations.
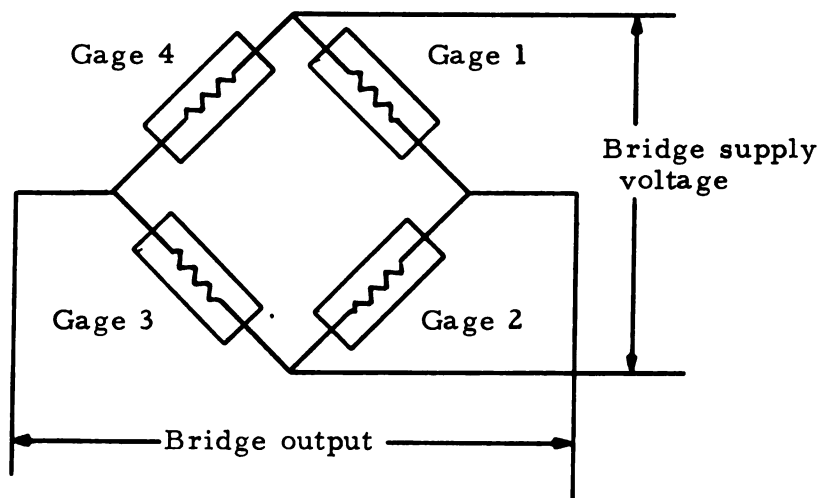
Figure 13. Load transducer bridge connection.
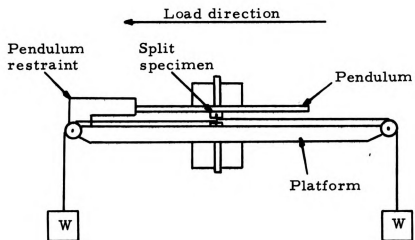
Figure 14. Load calibration system.

Figure 15. Acoustic transducer.
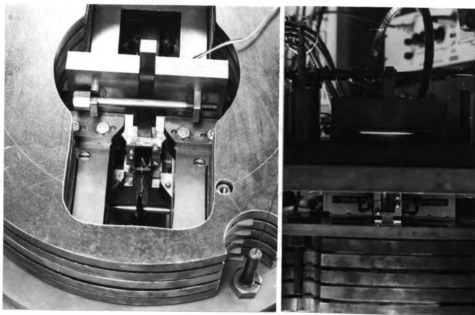
Top view   Side view

Figure 16. Acoustic transducer location.
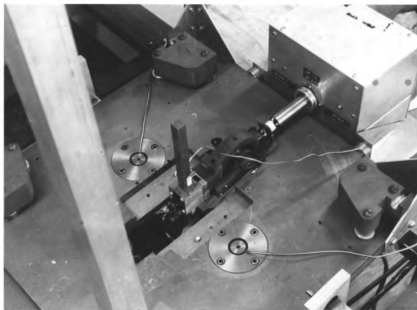
Figure 17. Relative location of acoustic and displacement
transducers - pendulum removed from loader.
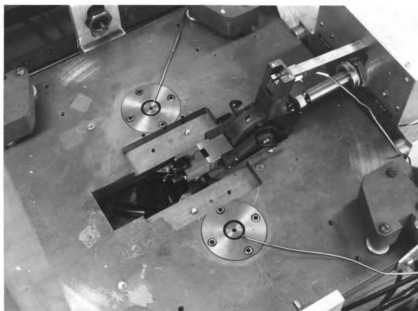
Figure 18. Relative location of acoustic and displacement
transducers with specimen revealed.
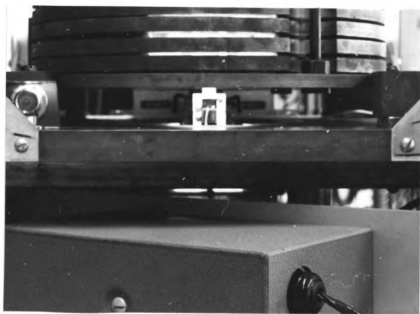
Figure 19. Acoustic emission preamplifier installed.

signal was then filtered and further amplified with the oscilloscope amplifier before being recorded on the tape recorder. In the earlier tests the signal recorded on tape was recorded on the oscillograph by simultaneous playback of the tape recording. In later tests, both the tape recording and the oscillograph recording were obtained simultaneously from the same amplifier output.

An assembly jig was used to hold the load bars in alignment while initial adjustments were made on the displacement transducer. This allowed adjustment of the test section gap and facilitated the installation and clamping of the test specimen. After the specimen was installed, the jig maintained alignment while the load bars with the specimen and displacement transducer were installed in the loader. The load transducer was monitored throughout the assembly and installation process in order to determine the size of any preload the specimen might be subjected to before the test began.

A typical run required twelve hours and was timed so the actual loading test occurred after midnight when the laboratory was most quiet.

Test preparations were started by supporting the loader with chains in order to make adjustments in pendulum alignment and to install the specimen. The specimen load bars were positioned in the assembly jig, and the crystal to be tested was clamped in place. Then the displacement capacitor was installed and initial adjustments were made.

Next, the assembly jig with the clamped crystal and transducer was lowered into position in the loader. After the upper clamp

assembly was secured to the pendulum, the upper and lower grips were tightened; and the assembly jig was removed. During this installation procedure, the pendulum was restrained from movement by a pressure-operated piston mounted on the platform. This piston remained in place until the load test was started to prevent accidental loads on the specimen while adjustments were made.

Final spacing and position adjustments were made on the differential capacitor using a capacitance meter to determine the correct values. Then the Decker probe, its cathode follower, and the acoustic preamplifier were mounted on the loader.

At this point the loader was floated and the chains were removed. The data electronics were then checked, and calibration signals were recorded using the complete recording system.

Just prior to the actual run, all gain and frequency settings were rechecked; and all parts of the system were turned on. Then the restraining post was removed to free the pendulum, a load calibration was placed on the X-Y recorder and oscillograph, and the load valve was opened.

In order to keep a test time record, the time mark signal (one pulse per second) was applied directly to the tape recorder. The simultaneous playback signal was then applied to an electronic counter and to the oscillograph. The oscillograph was turned on first, and test time started when the tape recorder was placed in its record mode. Event times were noted in an experiment log or on a supplemental tape recorder.

The seven channel tape recorder was used only for recording data during loading of the lithium fluoride crystals. When full load was reached, the signals being recorded on the oscillograph by using the playback from the tape recorder were switched directly to the oscillograph, so events occurring during unloading could be observed.

When the loader was again level (no load), the specimen was removed from the load bars; and a steel comparison specimen was tested. Finally the steel comparison specimen was removed, and a direct displacement calibration was placed on the oscillograph and the X-Y recorder.

The position of the displacement transducer was continuously monitored while specimens were being changed so that the initial position for both the lithium fluoride crystal and the steel comparison specimen could be located on the displacement calibration chart.

The crystal orientations chosen were those illustrated in Figure 20. Type I was a $\{110\}$ <110> , easy-glide cyrstal. The first bracket refers to the plane on which the direct-shear load was applied. The second bracket specifies the direction of the stress on the loaded plane. Type II, III, and IV crystals had $\{100\}$ <110> , $\{110\}$ <100> , and $\{100\}$ <100> orientations respectively. Of these four orientations, type III and IV crystals were expected to exhibit brittle fracture, since no easy-glide plane had a shear stress component in the easy-glide direction. The type II crystals were subjected to shear stress in the easy-glide direction on four of the six possible easy-glide planes. The amount of glide is limited, due to the geometry of the crystal clamps; and limited slip followed by
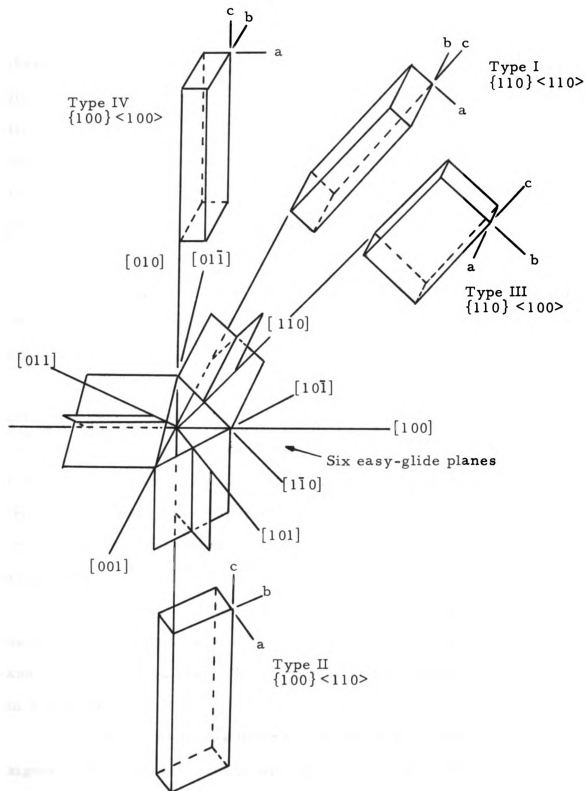
Figure 20. LiF crystal orientations.

crack formation and fracture was expected. The loading placed shear stresses on all six easy-glide planes in the easy-glide direction in the Type I, easy-glide crystal. However, the primary slip system had twice the shear stress of the four other slip planes. Since one plane of the primary slip system was the plane of loading and was not restricted, this crystal was expected to show large plastic deformation before fracture.

Figure 21 illustrates the specimen geometry and the state of applied stress. Figures 22 through 25 show the particular orientations of easy-glide planes relative to the plane of loading for all four orientations.

The magnetic tape recordings of each run were subjected to extensive read-out by three different methods; electronic pulse counting, visual pulse counting from transcripts obtained with a light-writing oscillograph, and RMS signal measurements using a true RMS voltmeter in conjunction with an X-Y recorder. Events of particular interest were photographed using a storage oscilloscope.

Electronic pulse counting yielded the most reliable pulse height distributions as a function of time for both acoustic emission and displacement pulses. The counting system is shown schematically in Figure 26.

The input band-pass filter was necessary to obtain a favorable signal to noise ratio for read-out. Investigation proved the most favorable band-pass settings to be 380-420 hz for the displacement channel and 3.6-3.8 Khz for the acoustic emission channel.
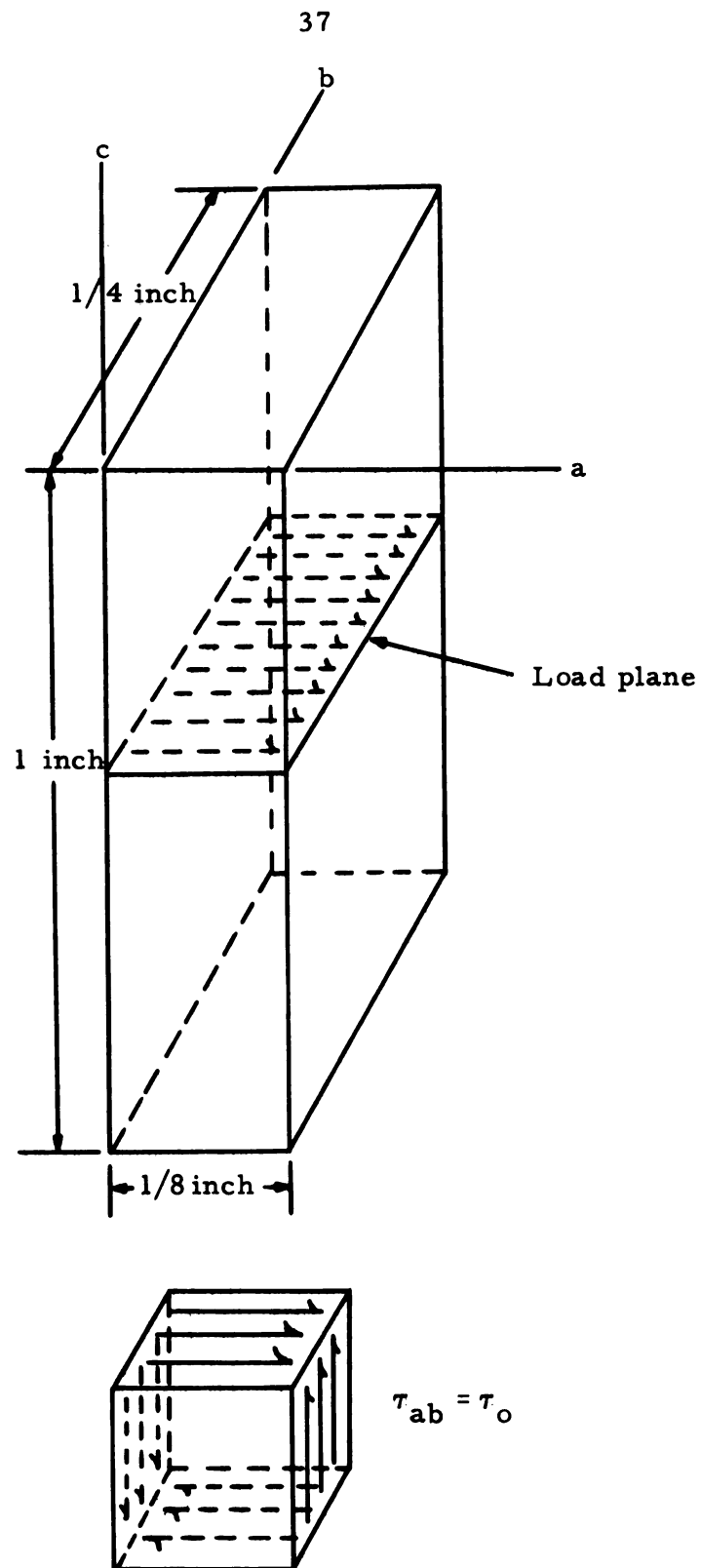
Figure 21. Specimen geometry and state of applied stress.

38

$\sigma_{[011]} = \sqrt{2}\tau_o$
$\tau_{[100]} = \tau_o/2$ } on (011)
$\tau_{[01\bar{1}]} = \sqrt{2}\tau_o/2$

$\sigma_{[110]} = \sqrt{2}\tau_o$
$\tau_{[00\bar{1}]} = \tau_o/2$ } on (110)
$\tau_{[\bar{1}10]} = \sqrt{2}\tau_o/2$

$\sigma = \tau = 0$ on (101) and (10$\bar{1}$).

Figure 23. Easy-glide planes, Type II crystal.

$\sigma_{[\bar{1}0\bar{1}]} = \tau_o/2$
$\tau_{[10\bar{1}]} = \tau_o/2$ } on ($\bar{1}0\bar{1}$)

$\sigma_{[01\bar{1}]} = \tau_o/2$
$\tau_{[0\bar{1}\bar{1}]} = \tau_o/2$ } on (01$\bar{1}$)

$\sigma = 0$ on (110), $\sigma = 0$ on (1$\bar{1}$0).
$\tau_{[1\bar{1}0]} = \tau_o$ $\tau_{[110]} = \tau_o$
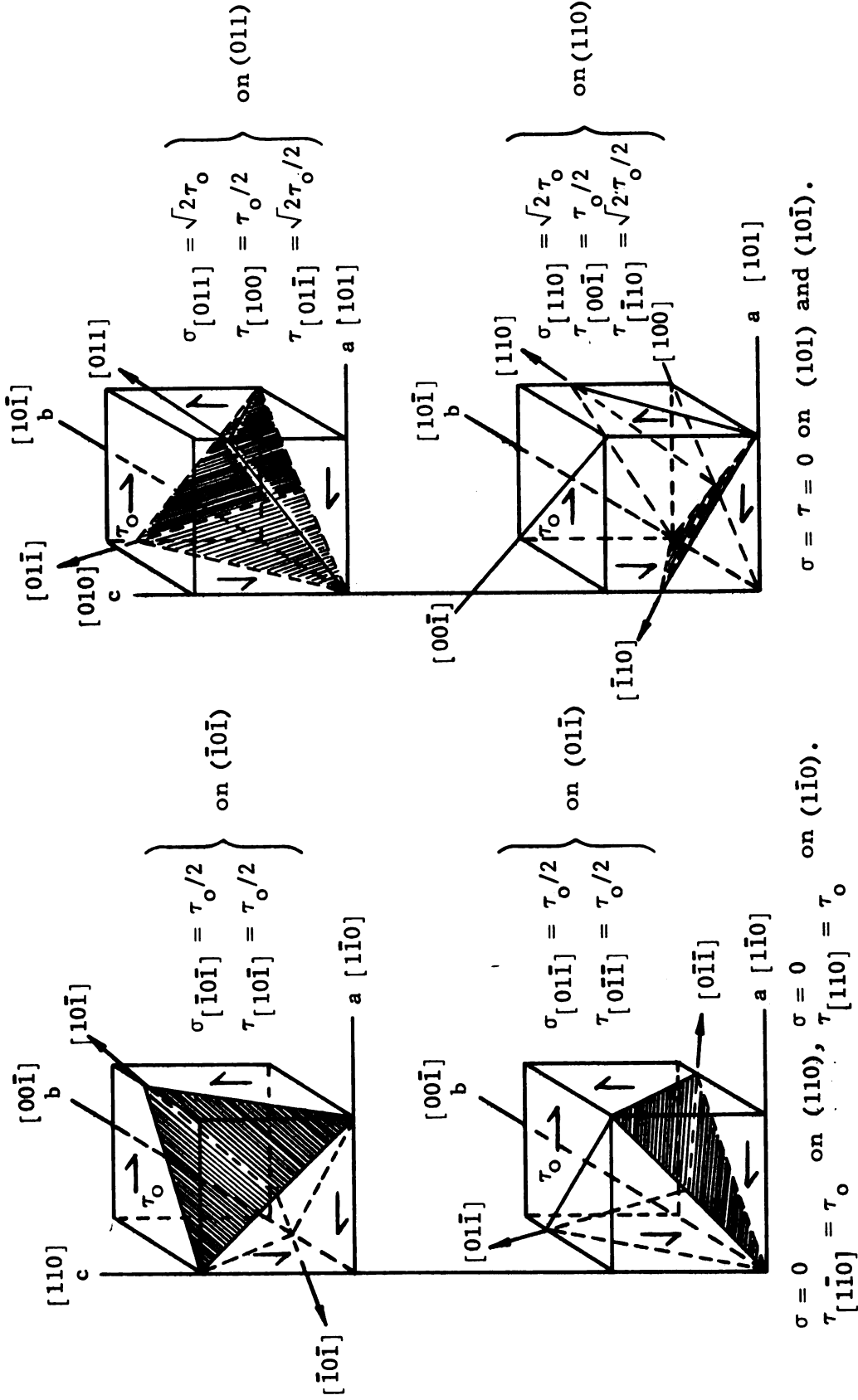
Figure 22. Easy-glide planes, Type I crystal.

Figure 25. Easy-glide planes, Type IV crystal.
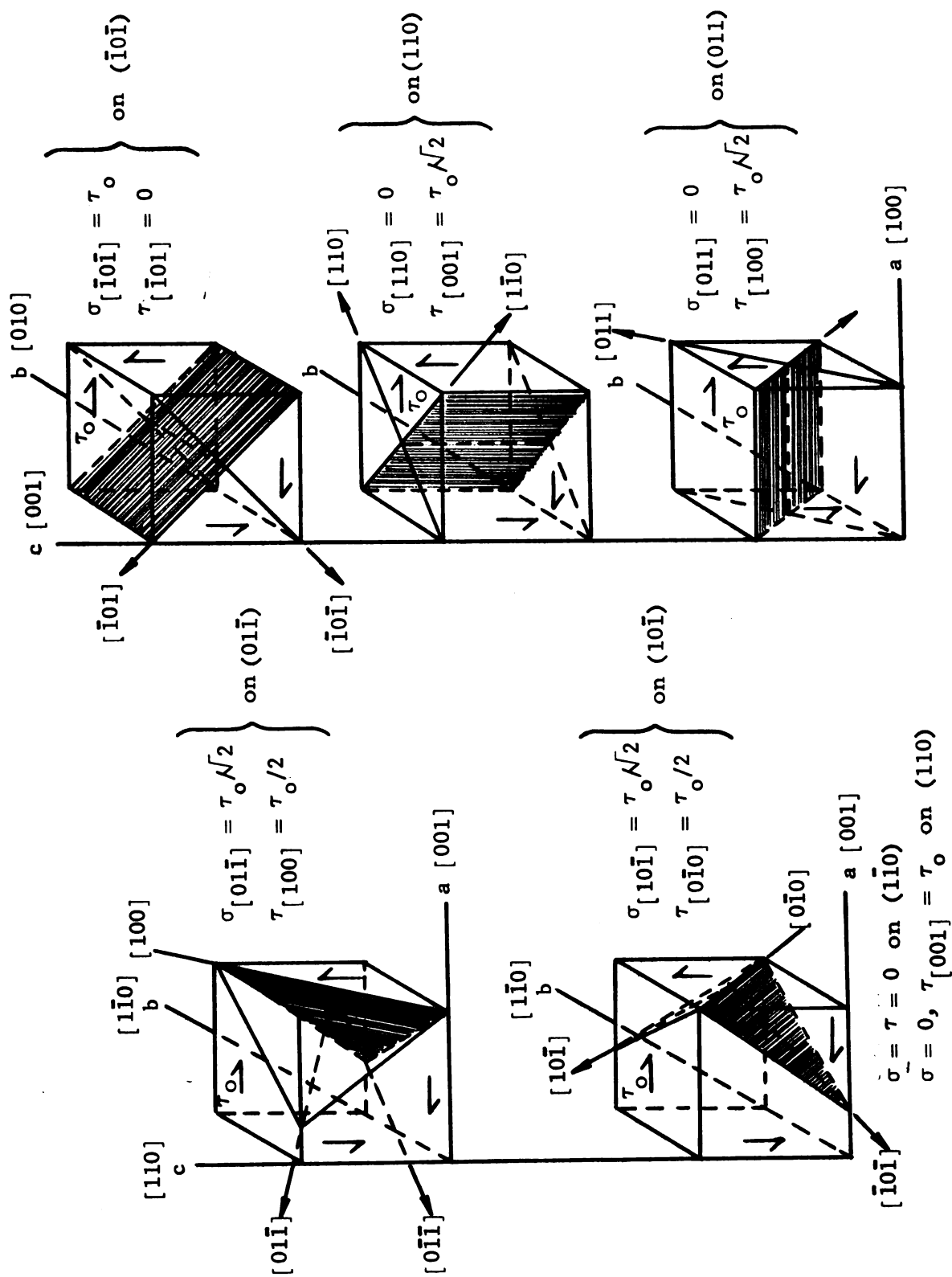
Figure 24. Easy-glide planes, Type III crystal.

```
┌─────────────────┐                    ┌─────────────────┐
│  PULSE INPUT    │                    │ TIME MARK INPUT │
│     FROM        │                    │     FROM        │
│  TAPE RECORDER  │                    │  TAPE RECORDER  │
└─────────────────┘                    └─────────────────┘
         │                                      │
         ▼                                      │
┌─────────────────┐                             │
│   BAND-PASS     │                             │
│    FILTER       │                             │
└─────────────────┘                             │
         │                                      │
         │                                      │
         ▼                                      ▼
┌─────────────────┐                    ┌─────────────────┐
│  OSCILLOSCOPE   │                    │  OSCILLOSCOPE   │
└─────────────────┘                    └─────────────────┘
         │      ◄───┐              ┌───►      │
         │          └── GATE OUTPUT ──┘       │
         ▼                                      ▼
┌─────────────────┐                    ┌─────────────────┐
│   ELECTRONIC    │                    │   ELECTRONIC    │
│    COUNTER      │                    │    COUNTER      │
│    (PULSE)      │                    │    (TIME)       │
└─────────────────┘                    └─────────────────┘
```

Figure 26. Pulse counting and time interval system.

The trigger level adjustment, in conjunction with a square wave calibration signal, was used to set the oscilloscope to trigger only on pulses larger than a selected value. The positive gate output of the oscillosocope, which provided a pulse each time the scope sweep was triggered, was applied to the counter. The dead time of the system, which consisted of the sweep time plus retrace time, could be varied by changing the sweep speed. Sweep speed was adjusted in each instance to minimize both the number of pulses missed, due to too long a sweep time, and multiple triggering on the same pulse, due to too short a sweep time. The appropriate speed was relatively easy to determine by visual observation of the oscilloscope.

The total number of triggered sweeps was recorded at the end of each 10 second interval. The time intervals were determined by observing a second counter totaling the time reference pulses (1 per second) that were recorded on the tape. Each data channel was scanned in this way at various trigger levels ranging down to just above the steady noise level.

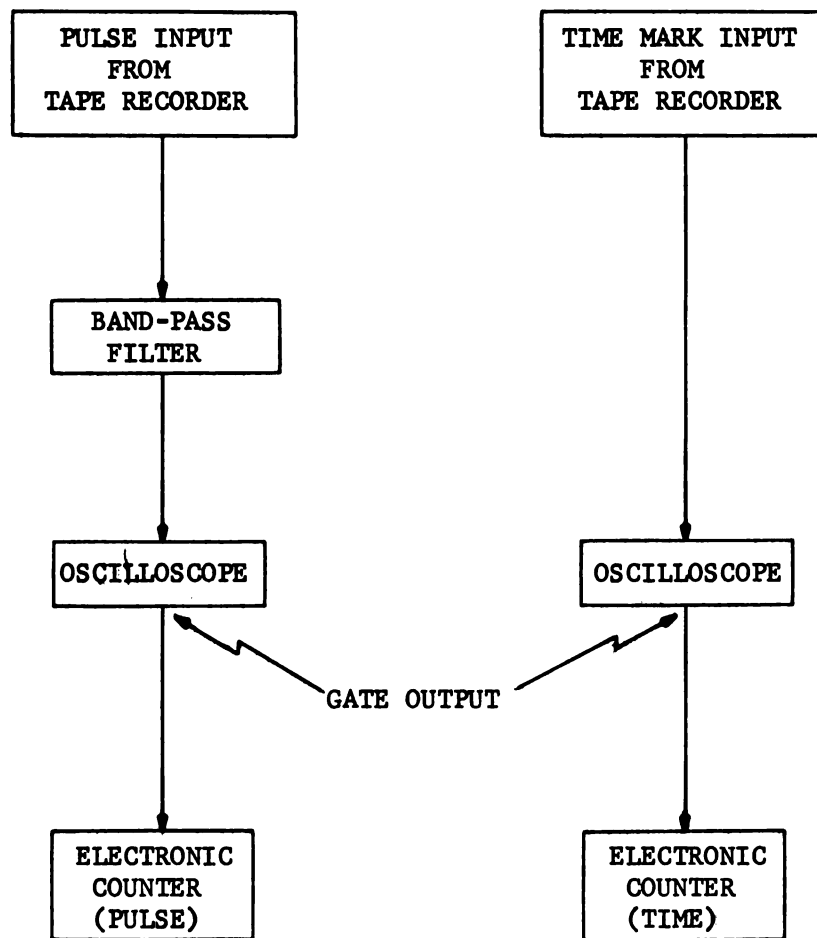Each signal channel was also played back through the system shown in Figure 27. This displayed the RMS signal strength versus time. The recorder pen was lifted every 10 or 20 seconds to indicate the end of each time interval used in the electronic pulse height analysis. The RMS voltmeter attenuator was set to give a small deflection for background noise, and the resulting traces show regions of acoustic emission or displacement pulse activity as spikes above noise. It was felt that this record might indicate regions of activity due to many small pulses that might not be apparent in the

```
┌─────────────┐            ┌─────────────┐
│ INPUT FROM  │            │ TIME MARKER │
│    TAPE     │            │ INPUT  FROM │
│  RECORDER   │            │TAPE RECORDER│
└──────┬──────┘            └──────┬──────┘
       │                          │
       ▼                          ▼
┌─────────────┐            ┌─────────────┐
│ TRUE   RMS  │            │OSCILLOSCOPE │
│ VOLTMETER   │            └──────┬──────┘
└──────┬──────┘                   │
       │                          │
  RMS MONITOR                 GATE OUTPUT
     OUTPUT
       │                          │
       ▼                          ▼
┌─────────────┐            ┌─────────────┐
│X-Y RECORDER │            │  COUNTER    │
│ (X = TIME)  │            │  (TIME)     │
└─────────────┘            └─────────────┘
```
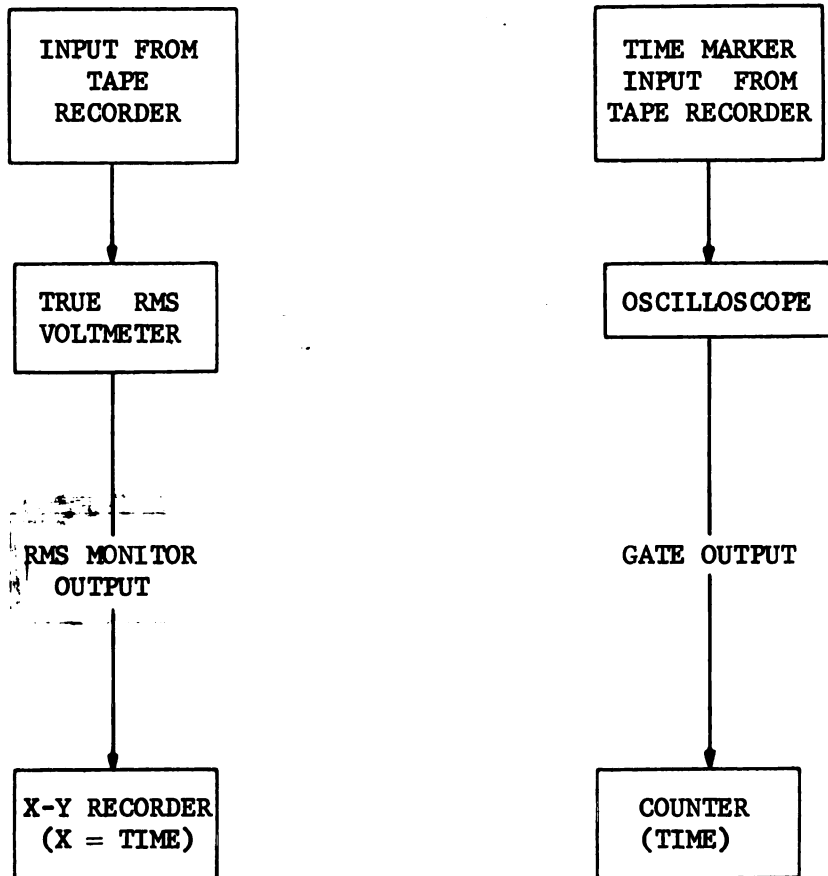
Figure 27. RMS signal read-out.

electronic pulse height analysis. It was possible to confirm coincident events by comparing the acoustic emission and displacement pulse RMS traces.

The three primary data channels (time reference, acoustic emission, and displacement pulse) were also read-out with a light-writing oscillograph with frequency response to 3 Khz. Various signal filtering and tape playback speeds were used. These records, in addition to the similar record obtained during the tests, assisted in confirming pulse counts and coincident events.

Demodulators were used to study the structure of both the acoustic emission and displacement signals in more detail. A mechanical impulse excites both the acoustic emission and displacement transducers to damped oscillations at their natural frequencies. In the absence of reflections these vibrations produce voltage signals that appear as damped sine waves. A single impulse will produce a signal that looks like the sketch in Figure 28. If this signal is demodulated with the circuit shown in Figure 29, the resulting signal will be an exponentially decreasing pulse. The rate of decay is governed by the time constant of the smoothing capacitor and the resistance R, usually the load resistance presented by the measuring instrument at the output of the demodulator.

If the demodulator time constant is chosen to give just the envelope of the input signal, a single impulse will produce a single smooth demodulator output pulse (dashed line in Figure 28). If, however, other impulses are applied to the transducer before the signal from the first impulse has disappeared, the resulting signal
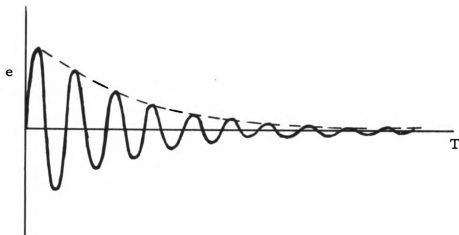
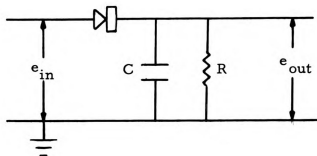Figure 28.   Damped signal resulting from a single impulse.

Figure 29.   Demodulator circuit.

will appear to have additional spikes as shown in Figure 30.

Additional impulses may cause either an increase or a decrease in

the log decrement of the input signal, depending upon whether the

impulse is out of phase or in phase with the natural vibration of the

transducer element. Only those impulses that produce a decrease

in the log decrement would appear on the demodulated output, because

half of the impulses, on the average, will be out of phase with the

vibrating transducer. The number of events determined from the

number of spikes in the demodulated signal will, therefore, only

represent approximately one half of the events occurring.
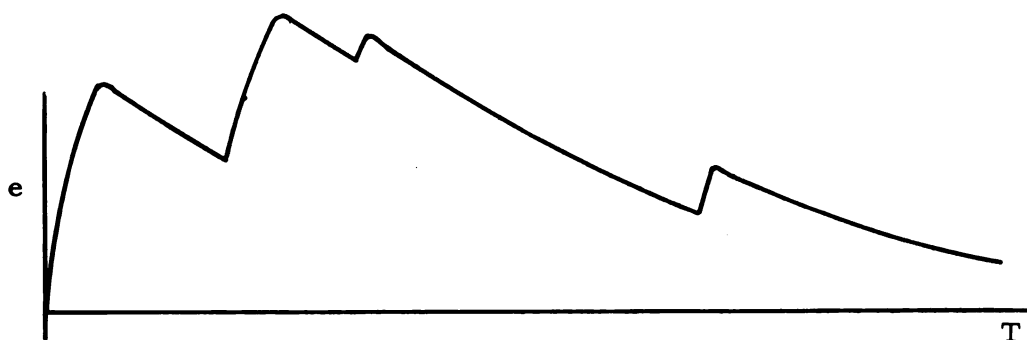
Figure 30. Demodulated signal containing several impulses.

All crystals were investigated with a polarizing microscope

to determine the mode of deformation. Only Type I and Type IV

crystals were oriented to make dislocations visible in polarized

light, since the Burgers vector must be in the direction of the

analyzer or polarizer transmission axis. The other two crystal

orientations would be expected to show the presence of stress

concentrations due to dislocations only if many are introduced into the specimen.

PRESENTATION OF DATA

Tests were run on fourteen crystals: nine Type I (easy-glide), two Type II, two Type III, and one Type IV. Of the tests of the Type I crystals: two were exploratory, one crystal was broken while being installed in the loader, and two were found to be misoriented. The remaining four Type I crystals all behaved consistently. Run 7 was the best documented test and data from it will be presented in detail.

The other types were tested primarily as control crystals, since little or no emission was expected from any of them. Table 1 lists the tests and a brief summary of the results of each. The test numbers were assigned in the order in which the tests were run.

Figure 31 shows a curve of shear load versus shear displacement for a representative of each type of crystal tested; the curves show both loading and unloading behavior. The flat portion at the top of three of the plots represents continued deformation at the maximum load for a few minutes before unloading began. All crystals were tested in as-received condition several months after they arrived from Harshaw Chemical Company. The only specimens that exhibited large instantaneous displacements, similar to Portevin-LeChatelier discontinuous slip, were the Type I crystals.

Figure 32 presents the acoustic emission behavior observed during Run 7, a typical test of a Type I, easy-glide crystal. This plot shows the number of countable acoustic emission pulses that occurred in each ten second time interval and confirmed coincidences

Table 1. List of runs and summary of results

| Test number	Summary of results
	Type I, {110}<110>, easy-glide crystal
1	Exploratory - no data
2	Exploratory - deformation by uniform single slip
3	Acoustic emission, displacement pulses, and coincidences
4	Acoustic emission, displacement pulses, and coincidences
7	Acoustic emission, displacement pulses, and coincidences
8	Crystal broken while installing in loader
9	Acoustic emission, displacement pulses, and coincidences
10	No emission or displacement pulses above noise - misoriented
13	Limited emission - no displacement pulses above noise - misoriented
	Type II, {100}<110> crystal
5	No emission above noise - displacement pulse circuit inoperative
12	No emission or displacement pulses above noise
	Type III, {110}<100> crystal
6	No emission or displacement pulses above noise
14	Some low level emission - no displacement pulses above noise
	Type IV, {100}<100> cyrstal
11	Fracture on cleavage plane
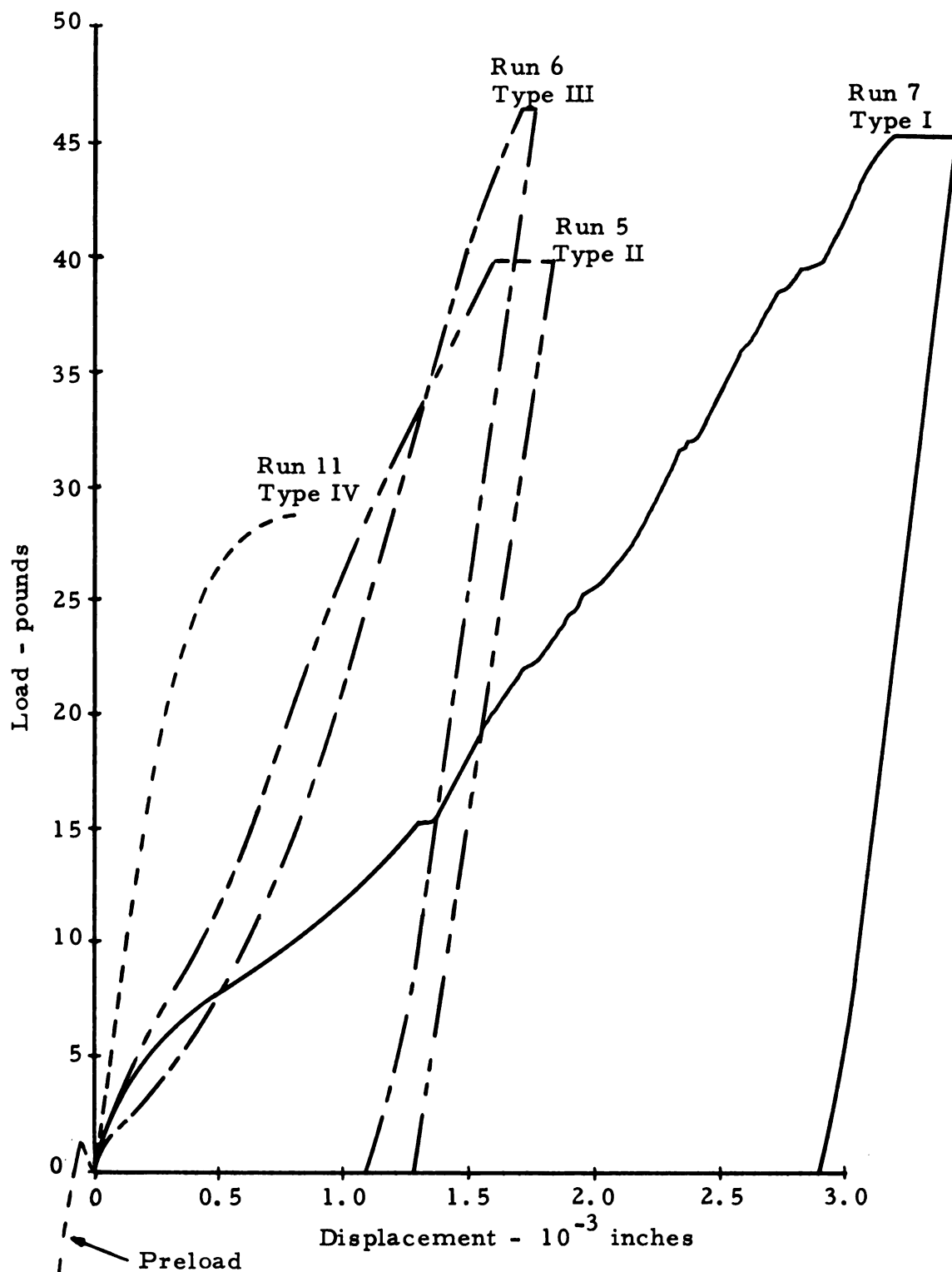
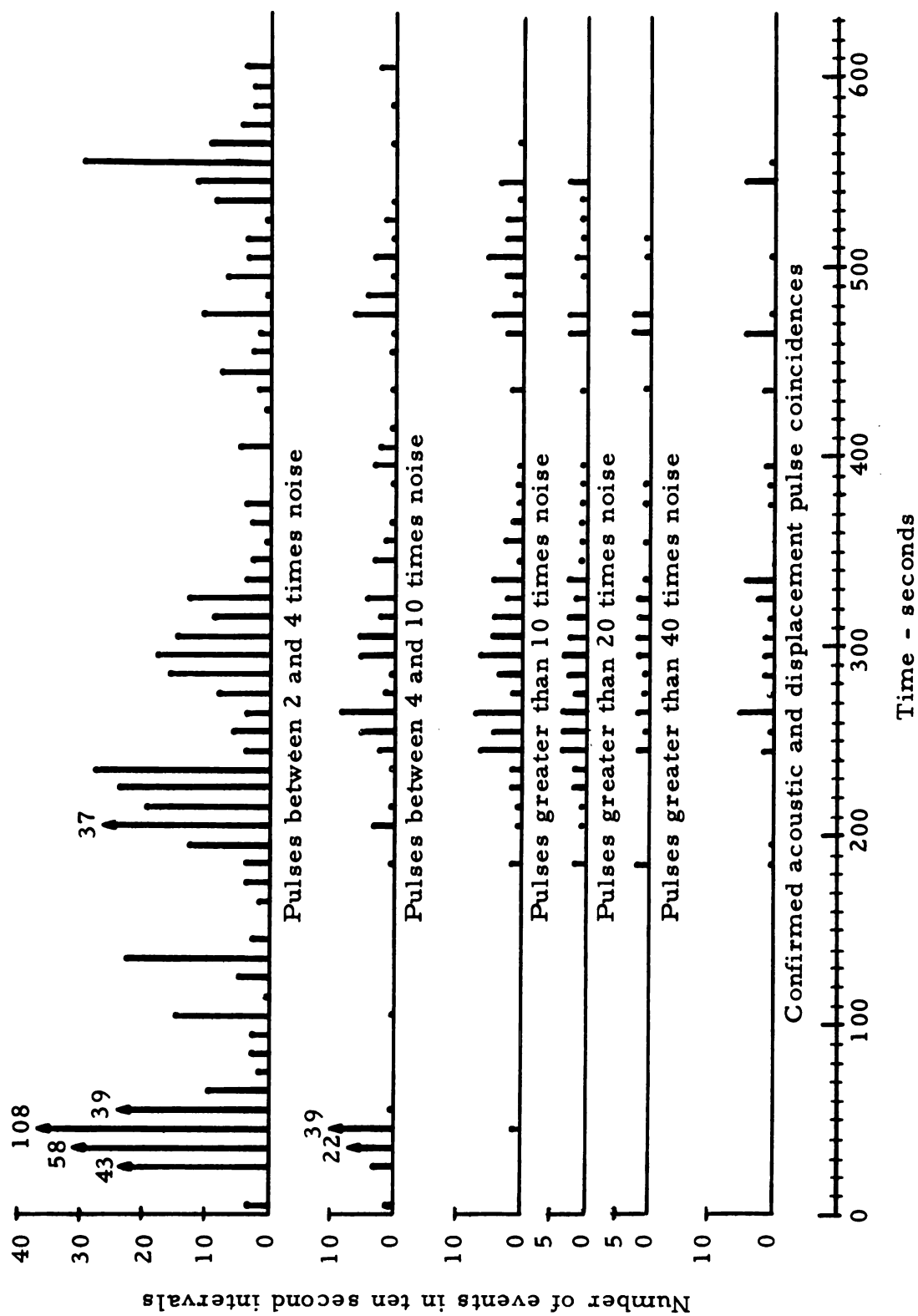Figure 31. Representative load-displacement curves.

Figure 32. Acoustic emission pulse distribution – Type I, Run 7.

between emission and displacement pulses. Low Level emission appeared early in the test, at or before the yield stress. High level emission appeared only at higher stresses, with a lower occurrence rate. The tests that produced coincident acoustic emission and displacement pulses were tests 3, 4, 7, and 9 - all Type I, easy-glide crystals. Again, Run 7 was typical.

The confirmed acoustic emission and displacement pulse coincidences shown at the bottom of the acoustic emission plot were those that appeared to occur simultaneously on the record obtained with the light-writing oscillograph. The recording speed used was 1 inch per second, which made resolution of coincident pulses possible to within 0.05 seconds. Further verification of coincident events was obtained using a dual trace oscilloscope. Many pictures taken of the oscilloscope traces show that the coincidences are simultaneous to within a few milliseconds.

Figure 33 presents the displacement pulse behavior observed for Run 7. The noise level observed during the pulse height analysis of this run was equivalent to the amplitude of pulses that would correspond to displacements of 2×10^{-7} inches at the transducer sensitivity and amplifier gain used. This displacement is equivalent to the displacement that would be produced by 9 unit dislocations when they pass out of the crystal. Larger displacement pulses observed during Run 7 involve groups of from 200 to 3200 unit dislocations. A complete tabulation of acoustic emission channel gains and displacement pulse sensitivities for all 14 tests is included in Appendix B.
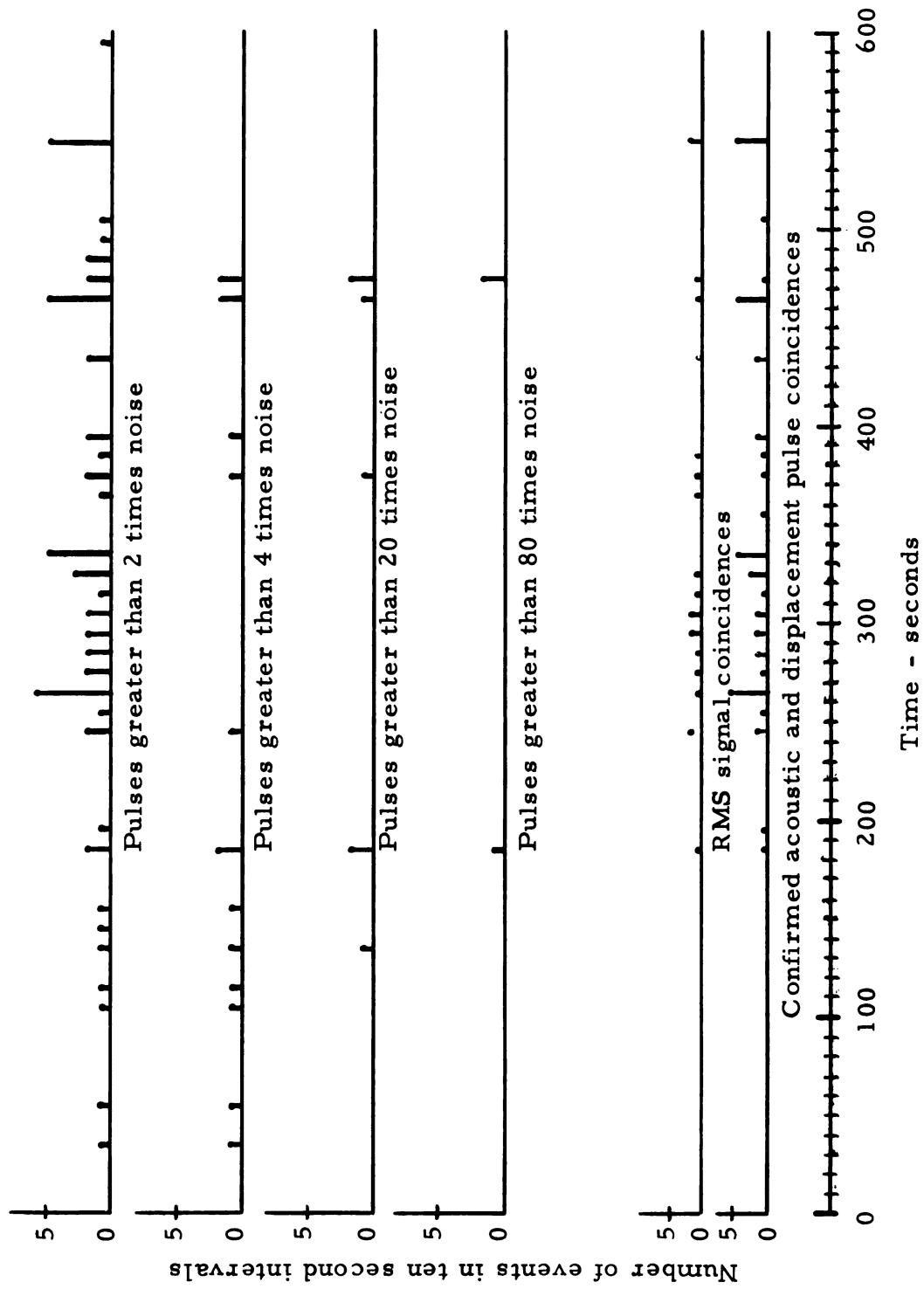
Figure 33. Displacement pulse distribution – Type I, Run 7.

This plot (Figure 33) shows the number of countable displacement pulses that occurred in each ten second interval as well as the confirmed pulse coincidences in corresponding intervals. In addition, coincidences confirmed with RMS signal traces are shown.

The largest displacement pulses almost always had large acoustic emission pulses in coincidence with them. The pulse distribution plots (Figures 32 and 33) indicated that the small displacement pulses make a large contribution to the confirmed coincidences while the low level acoustic emission pulses make very little contribution. In fact, many large acoustic emission pulses were observed with no indication of displacement activity. This is illustrated by Figure 34 which presents a series of oscilloscope pictures showing acoustic emission signals above and displacement pulse signals below. These pictures were obtained using a dual trace amplifier in a storage oscilloscope. The signals were conditioned by very restrictive bandpass filters and a demodulator that severely attenuated the recorded signals. Only the largest signals appear in each channel. The numbers at the lower edge of the pictures identify many of the coincident events plotted with the pulse distributions.

The three displacement pulses appearing in the third through fifth centimeter of the trace are not coincident with any acoustic emission pulse. There appeared to be a delay on the order of three seconds between three of the four acoustic emission pulses that appear above them and these three displacement pulses. These are the only large displacement pulses that were not coincident with emission pulses in Run 7. This apparent anomaly is explained in a later section.
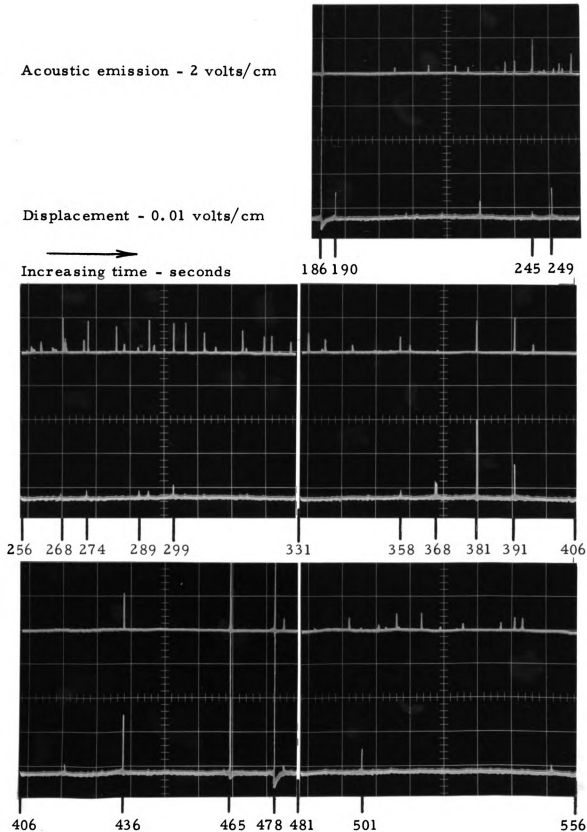
Figure 34. Oscilloscope traces of demodulated acoustic emission and displacement pulses - Type I, Run 7.

The Type I, easy-glide crystals were the only specimens to deform by large, instantaneous slip. This behavior is indicated by the horizontal segments and discontinuities in slope at several points on the load-displacement curve presented in Figure 35. Because load was proportional to time, the two vertical scales correspond identically. The early start of low level acoustic emission indicated that plastic deformation started immediately upon loading of Type I crystals. Furthermore, no well defined yield point was observed for any of the four typical Type I tests. Minor differences in initial behavior of the typical Type I tests may be attributed to differences in clamping which, in turn, will cause differing amounts of stress concentration at the boundary between the clamped region and the unrestricted test section and may introduce different numbers of fresh dislocations into the crystals due to indentation. The instantaneous slip events and pulse coincidences shown on the load-displacement curve for Run 7 agree quite well with each other.

Figure 36 shows a segment of the light-writing oscillograph record that was obtained during Run 7. The event shown occurred at T = 186 seconds. One second timing marks are at the top. The second trace down is a static reference trace. Then, in order, the displacement pulse, step displacement signal (explained on page 25), and acoustic emission signal appear. The D. C. displacement signal that was recorded on the X-Y plotter is shown at the bottom along with another static reference trace. The instantaneous displacement shown on the D. C. displacement signal at the bottom coincides with the displacement pulse appearing on the step displacement channel.
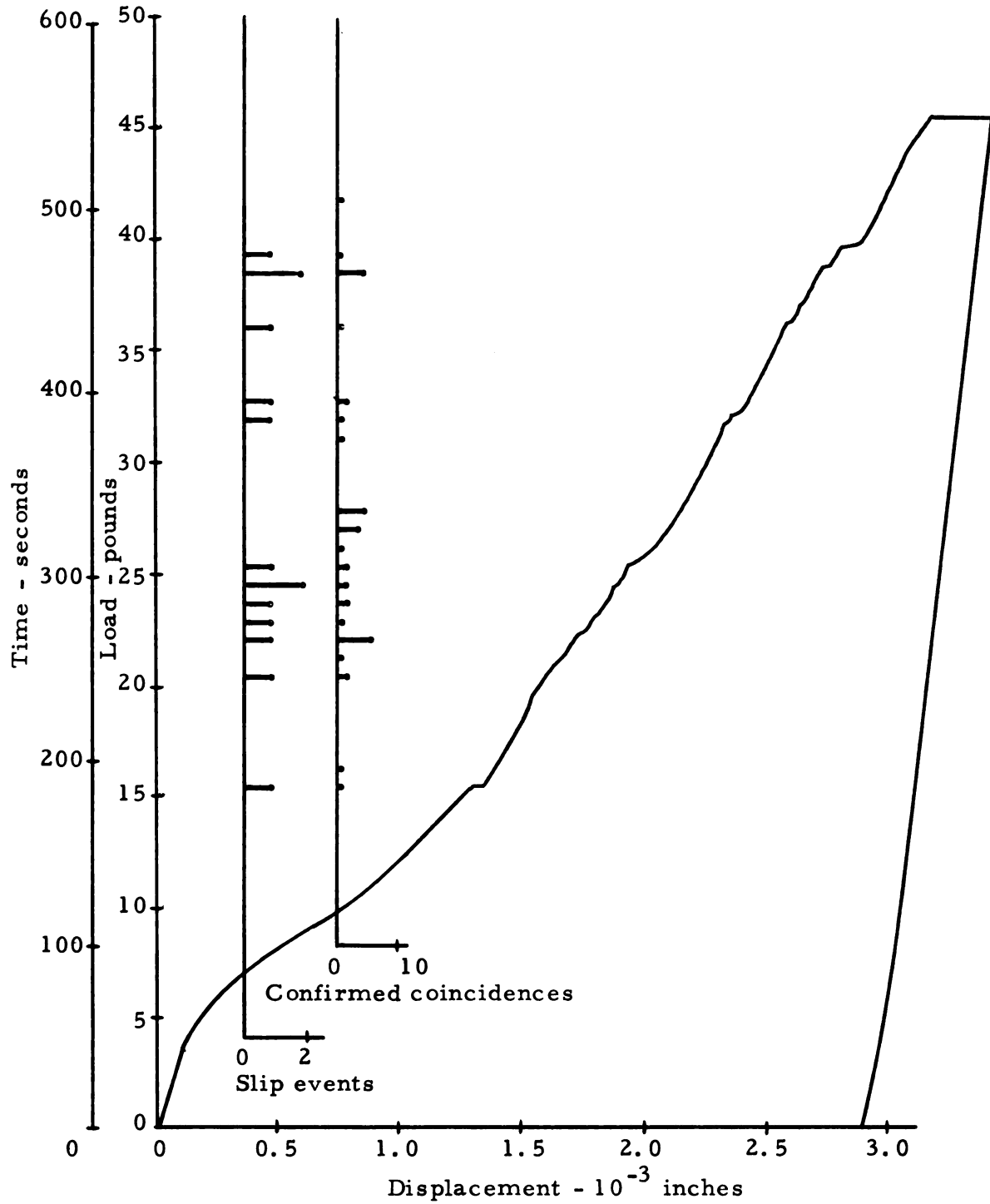
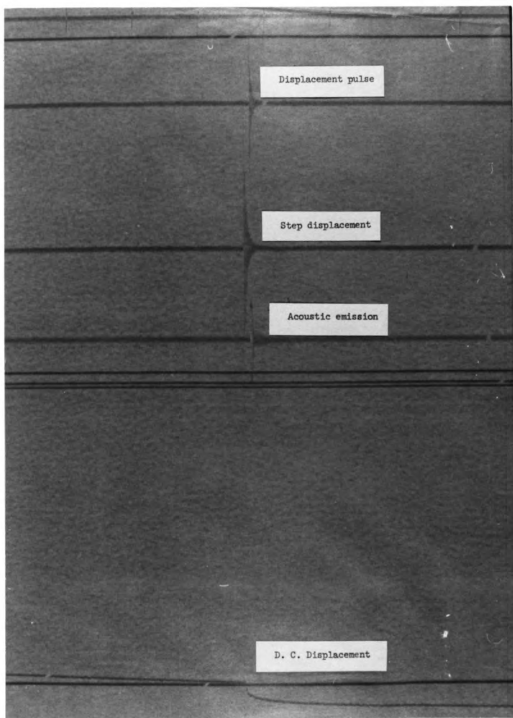Figure 35. Load-displacement and coincidences - Type I, Run 7.

Figure 36. Oscillograph record - event at T = 186 seconds.

The acoustic emission pulse coincides with the displacement pulse on the top trace. The offset between these pairs of signals is due to the fact that the step displacement and D. C. displacement were recorded directly on the oscillograph, while the displacement pulse, time reference, and acoustic emission signals were recorded on the oscillograph by simultaneous playback of the signals recorded on the tape recorder. The delay, therefore, represents the time required for a location on the tape to travel from the record head to the reproduce head. Run 7 was the only Type I run for which the D. C. displacement was successfully recorded on the oscillograph with sufficient sensitivity to be able to measure the magnitude of the instantaneous slip displacements. It was this record that provides proof of the coincidence of the emission and displacement pulses with the instantaneous slip behavior observed in the Type I crystals. The instantaneous displacement shown in Figure 36 had a magnitude of 50×10^{-6} inches.

Further detail of the same event is shown in Figure 37. Picture A shows the filtered emission and pulse displacement signal traces in a time interval starting at T = 183 seconds and ending at T = 191 seconds. The large coincident signals at T = 186 seconds are also shown in pictures B and C. A second coincident event is barely discernible at T = 190 seconds. The acoustic signal there is quite small. Picture B shows the filtered signals at a sweep speed of 5 milliseconds per cm. The upper trace is the acoustic emission signal. Picture C shows the same event after the signals were demodulated, as described earlier on pages 43 through 45 . These pictures indicate that the coincidence

Emission – 2 volts/cm

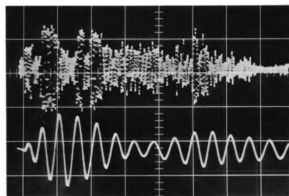Displacement – 0.5 volts/cm
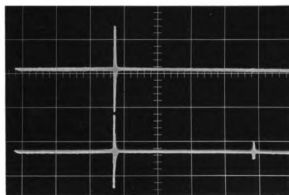
186

Picture A.   Sweep speed 1 second/cm
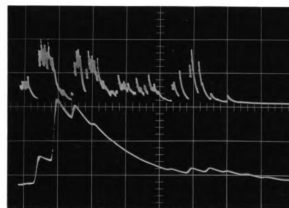

Emission – 2 volts/cm

Displacement – 0.5 volts/cm

Picture B.   Sweep speed 5 milliseconds/cm

Emission – 1 volt/cm

Displacement – 0.1 volts/cm

Picture C.   Sweep speed 5 milliseconds/cm

Figure 37.   Oscilloscope traces – event at T = 186 seconds – Type I, Run 7.

between the acoustic emission and displacement pulse is exact to within 2 to 4 milliseconds.

The demodulated signals show the complex, discontinuous nature of both the acoustic emission and displacement signals. In this picture 75 spikes are seen in the acoustic emission signal and 11 are seen in the displacement pulse. The duration of acoustic emission activity is 32.2 milliseconds. Table 2 tabulates similar data obtained from oscilloscope photographs and the oscillograph record for this and five other coincident events observed during Run 7. The photographs appear in Figure 46 and in Appendix F (Figure 55 through 58).

When the crystal was observed with a polarizing microscope after the test, it was found to have cracks that appeared to start at the surface in the test section, propagate along the (110) plane, and then shift to a primary cleavage plane, and propagate into the clamped region. Figure 38 shows the test region of the crystal tested in Run 7. Picture A was taken with ordinary white light and shows slip lines and cracks present in the test section. Picture B was taken with polarized light viewed through a crossed analyzer and reveals that the deformation was primarily by the mechanism of single slip. These pictures give some indication that crack formation and large instantaneous slip may have occurred simultaneously in some instances. All four typical Type I crystals exhibited some large acoustic emission with no simultaneous displacement, in addition to coincident emission-displacement events. In each case where isolated emission was observed, cracks were found when microscope observations were made.

Table 2.   Pulse data from oscillograph and oscilloscope traces
for coincident events, Type I, easy-glide, Run 7.

Time of event	Number of spikes on demodulated acoustic pulse	Duration of acoustic activity	Magnitude of instantaneous slip	Average shear stress	Remarks
	N	T	Δ	τ_o	
seconds		$(10^{-3}$ sec)	$(10^{-6}$ inches)	psi	
186	75	32.2	50	491	Figure 37
292	28	11	6	741	Figure 55
381	34	19.6	15	1010	Figure 56
436	23	6.5	0	1160	Figure 46 *
	35	15	10		**
	58	21.5	10		***
465	36	15	10	1235	Figure 57
467	-	15	11	1235	Figure 57
478	80	30	72	1270	Figure 58

*   Counting first large burst of acoustic emission only.
**   Counting spikes in remainder of pulse only.
***   Total spike count.

A
Left side White light Right side
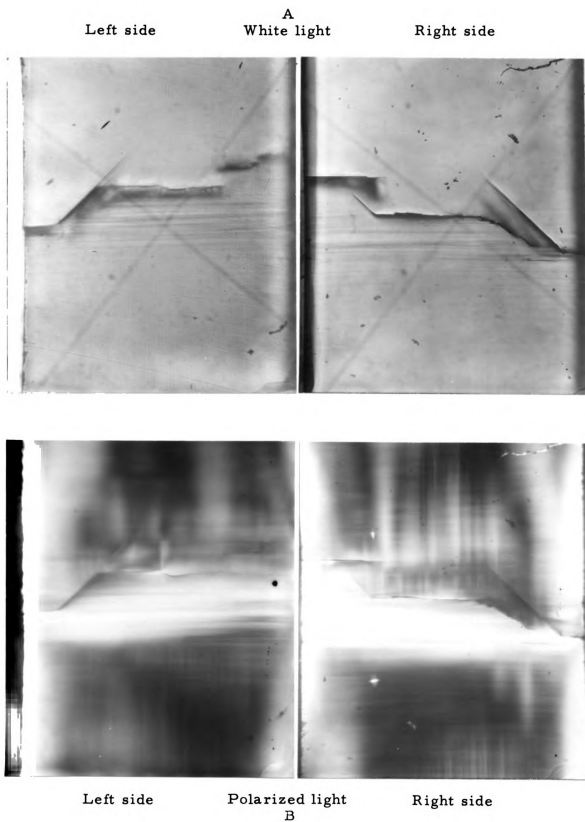

Left side Polarized light Right side
B

Figure 38. Micrograph of tested Type I crystal, Run 7.

Load-displacement curves for Runs 3, 4, and 9 also showing confirmed pulse coincidences and large, instantaneous slip events for Type I specimens are presented in Figures 39, 40, and 41. The corresponding emission and displacement pulse distributions are in Appendix E (Figures 48 through 53). No inconsistencies with Run 7 results were observed in these three additional Type I tests.

The two misoriented Type I crystals produced no countable displacement pulses or detectable RMS displacement activity. Of these two crystals, Run 10 gave some RMS emission activity at higher stresses and Run 13 gave both countable, low-level emission and RMS emission activity. Most of this appeared at and above the fairly well defined yield point (Figure 42).

Type II crystals, Runs 5 and 12, produced no countable pulses in either data channel. Run 5 was not expected to give any displacement pulses, because the data filter was set to eliminate signals below 2 Khz. Limited RMS activity was apparent in both channels around T = 375 from the crystal tested during Run 12. The load-displacement curve for Run 5 is included in Figure 31. Figure 43 represents the data from Run 12.

Type III crystals, Runs 6 and 14, gave different results. Run 6 produced no countable emission or displacement pulses. Run 14 gave some emission pulses and limited RMS activity in both channels. Data for Run 14 is shown in Figures 44 and 45. No pulse coincidences were found, even though Figure 44 shows activity in matching time intervals. The Type II and III crystals showed some evidence of stress concentrations due to plastic deformation when viewed with
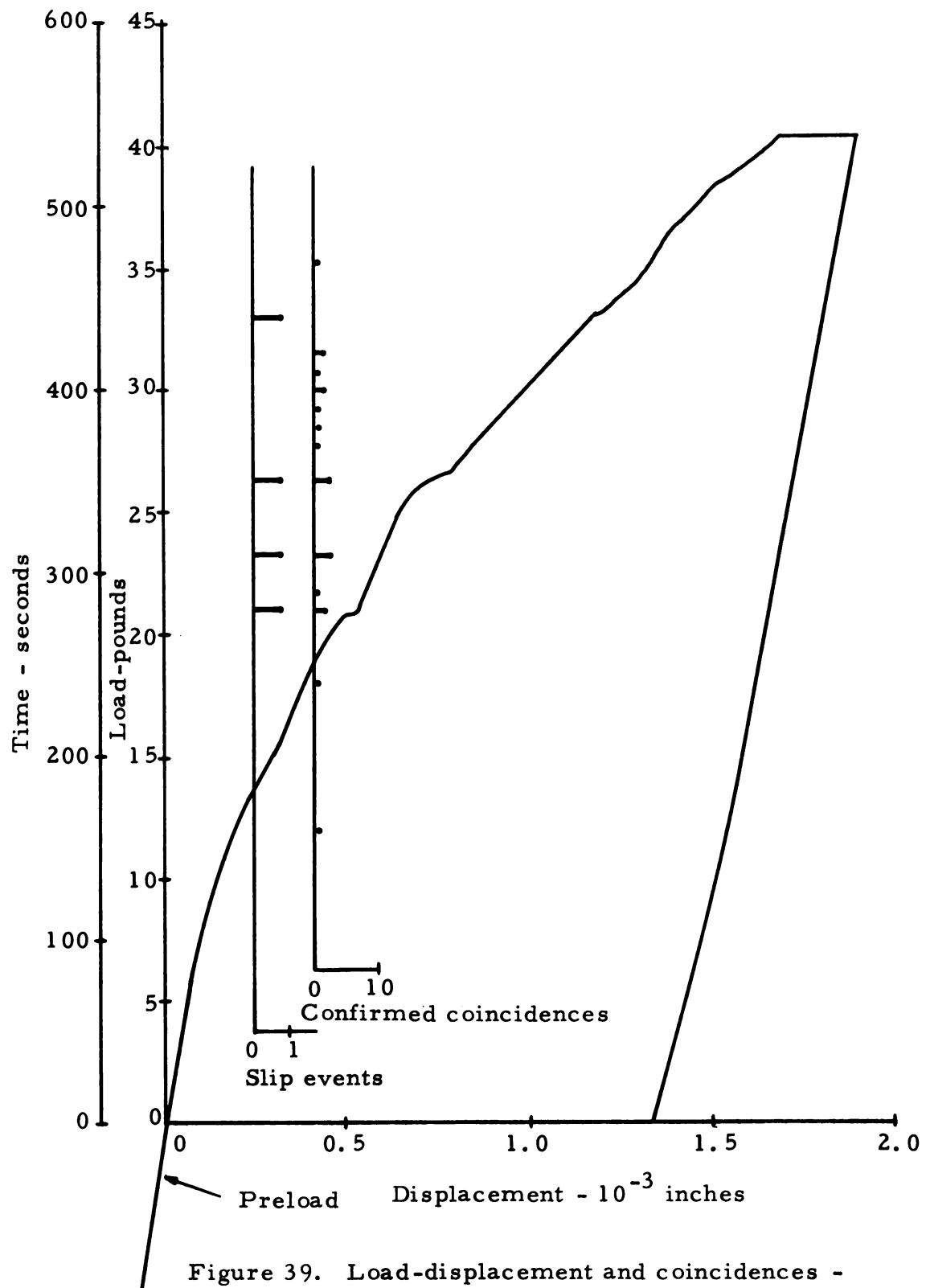
Figure 39. Load-displacement and coincidences - Type I, Run 3.

Figure 40. Load-displacement and coincidences - Type I, Run 4.
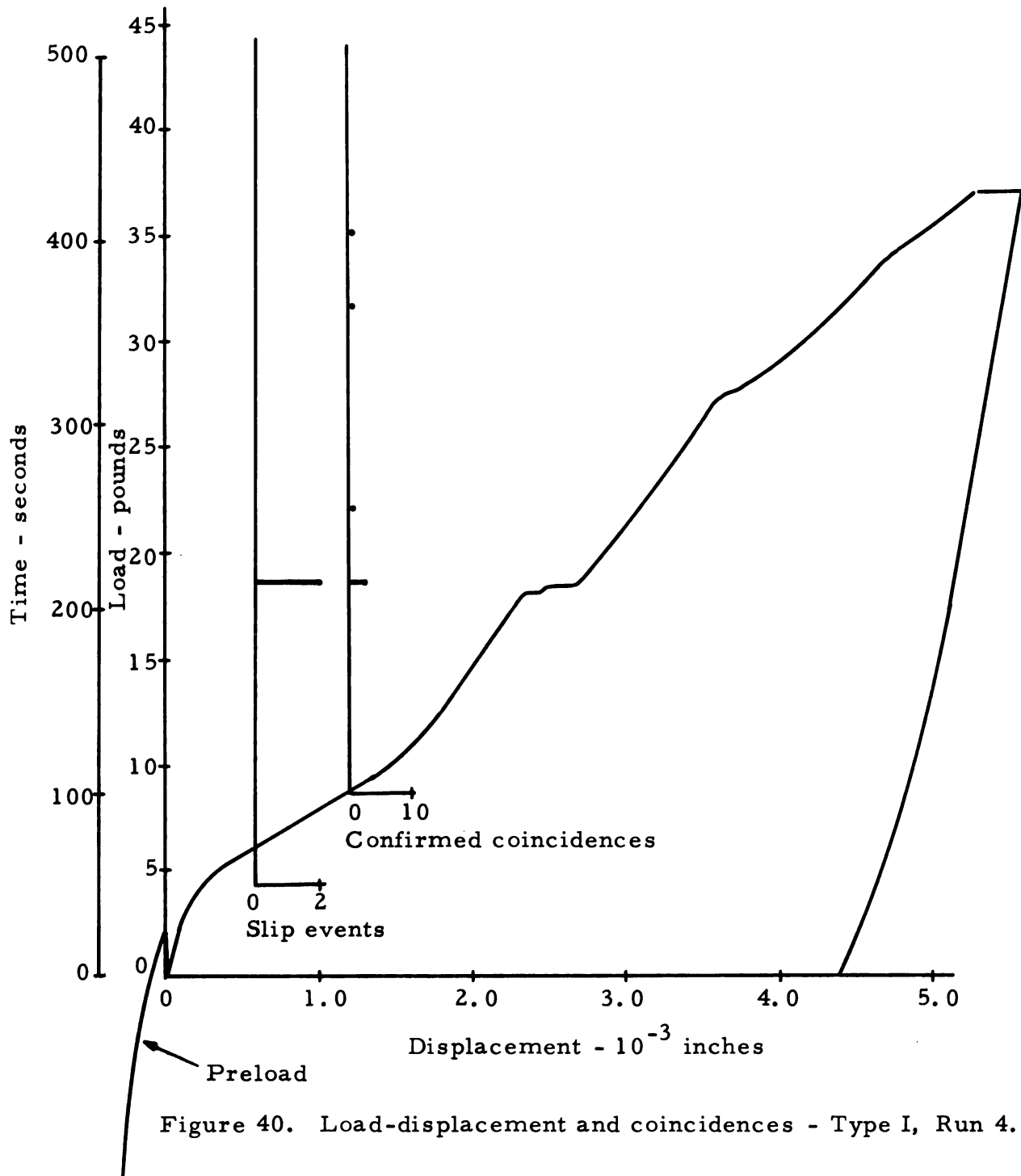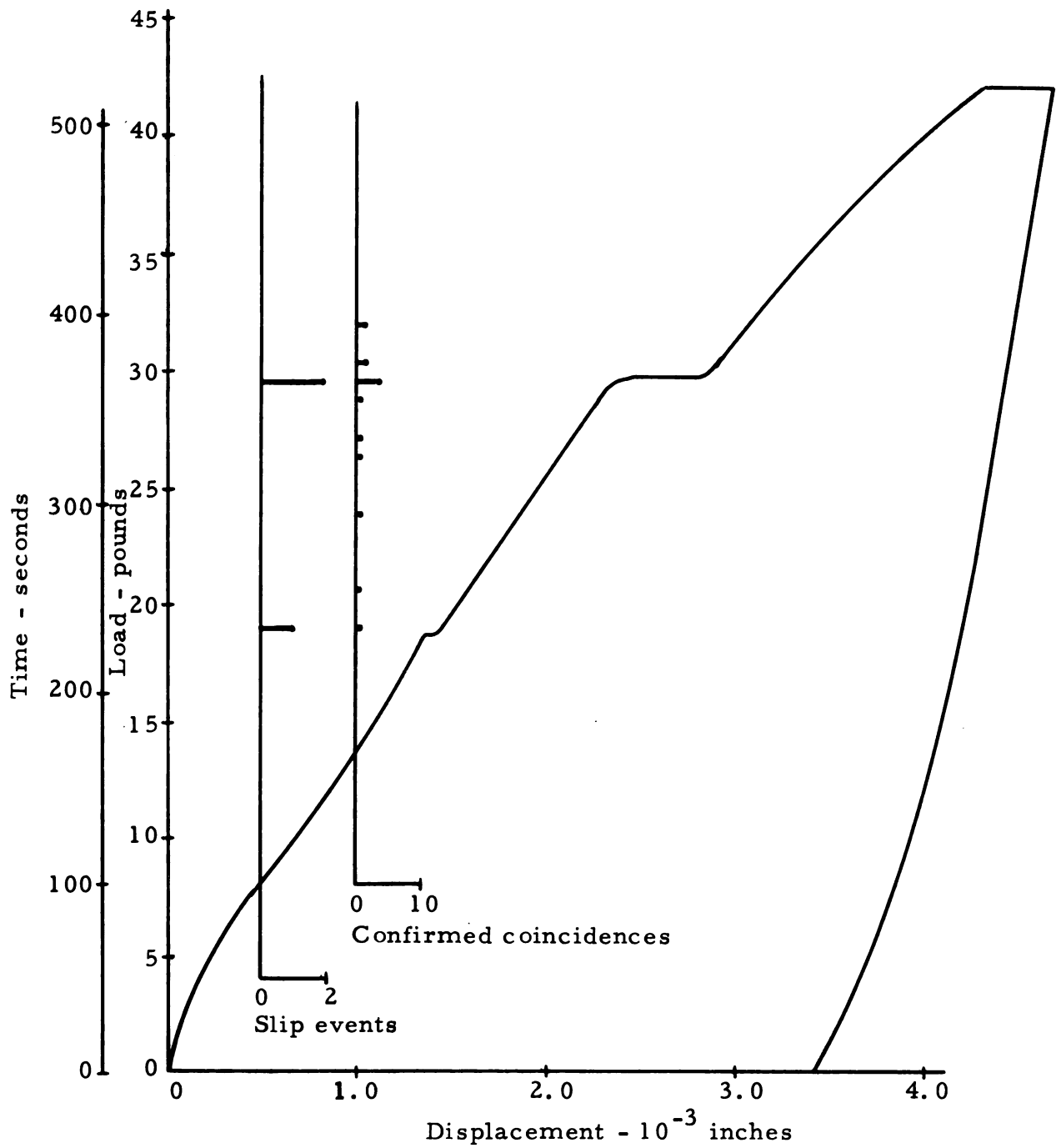
Figure 41. Load-displacement and coincidences - Type I, Run 9.
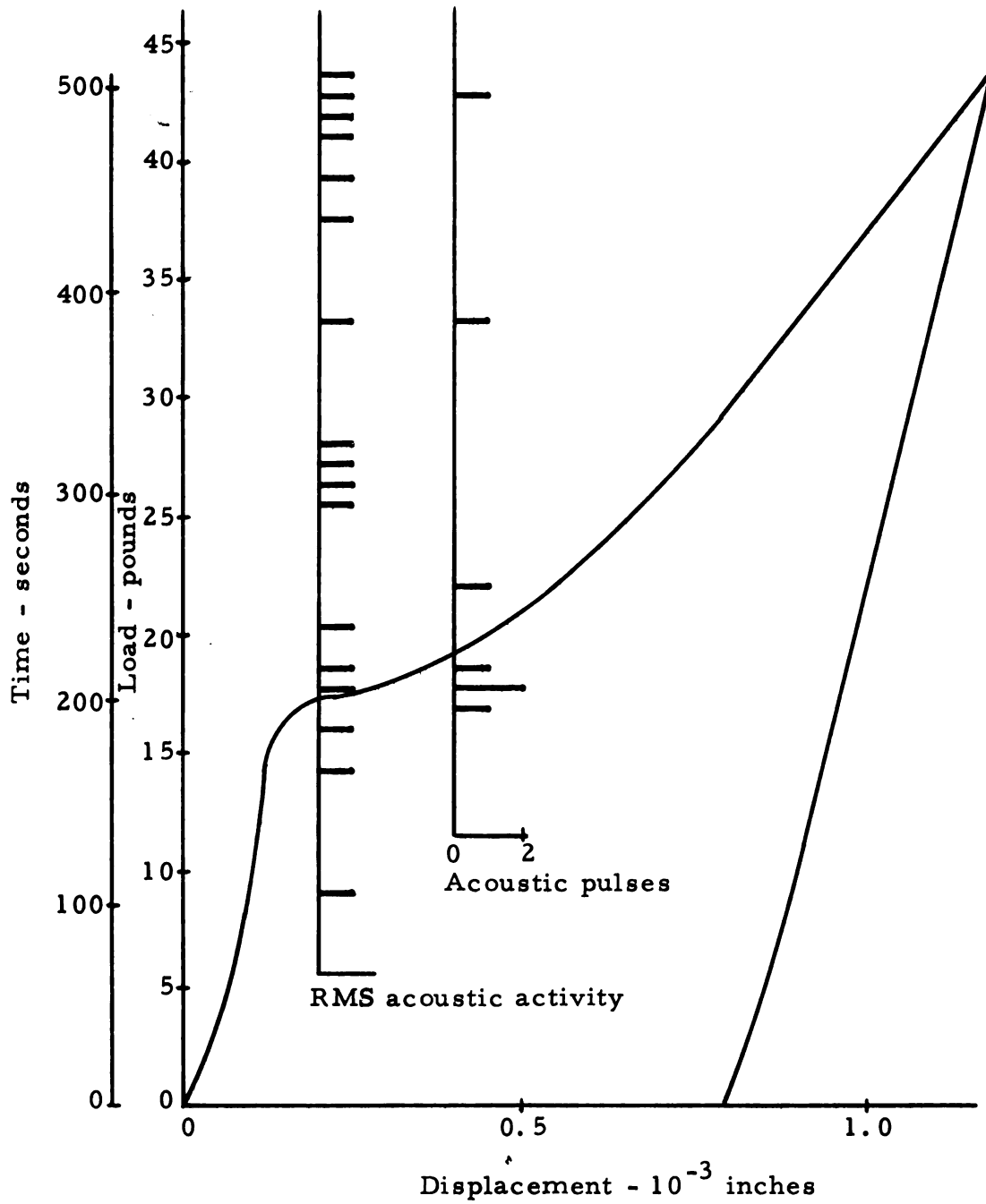
Figure 42. Load-displacement and acoustic emission - Type I, Run 13.
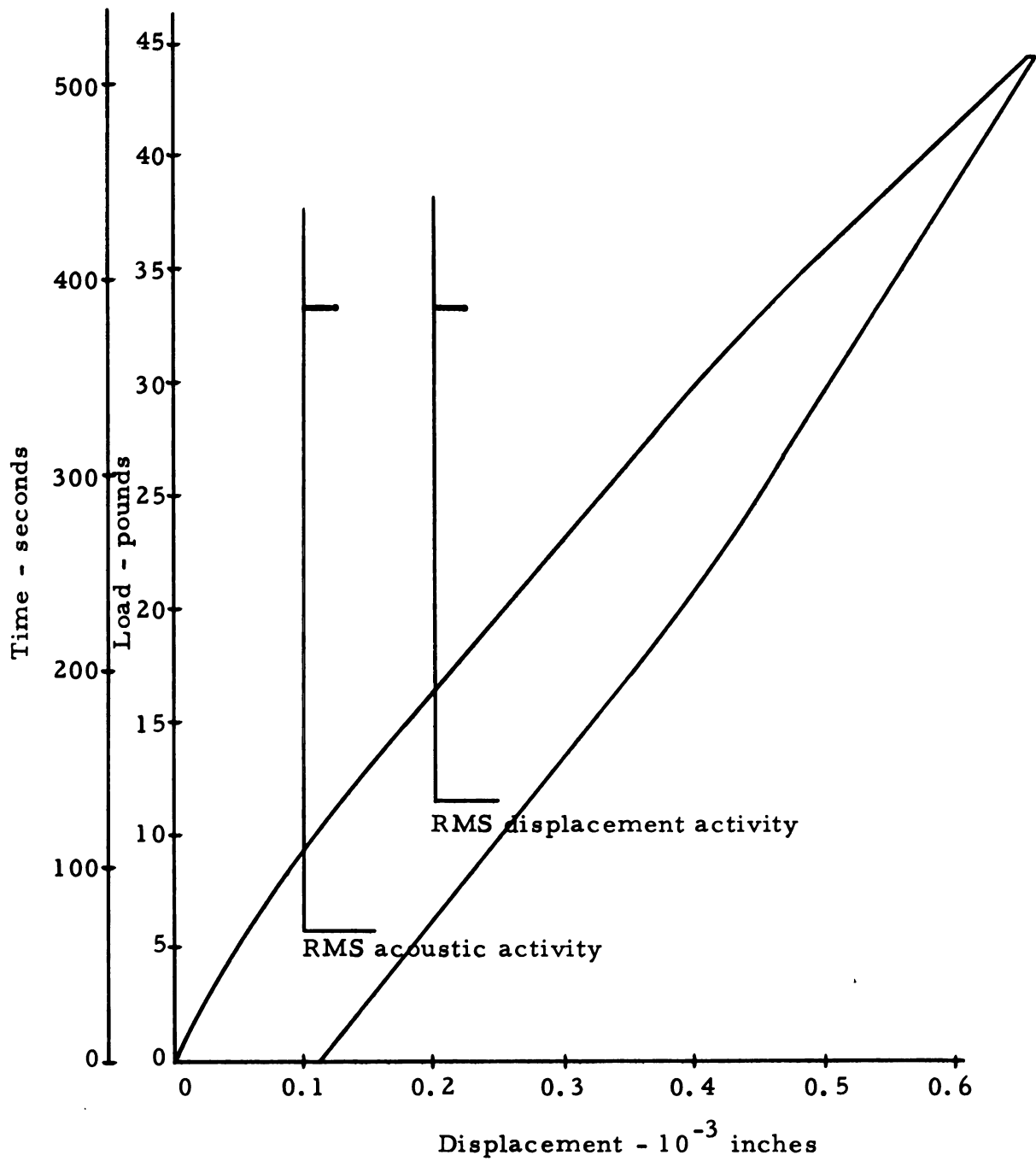
Figure 43. Load-displacement and RMS activity - Type II, Run 12.
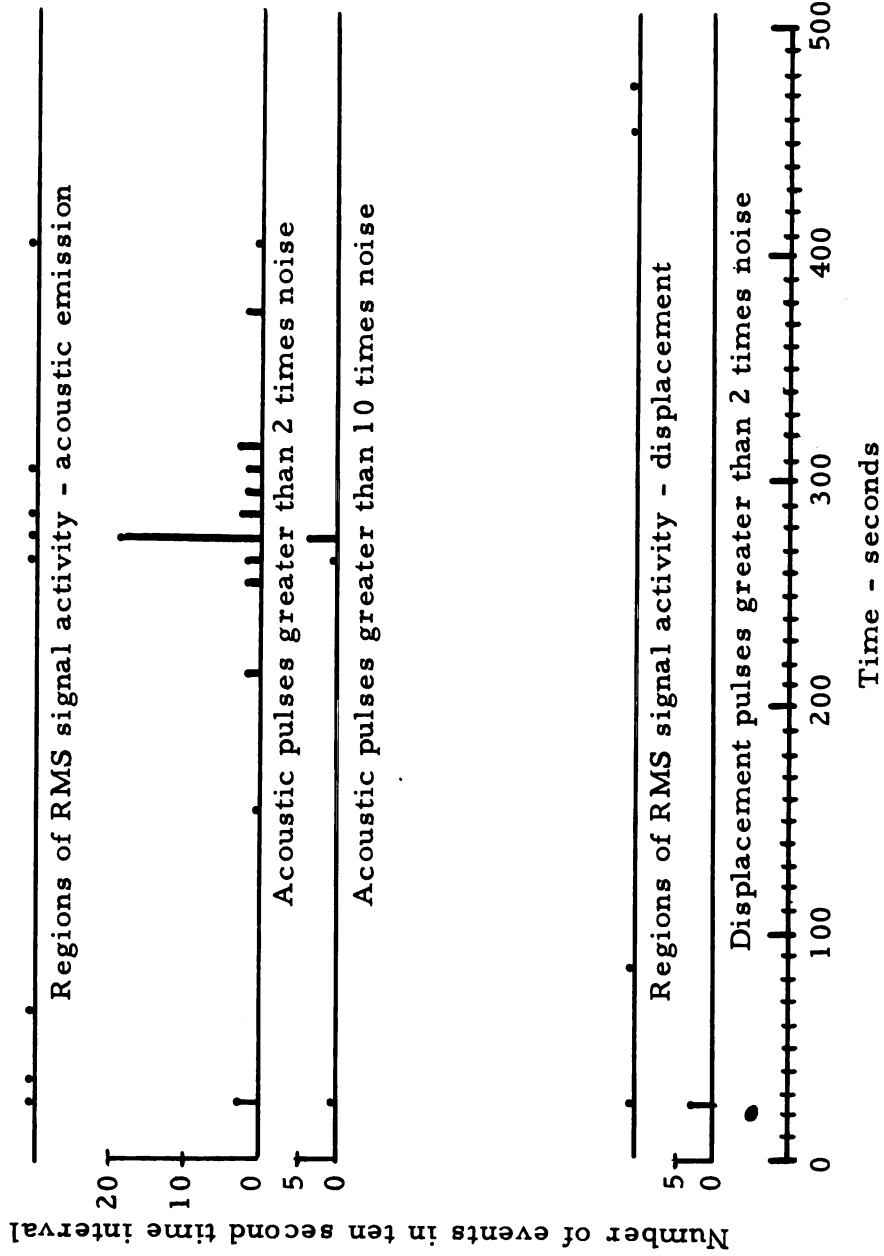
Figure 44. Acoustic emission and displacement pulse distributions - Type III, Run 14.
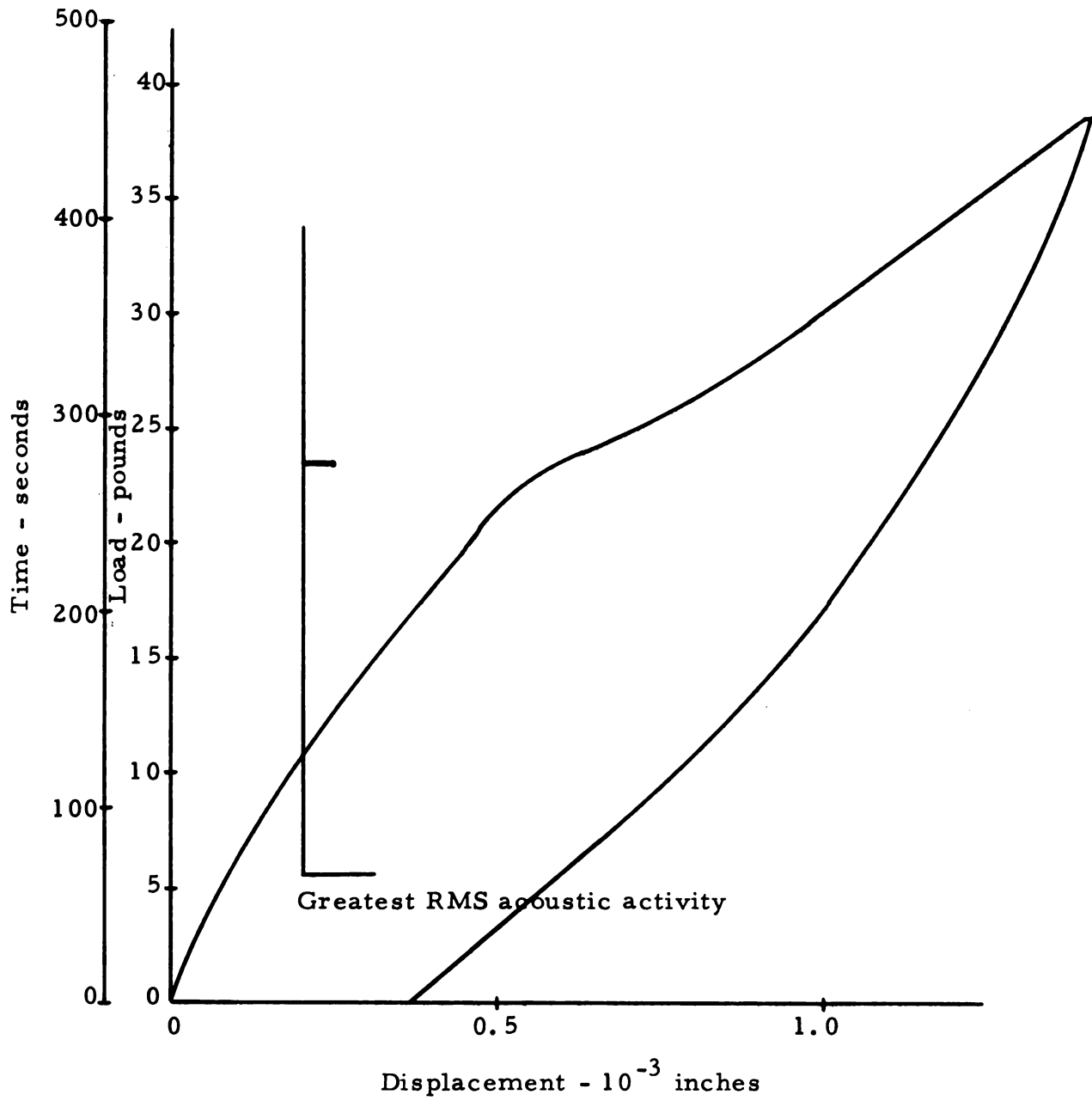
Figure 45. Load-displacement and acoustic emission - Type III, Run 14.

the polarizing microscope. No dislocations could be observed, how-ever, since the Burgers vectors for any operative dislocations were at an angle to the plane of the polarizer and analyzer of the microscope.

Only one Type IV crystal was tested. It fractured on a principal cleavage plane as was expected. The load-displacement curve for this test, Run 11, appears in Figure 31. When this crystal was observed under the microscope, it was discovered that conjugate slip had occurred throughout the crystal, even in the clamped region. Since the clamping pressure and distributed load from the clamp would place maximum shear stresses on the conjugate slip planes, this conjugate slip was not surprising. No pulse height analysis was attempted for this run.

DISCUSSION

The large acoustic emission pulses are the most interesting feature of this experiment. They appear only after an appreciable amount of plastic deformation of the Type I, easy-glide specimens (between 10% shear strain for Run 3 and 60% shear strain for Run 7). At least two phenomena are represented by these pulses, manifested by the presence or absence of large, nearly simultaneous displacement pulses, previously referred to as coincident displacements. In order to explain the behavior observed during the tests, it is necessary to examine how the transducers respond to rapid displacements and acoustic emission events.

Because the moving element of the displacement transducer was mounted at the end of a cantilever beam made of epoxy-fiber glass laminate, some delay is to be expected between displacements at the test specimen (located at the base of the cantilever beam - refer to Figures 9 and 18) and the corresponding displacements at the moving plate. This delay is the time required for a flexural stress wave to travel to the capacitor location. Using 3.33×10^6 pounds per square inch for the flexural modulus of the beam material, 0.144 pounds per cubic inch for its specific weight, $v = (Eg/\gamma)^{1/2}$ for the velocity of the flexural stress wave, and 3 inches for the distance between the test specimen and the capacitor plate, gives an expected delay of approximately 30 microseconds.

Because the acoustic emission transducer is in direct contact with the test specimen, within 1/8 inch of the acoustic emission source,

the time delay between the emission event in the crystal and the excitation of the transducer is estimated to be less than 1 micro-second.

If an acoustic emission and a step displacement occur at exactly the same time, the emission signal should lead the displace-ment pulse by about 30 microseconds. Additional delays introduced by the electronics are of no consequence since both electronic systems are identical, except for the cathode follower coupling the displace-ment transducer to its preamplifier which introduces negligible delay.

Oscilloscope traces of coincident events (Figures 37, 46, and 55 through 58) clearly show that these delays range from about 1000 to 7500 microseconds, indicating an internal acoustic emission mechanism rather than emission simultaneous with dislocation egress at the surface.

It is assumed that the displacement transducer responds to dynamic events when dislocations actually leave the crystal producing a slip line or step at the surface. The presence of large acoustic emission pulses without corresponding displacement, shown in Figures 32 and 34, indicate that the lattice vibrations that appear as acoustic emission signals are not large enough to effect the displacement transducer. This supports the assumption that all displacement signals are due to the egress of dislocations at the surface. The isolated acoustic emission pulses also suggest the presence of a second internal mechanism for acoustic emission.

The following mechanisms are proposed for the acoustic emission process. Acoustic emission is the direct result of crystal lattice vibrations, and the source of energy to cause these vibrations

must be internal to fit the observations described above. When
dislocations interact with obstacles, assumed to be relatively
stationary in the crystal lattice, they exert forces on the obstacles.
These forces, in turn, are transmitted to the region around the
obstacle and produce a local increase in the elastic strain energy.
When the driving force, due to the applied stress and dislocation
pile-up behind the obstacle, is sufficient to force dislocations past
the obstacles, the distorted region will relax to a configuration with
smaller strain energy. The excess strain energy will be available
to excite lattice vibrations if the breakaway process is rapid.

A second possible mechanism arises when the obstacle or
barrier is quite strong. In this case, the stress concentration
produced at the tip of the piled-up group of dislocations may cause
breakaway or be strong enough to force dislocations to coalesce and
nucleate a crack, which will propagate to relieve the local excess of
elastic strain energy. In either event, an acoustic emission would
be expected: accompanied by a displacement pulse if the piled-up
group reaches the surface and produces a step displacement, or
with no displacement pulse if a crack forms. Groups of moving
dislocations also may be expected to produce acoustic emission when
they collide with obstacles in their slip planes, a portion of their
kinetic energy appearing as lattice vibrational energy.

Acoustic emission accompanying the formation of piled-up
groups is unlikely, because the pile-up process is quasi static,
producing a gradual buildup of potential energy. The pile-up process
followed by breakaway, therefore, causes groups of dislocations to

act more or less coherently and enhances possible emission by collision. If no pile-up occurs, collision emission is possible only if dislocation velocities are high. High velocities are not generally associated with normal plastic deformation. However, the effect of pile-up is to apply greatly magnified forces on leading dislocations producing high velocities, which make collision emission more probable.

A transfer of elastic strain energy to lattice vibration similar to the breakaway process, though involving lower total energy, occurs whenever a segment of a pinned dislocation acts as a dislocation source. The cross-glide dislocation multiplication mechanism proposed by Koehler[35] and Orowan[36] and verified by Johnston and Gilman[29] conceivably can produce acoustic emission. However, if this is the case, many more acoustic emission pulses should be evident during the tests. In lithium fluoride, glide band dislocation densities remain constant at about 10^7 per square centimeter until glide bands fill the entire test section[25]. This occurs at about 1% compressive strain (about 1.5% shear strain). Densities of 10^4 to 10^5 per square centimeter are characteristic of as-grown lithium fluoride crystals.

A calculation based on the above dislocation densities and the lateral area of the test section of the specimens predicts that 24,000 dislocations will be produced before 1.5% shear strain is reached. The total emission count is much smaller than this; therefore, dislocation multiplication must not be a primary contributor to the emission process. Improved emission signal-to-noise ratio may make it possible to observe the multiplication process.

The loader used for this experiment is partially responsible for the behavior observed for the Type I, easy-glide crystals. It is not possible to cause dislocations to reach high velocities with hard testing machines unless high strain rates are imposed, with a resulting high stress rate. In such a machine at slow strain rates, plastic flow will produce a decrease in the applied stress and allow moving dislocations to decelerate. If a low strain rate is imposed on the specimen only low velocities will be observed. The loader in this experiment is a gravity loader that, though the load rate is quite low, maintains the applied load on the specimen as it deforms plastically. This feature of the loader tends to maintain the dislocation velocities because the applied stress does not decrease with plastic flow. A similar test with a hard machine will show a drop in load associated with the emission produced by breakaway rather than a large slip deformation as is observed in this experiment. The ability of the loader to follow rapid displacements depends somewhat on the angle of tilt because the pendulum is relatively massive. Near the no-load position (no-tilt), the component of weight causing acceleration of the pendulum is quite small.

Returning to the high level acoustic emission, the proposed model predicts emission due to catastrophic breakaway of dislocation groups and due to the formation of cracks. There are enough isolated high level emissions, as large as those associated with coincident displacement pulses, to point to crack formation as the source. In fact, all crystals producing isolated high level emission also exhibit internal cracks. No cracks form in specimens that do not exhibit high level emission.

The high level emission pulses with associated displacement pulses are interpreted in terms of the model as being due to catastrophic breakaway of groups of dislocations accelerated to high velocity, producing what has been referred to previously as instantaneous slip events.

That the high level emission does not appear until at least 10% shear strain occurs is a strong indication that obstacles involved in the pile-up process leading to the emission are the result of large plastic deformation rather than obstacles already present in the crystal. Line defects or trails[29] produced by dislocations moving on slip planes are a likely prospect for the blocking obstacles.

The number of dislocations involved in the instantaneous slip events and an estimate of dislocation velocities are obtained from calculations based on the data listed in Table 2, taken from the oscillograph record and oscilloscope pictures of events in Run 7. The calculations are based on the following assumptions.

The events are assumed to be due only to the breakaway process. The most likely number of distinct emission events is 2N, twice the number of spikes appearing on the oscilloscope trace; because phase differences cause the transducer to respond to only half of the impulses on the average, as explained earlier on pages 43-45. The time required to accelerate dislocations to terminal velocities is negligible, since Gilman and Johnston[25] indicate that terminal velocities are reached in less than 1.7 microns of travel. The distance traveled by the dislocations is the entire width of the crystal, 1/8 inch; and last, the transit time for dislocations involved

in the events is given by m/n, the ratio of the group size to the number of dislocations per second that must leave the crystal to accommodate the displacement magnitudes.

The number n is fixed by the displacement magnitude Δ and the time T during which the displacement occurs,

$$n = \Delta / |\hat{b}| T , \qquad (1)$$

where $|\hat{b}|$ is the magnitude of a unit glide dislocation (22.3 x 10^{-9} inches). The time T can be taken either as the delay time between the acoustic emission and displacement pulses or as the duration of the acoustic emission signal. The latter is taken as the appropriate time for two reasons. The displacement transducer shows secondary excitations that occur at the end of the acoustic emission signals due to deceleration as the base of the transducer stops, and the proposed model requires that dislocations be moving immediately after the initial emission and during subsequent collision emission events. The emission signals suggest that the actual dislocations move not as single large groups but as several smaller groups, possibly piled-up at different obstacles in their slip planes; and the delay between the acoustic emission and displacement pulses is then more indicative of the position of the pile-up nearest the surface of the crystal when breakaway initiates. The number m is uncertain, ranging from 1, if only one dislocation moves at any given time, to $m = \Delta / |\hat{b}|$, if all of the dislocations involved move simultaneously. One estimate of the average value of m can be obtained by assuming that

$$\overline{m} = \Delta/2N|\hat{b}| \qquad (2)$$

where $\Delta/|\hat{b}|$ is the total number of dislocations involved and $2N$ represents the number of distinct emission events, each assumed to be due to the independent, isolated motion of a single group of dislocations.

The dislocation velocity is obtained using

$$v = d/t = \frac{1/8}{m/n} = n/8m . \qquad (3)$$

In the case where $m = 1$ the upper limit velocity is obtained,

$$v_u = n/8m = \Delta/8|\hat{b}| \; T; \qquad (4)$$

if $m = \Delta/|\hat{b}|$, the lower limit velocity

$$v_l = 1/8T \qquad (5)$$

is obtained; and if $m = \overline{m} = \Delta/2N|\hat{b}|$,

$$\overline{v} = 2N/8T \qquad (6)$$

results. The various velocities resulting from these relations and the data from Table 2 are shown in Table 3 for the coincident events of Run 7.

The upper limit velocity is unreasonable since both the emission and displacement pulse signals indicate concerted motion of large groups of dislocations is the most likely displacement mechanism. The average velocity calculated from the average group size is a more reasonable upper limit. The actual dislocation velocity may be expected to be less than the upper limit because several groups may move at the same time,

Table 3. Dislocation velocities for coincident events – Type I, easy-glide, Run 7.

Time of event	Number of emission signal spikes	Magnitude of displacement	Duration of emission pulse	Total number of dislocations	Average group size	Lower limit velocity	Average velocity	Upper limit velocity	Average applied shear stress
	N	Δ	T	$\Delta/|\hat{b}|$	$\Delta/2N|\hat{b}|$	$v_1=1/8T$	$\bar{v}=2N/8T$	$\Delta/8|\hat{b}|T$	τ_o
sec		10^{-6} in	10^{-3} sec			in/sec	10^2 in/s	10^3 in/sec	psi
186	75	50	32.2	2240	15	3.88	5.81	8.70	491
292	28	6	11	269	4.8	11.35	6.36	3.06	741
381	34	15	19.6	673	9.9	6.38	4.34	4.29	1010
436	23	0	6.5	–	–	0	0	0	1160 *
	35	10	15	449	6.4	8.34	5.84	3.74	**
	58	10	21.5	449	3.9	5.82	6.74	2.61	***
465	36	10	15	449	6.2	8.34	6.00	3.74	1235
467	–	11	15	494	–	8.34	–	5.61	1235
478	80	72	30	3230	22	4.17	6.68	13.5	1270

$|\hat{b}| = 22.3 \times 10^{-9}$ in.

* Reflects 6.5 millisecond delay between acoustic and displacement pulse
** Includes only that portion of emiss on signal during displacement pulse
*** Includes total emission pulse.

causing an effective increase in the value of m in the relation

$v = n/8m$. The value of $\overline{m}$ is too small to be representative of the

group size that makes the main contribution to the displacement

and acoustic emission. The displacement signals indicate that the

displacement proceeds by the motion of a few, possibly one or two,

large groups and many small ones, rather than the movement of

groups uniformly distributed about the mean value. The large

groups will have the largest effect; therefore, the proper value for

m to determine the group velocity lies between $\overline{m}$ and $\Delta/|\hat{b}|$.

That the leading portion of the displacement pulses have amplitudes

much larger that the noise level equivalent, and the average group

size ranges from 4 to 22 dislocations, which is on the same order of

magnitude as the smallest detectable pulse, supports the above

statements. Appendix B, listing the acoustic channel gains and

displacement pulse sensitivities, shows that the smallest countable

displacement pulse is related to the egress of at least nine unit

dislocations for Run 7. If several groups move at the same time,

or if the predominant group size is actually larger, the dislocation

velocity will approach the lower limit.

The velocities calculated above for instantaneous slip events

are based on the assumption that the only mechanism operating is the

breakaway of piled-up dislocation groups. The proposed model allows

for emission accompanying crack formation and propagation, as well

as collision processes. There is no reason for excluding these

additional sources and they probably act simultaneously with the break-

away process. If either one makes a contribution to the acoustic

emission signal used to determine the number of acoustic

emission events occuring during the step displacement, the effect is to cause a high value of N (the number of spikes recorded in the emission signal). A reduction in N reduces the average velocity, given by

$$\bar{v} = 2N/8T, \qquad (6)$$

though it has no effect on the lower limit velocity.

Figure 46, especially, suggests the possibility of simultaneous slip and crack formation. The initial acoustic emission may be associated with the formation and propagation of a crack, with the remaining burst being due to the breakaway process.

The collision process is equally probable but its occurrence is unlikely without prior breakaway emission. Though the process of dislocation pile-up can be considered as a collision process, it will progress slowly, with only one dislocation at a time coming to rest at an equilibrium position. Once a group collects at an obstacle, the subsequent release of a nearly coherent group will produce conditions conducive to collision emission. Any obstacle in the slip plane of the moving group is expected to interact with the group to impede its progress and produce collision emission which, in turn, will cause a high spike count and a correspondingly high estimate of the average dislocation velocity.

In all, three types of acoustic emission are observed: the two types of high level emission pulses just discussed, associated with crack formation and breakaway of large dislocation groups that reach average velocities of about 500 to 600 inches per second, and low level

Emission 2 v/cm

5 milliseconds/cm

Displacement 0.2 v/cm
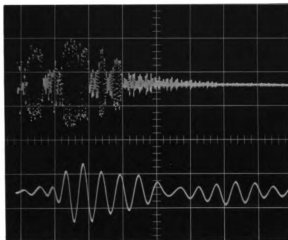
Emission 0.5 v/cm
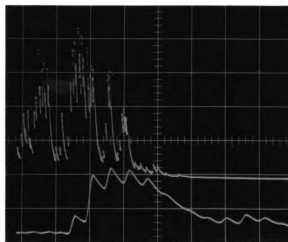
5 milliseconds/cm

Displacement 0.01 v/cm

Figure 46. Oscilloscope traces - event at T = 436 seconds -
Type I, Run 7.

acoustic emission with no coincident displacement pulses. Smaller displacement pulses also are observed with no apparent acoustic emission (see Figure 33, Run 7). Three of the largest non-coincident displacement pulses are just detectable in Figure 34 between T = 190 and T = 245 seconds. Such non-coincident acoustic emission and displacement pulses are expected, according to the model of the emission process, when small groups of dislocations piled-up behind weak obstacles are finally forced to break away and move through the crystal. Since these groups must be much smaller than the smallest group associated with instantaneous slip, the driving force on the leading dislocations is smaller and lower velocities result.

The combined effect of low velocity and unknown position of origin produces much longer and variable delays between the acoustic emission associated with the breakaway and the corresponding displacement pulse, making it difficult to determine correlations between them except on a statistical basis. A close look at the acoustic emission and displacement signals between T = 190 and 245 seconds (Figure 34) shows that there are emission pulses preceding each isolated displacement pulse by about three seconds. If these emission pulses are associated correctly with the delayed displacement pulses (the absence of other activity in the region makes this likely), and if the group of dislocations is assumed to have traveled the entire width of the crystal, the related dislocation velocity becomes v = 1/8x3 or about 0.04 inches per second.

As a result of the low velocity, secondary emission by the collision process is improbable. For such small groups of dislocations, the terminal velocity of the group is probably similar to the bulk of the dislocations causing plastic flow. This is especially true for these three delayed events because the load angle is still small and, as discussed earlier, the ability of the loader to maintain the dislocation velocity is limited. The low level emission without coincident displacements therefore seems quite reasonable since the delay between the emission and corresponding displacement is variable; and, furthermore, many of these breakaway groups, being small and moving with low velocities, will become pinned again by other obstacles before they can leave the crystal. With a low velocity the individual dislocations of the group are not as apt to continue moving coherently through the crystal,which increases the possibility that they pile-up on other obstacles in their slip planes without producing collision emission and without resulting displacement pulses.

The general appearance of the load displacement curves for all runs indicates that the bulk of the plastic deformation is smooth. This suggests that the deformation results from random motion of small groups of less than 9 dislocations (Run 7).

An estimate of the upper limit dislocation velocity in this case is obtained from the load-displacement curve from Run 7, typical of the easy-glide tests. The average loading slope, away from the regions of instantaneous slip, is very nearly 248×10^3 seconds per inch of displacement. The unloading slope is 1090×10^3 seconds per inch of displacement. The corresponding relative velocities (velocity

of the top part of the test crystal relative to the bottom part) are 4.03 $\times 10^{-6}$ inches per second and 0.92 $\times 10^{-6}$ inches per second. The difference between these velocities represents the relative velocity due to plastic flow, since the unloading process is essentially elastic. This plastic flow velocity is 3.11 $\times 10^{-6}$ inches per second and may be attributed to the motion of groups of less than nine unit dislocations, because few detectable displacement pulses are observed in these regions of the load-displacement curve.

The plastic flow velocity divided by the length of the unit Burgers vector for an easy-slip dislocation (22.3 $\times 10^{-9}$ inches) indicates the number of dislocations that must leave the crystal in one second to accommodate the velocity: about 140 unit dislocations per second for Run 7.

Let $v = d/t$ inches per second represent the dislocation velocity, where t represents the time in seconds required for an edge dislocation to travel entirely through the crystal, a distance of 1/8 inch. If n represents the rate with which dislocations leave the crystal (dislocations per second) and m represents the number of dislocations moving at any given time, $t = m/n$ seconds and v becomes $n/8m$ inches per second. For any given value of n, the upper limit velocity occurs when $m = 1$ which represents the case when only one dislocation is moving at any given time. The upper limit dislocation velocity in the case of the smooth plastic flow observed during Run 7 ($n = 140$ per second) is, therefore, 17.5 inches per second. This approximation, as before, ignores any finite accelerations the dislocations experience.

In this case, no estimate of a lower limit velocity is made, because no measurement to determine m is possible. However, it is probable that many small groups move simultaneously and independently of each other. For example, if 100 groups of 5 move together, m would become 500 and the resulting dislocation velocity is

$$v = n/8m = 0.035 \text{ inches per second.}$$

This is consistent with the velocity related to the identifiable delayed events discussed earlier.

Reports on dislocation velocities in lithium fluoride[25, 31] indicate that, for any given degree of hardness, dislocation velocity increases with applied stress over an extremely large range. For example, dislocation velocities may range from 2×10^{-5} to 2×10^{-1} inches per second as the applied shear stress varies from 900 to 1400 psi. The dependence appears to be linear in a log log plot. Dislocation velocities as high as 2×10^{5} inches per second are reached with shear stress impulses of 40,000 psi. The dislocation velocity appears to approach the velocity of $(110)[\bar{1}10]$ shear waves asymptotically. Tests on a single crystal do not reflect the effects of work hardening. However, additional tests on softer and harder crystals indicate that hardening causes a constant increase in the stress for all velocities up to about 0.4 inches per second. Figure 48 qualitatively represents the above results.

The upper limit dislocation velocity of 17.5 inches per second for the smooth plastic flow of Run 7 appears to be high in comparison with the above data. The large number of dislocations available to accommodate the deformation, the velocity for the three delayed

displacement pulses, and the more reasonable calculation that considers the motion of many small groups, are in essential agreement with the above results.

The dislocation velocities for the instantaneous slip events also appear to be high. Neither the lower limit nor the upper limit shows any regular stress dependence and the lower limit is higher than would normally be expected. The average dislocation velocity for these events appears to be constant for all stress levels. There are several reasons for these apparent discrepancies. The results quoted[25,31] are from measurements involving single dislocations moving in essentially virgin crystal, while the dislocation velocities for the instantaneous slip events reported here are for large groups of dislocations initially piled-up at obstacles. The effect of the pile-up is to magnify the driving stress on the leading dislocation by approximately the number of dislocations piled up behind it, and the effective driving stress is much higher than the applied stress appearing in Gilman and Johnston's reports. Consequently, generally higher velocities are to be expected. This is illustrated in Figure 47 by the two points on line c which indicate the expected velocity, v_a, based on the applied shear stress, τ_a, and the velocity, v_c, resulting from the actual driving stress, τ_c. Furthermore, if the loader supplies energy to the system as fast or faster than drag forces on dislocations dissipate it, the dislocations can be expected to maintain their velocity, or even continue to accelerate. This feature of the loader is described earlier.

Lack of a definite relation between stress and velocity is partially explained by the actual value of the driving stress being unknown. An-
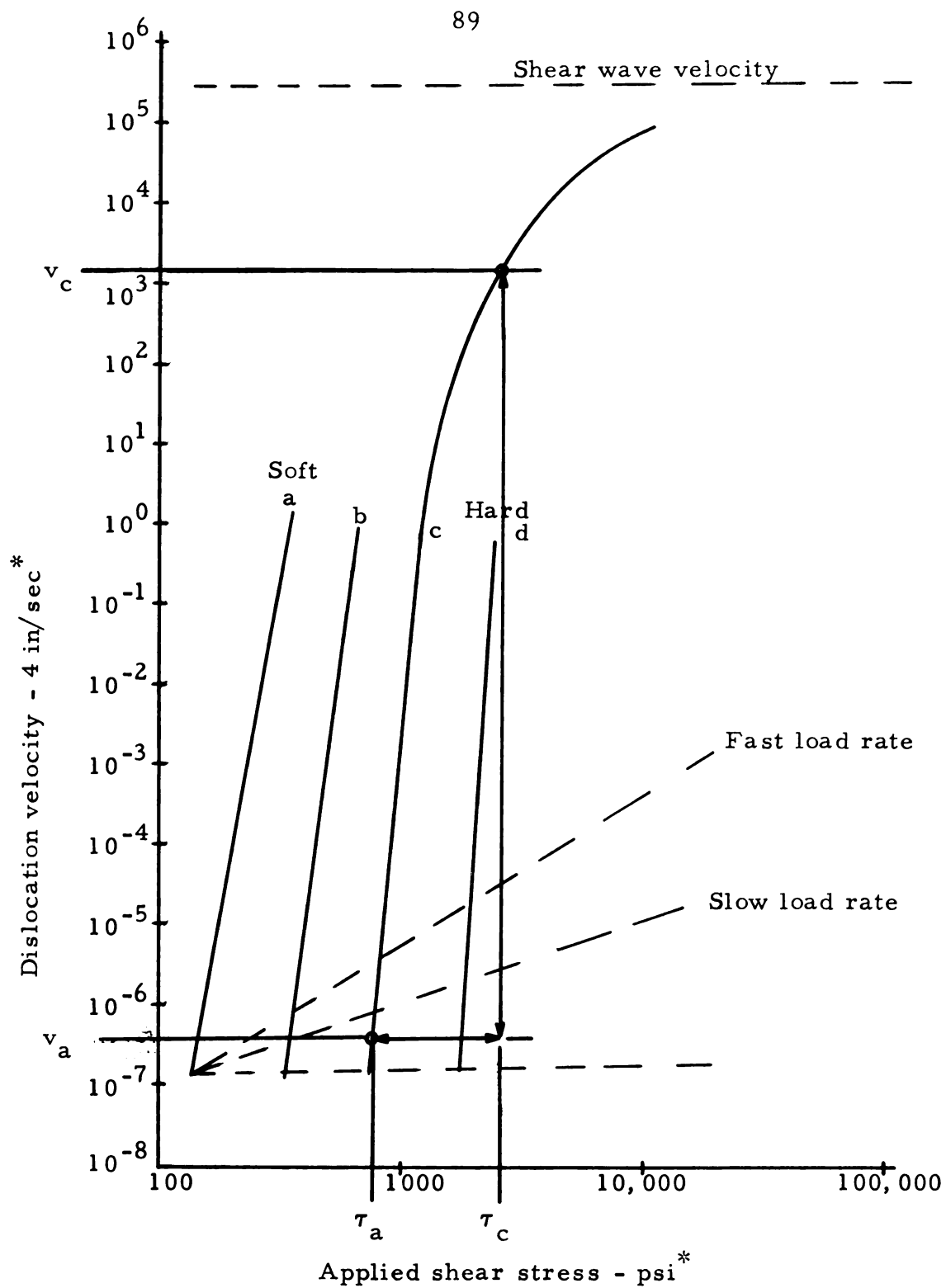
$*$ Plot is intended to represent qualitative features only.

Figure 47. Dislocation velocity versus applied shear stress.

other factor is the extremely low load rate and essentially unrestricted deformation of the present test. For example, the total plastic deformation for Run 7 is 2.9×10^{-3} inches at a load rate of five pounds per minute (approximately 100% shear strain at a stress rate of 160 psi per minute). Such plastic deformation must cause a great amount of work hardening which reduces the stress dependence of dislocation velocity. This effect is shown by the dashed lines superposed on Figure 47. Under these conditions, the higher velocities seem not unreasonable. No direct velocity comparisons are possible, since the relative purities, as-grown dislocation densities, and hardness of the crystals are not known.

Signal amplitude comparisons between acoustic emission and displacement signals, both pulse and RMS, give no definite correlations. Large displacements can be expected to have large acoustic emission pulses associated with them, but large acoustic emissions due to crack formation are not accompanied by displacement pulses. Furthermore, the collision emission process that is very likely in conjunction with breakaway emission during instantaneous slip events adds an amount to the emission signal that depends more upon the number and type of collisions than upon the actual magnitude of the displacement. However, lack of pulse height correlation is due primarily to the irregularity of the acoustic emission pulses, because the RMS displacement signals are found to be related to the instantaneous slip displacements in the following way:

$$\text{(RMS amplitude)}^{1/2} = K\Delta \ . \tag{7}$$

Measurement of such small changes in displacement presents several difficulties. The displacement sensitivity of the basic transducer is somewhat selectable, ranging between 900 and 2500 volts per inch, depending upon the initial settings of the displacement capacitor spacing. These sensitivities are achieved with the sacrifice of linearity, though the range of displacement is small and resulting changes in sensitivity are either negligible or can be corrected by use of calibration data.

The biggest difficulty is to separate the small rapid changes in displacement from the D. C. component of the signal that represents the total displacement. Three problems appear here. They are signal-to-noise ratio, frequency response of the transducer, and true reproduction of the rapid step displacements. A basic sensitivity of 1000 volts per inch produces a change of 22.3 microvolts for the egress of one unit dislocation. Therefore, a noise level of 0.4 millivolts peak-to-peak, such as is typical for this experiment, effectively obliterates these low level signals and, in Run 7, limits resolution of dynamic events to those involving more than 10 unit dislocations.

The moving element of the displacement transducer is a relatively massive plate mounted at the end of a plastic beam. Its low natural frequency, about 400 Hz, limits its ability to follow rapid step displacements and smooths out details of the events. In the present experiment the dynamic sensitivity can be inferred only from the quasi-static sensitivity measured after each run and the gains and attenuations in the signal conditioning and playback equipment. This information is listed in Appendix B.

The third problem is evident in the relationship between displacement pulse RMS amplitude and measured displacements (equation 7),

$$(\text{RMS amplitude})^{1/2} = K\Delta \ ,$$

which is believed to be partly the result of inductive coupling in the displacement pulse channel and partly the result of the mechanical response of the transducer.

Since dynamic displacements are of primary interest, long term stability of the transducer is not important as long as it does not change appreciably during each run. Direct calibrations of the transducer taken several days apart indicated that the long term stability was sufficient for the present experiment. Additional precautions in construction and control of environment will be necessary if a transducer of this type is to be used to measure such small displacements in a creep-type experiment.

It also should be mentioned in conclusion that some of the control specimens also give evidence of low level acoustic emission. In view of the additional load components (tension and flexure) applied to the crystals, the presence of low level acoustic emission from these control specimens is to be expected. The lack of displacement pulses during these control tests is due to the restrictive load geometry which makes easy-glide difficult unless the easy-glide plane is also the load plane.

CONCLUSIONS

Dynamic displacements with magnitudes on the order of 2×10^{-7} inches and greater can be detected with the equipment and techniques reported here. More exact measurement of such small dynamic displacements and resolution of displacements on the order of 2×10^{-8} inches and smaller are believed practical with improvements suggested in the next section.

Acoustic emission is due to lattice vibrations set up when excess elastic strain energy, stored in the volume around a blocking obstacle. as a result of dislocation pile-up on the obstacle, is released or allowed to relax rapidly. In lithium fluoride the method of release may be the breakaway of the dislocation group or the formation of a crack. Secondary emission can be produced as a result of collision processes between coherent moving groups of dislocations or high velocity single dislocations and blocking obstacles. The former is most likely, since single dislocations would rarely attain sufficient velocity to cause an emission before they become pinned by obstacles in their glide plane. The pinning process that causes groups of dislocations to collect is instrumental to the secondary emission process: it is the resulting stress concentration which causes group velocities sufficient to produce secondary collision emission.

The acoustic emission behavior observed for the easy glide specimens can be qualitatively characterized by using the proposed model. The easy-glide crystals exhibit plastic behavior immediately upon loading. This is evidenced by the immediate, rapid occurrence of low level

93

acoustic emission from the breakaway of small groups of less than

nine dislocations, or from the activation of Frank-Read sources in the

crystal. Displacement pulses are expected and observed with no

particular value of time delay between emission and displacement

pulses, because groups large enough to produce a displacement

pulse are moving with low velocity, and the time delay is dependent

upon the location of the blocking obstacle in the particular slip

plane. Furthermore, due to the low velocity, many moving groups

may be blocked again by other obstacles, producing collision

emission without accompanying displacement pulses.

After slip bands entirely fill the test section, line defect

trails resulting from cross-glide dislocation multiplication provide

increasing numbers of strong blocking obstacles for easy-glide, and

cause the collection of larger piled-up dislocation groups. No high-

level emission is expected before slip bands are completely developed;

since before this point is reached, there is virgin crystal in which

dislocation multiplication and easy-glide can take place. The stress

concentration at the leading edge of such a group is sufficient to produce

breakaway emission and accelerate much of the group to high velocity,

creating an instantaneous slip event with coincident displacement

pulses. Due to the high velocity attained and the increased number

of blocking obstacles in the slip plane, collision emission is expected

to be common under breakaway conditions. The additional mechanism

of crack nucleation and propagation adds to the signals observed during

the instantaneous slip events and also makes its own contribution, as

evidenced by the presence of large emission pulses with no associated

displacement pulses - either coincident or delayed. Low level emission and non-coincident displacement pulses, related to the breakaway of small groups with low velocities, continue throughout the test, producing the bulk of the smooth plastic deformation.

The data and the associated emission process model suggested above are in complete agreement with independent conclusions by Schofield[15] and Tatro[37] that the emission process is due to an internal, volumetric, rather than an external, surface mechanism.

The model also agrees with Schofield's results indicating that high frequency emission requires a strain rate above a certain minimum value. The low level emission observed in this experiment corresponds to the high frequency emission observed by Schofield. Since the emission mechanism proposed here is essentially a dynamic mechanism, and the rate of dislocation multiplication and pile-up, as well as collision processes, are quite strain-rate dependent, low velocity dislocations associated with low strain rates would not produce detectable emission pulses at the noise levels presently achieved.

It is possible to relate the burst-type emissions observed by Schofield in some materials to the breakaway process apparent in lithium fluoride. As in lithium fluoride, which shows burst-type emissions due both to cracking and dislocation breakaway, other materials have been shown to produce emission by other mechanisms, such as micro-twinning in zinc and stacking fault formation in gold. Such emission is to be expected, since these processes are characterized by a rapid change in structure, relieving local elastic strain energy concentrations.

However, the emission identified as low level in the present experiment, and high frequency in the work of others, is most probably due to the internal breakaway and collision processes proposed here. Each material may be expected to exhibit burst-type emission dependent upon crystallographic structure.

The model satisfactorily explains the early results of other experimenters, notably Liptai[18], who related emission to surface effects. The emission he observed in aluminum with thick anodized and reacted coatings was no different than that proposed in this case. The effect of the coatings was to cause a preponderance of dislocation pile-ups at the interface between the aluminum and the coating layer; and since the resulting release of dislocation groups was concentrated near the surface, other internal sources would be masked. The early experiments by Schofield and Tatro on aluminum indicated a surface mechanism because the oxide coating, normally present on aluminum, enhances the breakaway contribution at the surface. The same would be true of any surface treatment that tends to harden a surface layer of the specimen.

SUGGESTIONS FOR FURTHER RESEARCH

The conclusion that low level emission is associated with discrete displacements needs to be reinforced with additional data amenable to statistical analysis. In order to do this with a series of experiments similar to the present one, it will be necessary to improve signal-to-noise ratios in both the emission and displacement-pulse channels, and to improve the upper frequency response of the displacement transducer. The region where strain is less than 1.5% is of primary interest, since this is where the basic breakaway process predominates: crack formation is absent because stress concentrations are small, and secondary collision emission is less apt to play an important role because velocities are low.

Pulse height correlation will be much more meaningful in this region with other mechanisms suppressed. With good correlations between acoustic emission pulse heights and displacement pulses, reasonable measures of the energy involved in the basic breakaway emission process should be made. Theoretical consideration of the additional energy stored in the crystal lattice due to the interaction of piled-up groups and blocking obstacles will be necessary to allow a better understanding of the breakaway emission process.

Secondary collision emission in the region between 1.5% strain and 10% strain or higher should be interesting from the viewpoint of studying the phenomenom of work hardening in crystalline materials.

The present loader is not capable of controlled strain rates or of load rates higher than five pounds per minute. Further research on the relations between dislocation velocity, stress, and work hardening

should be pursued with a programmable loader capable of a wide range of load and strain rates.

Continued improvement of signal-to-noise ratio of the displacement transducer will improve the dynamic displacement resolution and allow detection of single dislocation egress. A reduction in noise by a factor of ten will be sufficient, and is believed practical.

Better load geometry will allow redesign of the moving element of the displacement transducer to allow stiffer supports and a less massive moving plate. The resulting shift to higher natural frequency will allow detection of more displacement details. .

Circuitry should be designed to allow more direct measurement of the rapid step displacements. One possibility that should be investigated is formation of a second displacement signal with high frequency components filtered out. A difference amplifier could then be used to compare the direct signal with the smoothed one and pick off rapid displacement changes without using capacitative or transformer coupling.

BIBLIOGRAPHY

1. Orowan, E., and Becker, R., _Zeit. Physik_, Volume 79, (1932).

2. Klassen-Nekludowa, M., _Zeit. Physik_, Volume 55, (1929).

3. Crussuard, C., Leon, J. B., Plateau, J., and Blacket, C., "Sur la formation d'ondes sonores, au cours d'essai de traction, dans des eprouvettes metalliques", _Comptes rendus des seances de l'Acadamie des Sciences_, Volume 246, seance du 19 mai, (1958).

4. Blewitt, T. H., Coltman, R. R., and Redman, J. K., "Low Temperature Deformation of Copper Single Crystals", _Journal of Applied Physics_, Volume 28, Number 6, June, (1957).

5. Schmid, E., and Valanck, M. A., _Zeit. Physik_, Volume 75, (1932).

6. Kaiser, J., "Untersuchungen uber das Auftreten von Gerauschen beim Zugversuch", Doctoral thesis, Munich Technische Hochschule, (1950).

7. Kaiser, J., _Arkiv Für das Eisenhüttenwessen_, Volume 24, pg. 43-44, (1953).

8. Tatro, C. A., "Sonic Techniques in the Detection of Crystal Slip in Metals", _Engineering Research_, Volume 1, Progress Report, The Engineering Experiment Station, College of Engineering, Michigan State University, (1957).

9. Tatro, C. A., "Sonic Techniques in the Detection of Crystal Slip in Metals", Division of Engineering Research, Progress Report, Michigan State University, January, (1959).

10. Tatro, C. A., "Acoustic Emission from Crystalline Materials Subjected to External Loads", Division of Engineering Research, Progress Report, Michigan State University, April, (1960).

11. Tatro, C. A., and Liptai, R. G., "Acoustic Emission from Crystalline Substances", Paper presented at the Symposium on Physics and Nondestructive Testing, Southwest Research Institute, October, (1962).

12. Schofield, B. H., Bareiss, R. A., and Kyrala, A. A., "Acoustic Emission Under Applied Stress", WADC Technical Report 58-194, April 30, (1958).

13. Schofield, B. H., "Acoustic Emission Under Applied Stress", ARL 150, December, (1961).

14. Schofield, B. H., "Acoustic Emission Under Applied Stress", ASD-TDR-53-509, Part I, April, (1963).

15. Schofield, B. H., "Acoustic Emission Under Applied Stress", ASD-TDR-63-509, Part II, May, (1964).

16. Schofield, B. H., "Investigation of Applicability of Acoustic Emission", AFML-TR-65-106, May, (1965).

17. Shoemaker, P. S., "Acoustic Emission, An Experimental Method", M. S. thesis, Michigan State University, (1961).

18. Liptai, R. G., "An Investigation of the Acoustic Emission Phenomenon", Ph. D. thesis, Michigan State University, (1963).

19. Liptai, R. G., and Tatro, C. A., "Acoustic Emission - A Surface Phenomenon", Paper presented at the Symposium on Nondestructive Testing of Aircraft and Missile Components, Southwest Research Institute, February, (1963).

20. Sedgwick, R. T., "An Investigation of Acoustic Emission from Coated and Uncoated Ionic Crystals", Ph. D. thesis, Michigan State University, (1965).

21. Taylor, G. I., Proceedings of the Royal Society, A, Volume 145, pg. 362, (1934).

22. Orowan, E., Zeit. Physik, Volume 89, pg. 605, 614, 634, (1934).

23. Polanyi, M., Zeit. Physik, Volume 89, pg. 660, (1934).

24. Gilman, J. J., and Johnston, W. G., "Dislocations, Point-Defect Clusters, and Cavities in Neutron Irradiated LiF Crystals", Journal of Applied Physics, Volume 29, Number 6, June, (1958).

25. Johnston, W. G., and Gilman, J. J., "Dislocation Velocities, Dislocation Densities, and Plastic Flow in Lithium Fluoride Crystals", Journal of Applied Physics, Volume 30, Number 2, February, (1959).

26. Gilman, J. J., "Plastic Anisotropy of LiF and Other Rocksalt-Type Crystals", Acta Metallurgica, Volume 7, September, (1959).

27. Gilman, J. J., "Dislocation Sources in Crystals", Journal of Applied Physics, Volume 30, Number 10, October, (1959).

28. Gilman, J. J., and Johnston, W. G., "Behavior of Individual Dislocations in Strain-hardened LiF Crystals", Journal of Applied Physics, Volume 31, Number 4, April, (1960).

29. Johnston, W. G., and Gilman, J. J., "Dislocation Multiplication in Lithium Fluoride Crystals", Journal of Applied Physics, Volume 31, Number 4, April, (1960).

30. Gilman, J. J., "Direct Measurements of the Surface Energies of Crystals", Journal of Applied Physics, Volume 31, Number 12, December, (1960).

31. Gilman, J. J., and Johnston, W. G., "Dislocations in Lithium Fluoride Crystals", Solid State Physics, Volume 13, Academic Press, (1962).

32. Sproull, R. L., "Charged Dislocations in Lithium Fluoride", Phil. Mag., Volume 55, Number 56, August, (1960).

33. Lion, K. S., Instrumentation in Scientific Research, pg. 86, McGraw-Hill, 1959.

34. Lion, K. S., "Mechanic-Electric Transducer", The Review of Scientific Instruments, Volume 27, Number 4, April, (1956).

35. Koehler, J. S., "The Nature of Work-Hardening", Physical Review, Volume 86, Number 1, January, (1952).

36. Orowan, E., in Dislocations in Metals, pg. 103, American Institute of Mining and Metallurgical Engineers, New York, (1954).

37. Tatro, C. A., private communication.

Appendix A.   Equipment List

Item	Used For
1. Decker 02B-1-4D general purpose probe.	Sensor for differential capacitor (displacement).
2. Decker 904 delta unit.	Sensor power supply.
3. Tektronix type 122 low-level preamplifier.	Preamplifier for emission and displacement pulse signals.
4. Tektronix type 532 oscilloscope with type 53/54D plug in unit.	Amplifier and monitor for emission and displacement signals. Gate signal generator for pulse height analysis and time counter.
5. Variable electronic filters; Spencer Kennedy model 302, Spencer Kennedy model 308, Krohn-Hite model 335R.	Filters for recording and readout.
6. Ampex FR-1100 tape recorder-reproducer.	Data storage.
7. Sorensen ACR 2000 voltage regulator.	Line voltage regulator and filter to remove fast transients. Power for tape recorder.
8. CEC type 5-119 recording oscillograph.	Multi-channel data recording.
9. Galvanometer drivers: CEC type 1-162A galvanometer-driver amplifier, Brush Instruments universal amplifier model RD-5612-00.	Galvanometer drivers for 5-119 oscillograph.
10. Baldwin SNB3-06-12S6 semiconductor strain gages.	Load bridge.
11. Ellis BAM-1 bridge amplifier.	Load bridge amplifier.
12. Varian model F-80 X-Y recorder.	Load-displacement plot.
13. Tektronix type 180 A time mark generator.	Time reference signal.

14. Nuclear-Chicago model 151A   Time reference counter.
    electronic counter.

15. Ballantine Laboratories, Inc.   Provide RMS signal for readout.
    model 320 true root-mean-
    square voltmeter.

16. Hewlett Packard model 522B   Counter for pulse height
    electronic counter.   analysis.

17. Tektronix type 130 L-C meter.   Monitor for measuring initial
    capacitance of differential
    capacitor.

18. Tektronix type 564 storage   Coincident pulse pictures.
    oscilloscope with 3A1 dual
    trace amplifier and 2B67
    time base plug in units.
    Type C-12 oscilloscope camera.

19. Hewlett Packard 200CD   Calibration and setup signal
    oscillator, Arenberg 93 ohm   and monitor.
    attenuator, Hewlett Packard
    400A RMS voltmeter, and
    Tektronix type 551 dual beam
    oscilloscope with 53/54D and
    53E/54E plug in units.

20. Cohu 510 digital voltmeter.   Meter to set initial balance of
    displacement transducer cathode
    followers.

21. Harrison Lab 6204A D.C.   Zero suppression for displace-
    power supply.   ment signal recorded on 5-119
    oscillograph.

22. ADP crystal stack.   Acoustic emission transducer.

Appendix B

Acoustic channel gains and displacement pulse sensitivities.

Run Number	Acoustic gain True 10^4	Relative to Run 7	Displacement sensitivity True 10^6 volt/in	Relative to Run 7	Displacement Noise level equivalent 10^{-7} in	$|\vec{b}|$ **
		{110}<110> Type I				
3_{0-120}*	2.42	1.11	9	43.7		
$3_{120-230}$	2.42	1.11	18	87.4		
$3_{230-420}$	2.42	1.11	45	218	2.78	12.5
$3_{420\text{ on}}$	1.21	0.55	45	218		
4	1.21	0.55	22.1	107	0.184	0.84
7	2.2	1	0.206	1	1.95	8.75
9	0.11	0.05	0.129	0.63	1.94	8.7
10	0.55	0.25	0.059	0.29	10.9	48.9
13	0.55	0.25	0.396	1.93	3.15	14.1
		{100} <110> Type II				
5	0.55	0.25	0.758	***		
12	0.55	0.25	0.595	2.88	2.1	9.4
		{110} <100> Type III				
6	2.2	1	0.218	1.06	10.9	48.9
14	0.22	0.1	0.396	1.93	1.57	7.04
		{100} <100> Type IV				
11	0.22	0.1	0.396	1.93		

*   Subscripts indicate time interval during run if not constant for entire run.

**   Number of unit dislocations equivalent to smallest countable pulse. $1 |\vec{b}| = 22.3 \times 10^{-9}$ inches.

***   Displacement pulse data not recorded due to use of 2 Khz high-pass filter.

Appendix C. Load-displacement data.

Run 3, Type I			Run 4, Type I	
Loading			**Loading**	
Displacement 10^{-3} in	Load lb		Displacement 10^{-3} in	Load lb
-0.073	-6.66		-0.457	-16.79
-0.028	-3.06		-0.420	-14.77
0	0		-0.289	-9.51
+0.050	+3.89		-0.149	-2.22
0.105	7.94		+0.038	+2.63
0.194	11.99		+0.029	+1.82
0.250	13.84		0	0
0.316	15.49		+0.047	+1.82
0.361	17.14		0.159	3.44
0.416	18.74		0.252	4.25
0.488	20.74		0.457	5.47
0.538	20.99		0.625	6.28
0.572	22.29		1.110	8.30
0.616	23.94		1.465	9.92
0.716	26.19		1.539	10.32
0.733	26.49		2.062	15.18
0.783	26.64		2.345	18.08
0.883	28.29		2.435	18.08
0.994	30.14		2.509	18.48
1.050	30.94		2.677	18.48
1.094	31.59		2.789	20.78
1.194	33.14		3.218	23.28
1.272	34.19		3.536	26.78
1.338	35.34		3.703	27.68
1.438	37.09		4.207	29.98
1.516	38.44		4.748	34.08
1.627	39.44		5.047	35.53
1.694	40.34		5.271	37.08
Unloading			**Unloading**	
0	0		0	0
0.042	2.45		0.15	2.23
0.109	6.42		0.45	9.51
0.146	8.75		0.63	15.58
0.220	13.56		0.86	23.80
0.298	19.05		1.01	29.05
0.387	26.00		1.12	34.15
0.476	32.20		1.16	35.55
0.598	42.80			

Run 5, Type II

Displacement 10^{-3} in	Load Lb
Loading	
-0.167	-13.29
-0.145	-6.28
-0.102	-1.61
-0.058	+0.68
-0.044	+1.17
-0.015	+0.23
0	0
+0.015	+0.44
0.044	2.19
0.174	4.82
0.319	7.74
0.464	10.66
0.595	13.87
0.682	16.79
0.798	20.59
0.900	23.51
0.987	26.41
1.103	28.81
1.205	31.26
1.393	35.41
1.466	37.11
1.582	39.71
1.756	41.81

Unloading

Mean slope 71.23 lb/10^{-3} in

Run 6, Type III

Displacement 10^{-3} in	Load Lb
Loading	
0	0
0.071	1.50
0.324	4.51
0.607	9.52
0.688	11.53
0.768	13.78
0.870	16.79
1.011	21.80
1.112	25.56
1.213	29.57
1.314	33.33
1.395	36.58
1.517	41.10
1.618	44.35
1.674	46.11

Run 6 continued

Displacement 10^{-3} in	Load Lb
Unloading	
0	0
0.087	3.51
0.188	8.77
0.218	11.28
0.239	12.03
0.259	13.53
0.299	16.29
0.360	20.80
0.441	27.56
0.542	35.58
0.603	40.09
0.643	43.35

Run 7, Type I

Displacement 10^{-3} in	Load Lb
0	0
0.045	1.30
0.125	3.64
0.250	5.78
0.348	6.85
0.530	8.14
0.635	8.83
0.745	9.68
0.930	11.45
1.110	13.34
1.285	15.37
1.330	15.37
1.370	15.70
1.410	16.41
1.552	19.71
1.630	20.77
1.730	22.19
1.865	23.96
1.880	24.29
1.936	25.30
2.045	26.08
2.175	28.21
2.265	30.10
2.330	31.68
2.370	31.98
2.545	35.29
2.585	36.23
2.602	36.23
2.690	38.00
2.730	38.62
2.765	38.66

Run 7 continued Displacement 10^{-3} in	Load Lb
2.810	39.63
2.888	39.63
2.950	40.72
3.055	43.32
3.120	44.59
3.180	45.44

Unloading

0	0
0.026	1.30
0.068	3.89
0.111	6.49
0.175	11.09
0.240	15.93
0.282	19.71
0.335	24.20
0.410	31.04
0.452	34.82
0.516	40.48
0.559	44.50

Run 9, Type I

Displacement 10^{-3} in	Load Lb
0	0
0.034	1.49
0.116	3.06
0.229	4.89
0.544	8.29
0.776	10.90
0.973	13.51
1.181	16.39
1.357	18.58
1.425	18.69
1.506	19.53
1.656	21.62
1.761	22.66
1.981	25.28
2.268	28.67
2.448	29.59
2.828	29.59
2.888	30.37
3.018	31.81
3.258	34.16
4.048	40.44
4.268	41.87

Run 9 continued

Displacement 10^{-3} in	Load Lb

Unloading

0	0
0.16	2.54
0.40	7.50
0.57	11.95
0.68	15.34
0.80	19.13
0.96	25.80
1.11	33.64
1.20	36.91
1.25	39.39
1.28	41.87

Run 10, Type I

Displacement 10^{-3} in	Load Lb

Loading

0	0
0.076	6.94
0.177	14.69
0.278	20.29
0.369	23.23
0.480	26.97
0.581	30.71
0.682	34.44
0.783	38.72
0.884	42.72
0.955	45.39

Unloading

0	0
0.051	2.40
0.152	9.21
0.201	12.68
0.354	25.37
0.480	39.38
0.495	45.39

Run 11, Type IV

Displacement 10^{-3} in	Load Lb
0	0
0.050	4.03
0.101	7.66
0.151	11.18
0.202	14.29
0.252	17.30
0.303	19.88

Run 11 continued Displacement 10^{-3} in	Load Lb
0.353	22.11
0.404	23.96
0.454	25.36
0.505	26.33
0.565	27.14
0.656	27.94
0.777	28.48
0.787	28.50
Fracture	

Run 12, Type II

Displacement 10^{-3} in	Load Lb
Loading	
0	0
0.035	3.82
0.166	13.78
0.207	16.74
0.278	21.59
0.338	25.63
0.378	28.32
0.409	30.21
0.459	33.17
0.590	40.98
0.656	44.34
Unloading	
0	0
0.052	3.55
0.133	9.48
0.229	16.21
0.396	29.94
0.466	36.40
0.517	40.71
0.560	44.34

Run 13, Type I

Displacement 10^{-3} in	Load Lb
Loading	
0	0
0.105	10.85
0.135	15.70
0.226	17.31
0.266	17.58
0.327	18.12
0.367	18.52
0.509	20.95

Run 13 continued Displacement 10^{-3} in	Load Lb
0.569	22.69
0.700	26.73
0.761	28.62
0.811	30.23
0.872	32.39
1.124	41.27
1.185	43.37
Unloading	
0	0
0.045	3.85
0.121	11.93
0.212	23.23
0.313	34.81
0.387	43.37

Run 14, Type III

Displacement 10^{-3} in	Load Lb
Loading	
0	0
0.030	2.68
0.091	5.95
0.162	9.12
0.384	17.70
0.424	19.04
0.464	20.43
0.585	23.46
0.626	23.92
0.686	24.53
0.787	26.14
0.898	28.15
0.979	29.76
1.110	32.44
1.200	34.32
1.342	37.27
1.382	38.07
1.398	38.34
Unloading	
0	0
0.010	0.27
0.378	9.65
0.550	14.21
0.651	17.96
0.792	24.13
0.974	34.05
1.034	38.34

Run 3, Type I

Key to columns
Column 1 - ten second time interval ending at time indicated in seconds.
Column 2 - displacement pulses in ten second time interval with pulse
 height between 0.5 and 1.0 volts.
Column 3 - displacement pulses with pulse heights between 0.3 and 0.5
 volts.
Column 4 - displacement pulses with pulse heights between 0.25 and
 0.3 volts.
Column 5 - total of columns 2, 3, and 4.
Column 6 - emission pulses with pulse heights between 5 and 10 volts.
Column 7 - emission pulses with pulse heights between 2.5 and 5 volts.
Column 8 - emission pulses with pulse heights between 1 and 2.5 volts.
Column 9 - emission pulses with pulse heights between 0.5 and 1 volt.
Column 10 - emission pulses with pulse heights between 0.25 and 0.5 volts.
Column 11 - total of columns 6 through 10.
Column 12 - positively identified RMS coincidences.
Column 13 - RMS coincidences that were not enough above background to
 be considered for column 12.
Column 14 - confirmed coincidences between displacement and acoustic
 emission pulses.

Time Interval	Displacement pulses				Acoustic emission pulses						Coincidences RMS		Pulse
1	2	3	4	5	6	7	8	9	10	11	12	13	14
5													
15													
25													
35													
45												1	
55													
65													
75									19	19			
85									2	2			
95													
105												2	
115		2		2									
125									1	1			
135		1		1				1		1	1		
145							2	2		4	1		
155						2		1	8	11	1		
165	1			1				1	4	5			1
175									22	22			
185							1		2	3			
195		2		2				2	2	4			
205							1	1	1	3			
215							2		2	4	1		

Run 3   continued

Time Interval	Displacement pulses				Acoustic emission pulses						Coincidences RMS	Pulse	
1	2	3	4	5	6	7	8	9	10	11	12	13	14
225								1	1	2			
235							2		4	6		1	
245	9	10		19	1		2	4	10	17	1	2	1
255			10	10	1		2	1	4	8	1		
265		1	8	9					2	2			
275			12	12		2	1		19	22	1	1	
285			15	15		2		1		3	2	3	2
295			5	5	1	1	2	4	2	10		1	1
305			6	6		4		2	2	8		1	
315	2	11	2	15	2	10	11	14	15	52	1	1	3
325			6	6		5	1	2	11	19	1	1	
335			2	2		1	7	3	11	22			
345			2	2		2	3	5	9	19			
355		1	9	10	2	3	7	3	16	32			3
365			1	1	1	4		22	11	38	1	3	
375			8	8	1	4	13	10	25	53			1
385			7	7	4	6	4	6	34	54		1	1
395			7	7		10	7	14	5	36		1	1
405	2		11	13	2	11	7	1	31	52	2	2	2
415			5	5	3	1	6	3	26	39		2	1
425			6	6	5	3		11	-	19+			2
435			4	4		4	5	2	-	11+		2	
445			4	4·	1	3	5	8	-	17+	1	1	
455			8	8	2	2	2	8	-	14+	2		
465	1		8	9	1	2	3	6	-	12+	1		
475			1	1	1	2	2	8	-	13+	1	1	1
485			2	2	1	2	1	5	-	9+			
495			8	8	1	4	2	2	-	9+		2	
505			4	4	1	1	2	9	-	13+		1	
515		1	4	5		1	1	8	-	10+			
525			5	5	1	1		7	-	9+			
535			2	2			1	6	-	7+			
545							1		-	1+	1	2	
555			3	3				1	-	1+	1	1	
565			4	4					-	0+			
575			3	3				1	-	1+			

Run 4, Type I

Key to columns
Column 1 - ten second time interval ending at time indicated in seconds.
Column 2 - displacement pulses with pulse heights between 0.5 and 1 volt.
Column 3 - displacement pulses with pulse heights between 0.25 and 0.5 volts.
Column 4 - displacement pulses with pulse heights between 0.1 and 0.25 volts.

Column 5 - displacement pulses with pulse heights between 0.05 and 0.1 volts.
Column 6 - displacement pulses with pulse heights between 0.025 and 0.05 volts.
Column 7 - total of columns 2 through 6.
Column 8 - emission pulses greater than 1 volt.
Column 9 - emission pulses with pulse heights between 0.5 and 1 volt.
Column 10 - emission pulses with pulse heights between 0.25 and 0.5 volts.
Column 11 - emission pulses with pulse heights between 0.1 and 0.25 volts.
Column 12 - emission pulses with pulse heights between 0.05 and 0.1 volts.
Column 13 - total of columns 8 through 12.
Column 14 - positively identified RMS coincidences.
Column 15 - confirmed coincidences between displacement and acoustic emission pulses.

Time Interval	Displacement pulses						Acoustic emission pulses						Coincidences	
1	2	3	4	5	6	7	8	9	10	11	12	13	RMS 14	Pulse 15
10					9	9								
20					3	3					7	7		
30					4	4								
40					5	5								
50					3	3								
60					6	6								
70					6	6								
80					2	2								
90					6	6							1	
100					3	3								
110					1	1								
120					3	3					6	6		
130					1	1								
140					3	3								
150														
160											1	1		
170					3	3		1				1		
180					6	6								
190					7	7								
200					9	9			1			1		
210					5	5				1		1		
220	1	1	1	2	13	18	4	4	7	10	20	45	2	3
230					1	1				10		10	1	
240					1	1					1	1		
250					2	2		1				1		
260					1	1		3	3	4	5	15	1	1
270								3		2	1	6		
280					5	5		1	1	3	3	8		
290					1	1		2		5	3	10		
300								1	2	2	4	9		

Run 4 continued

Time Interval	Displacement pulses						Acoustic emission pulses						Coincidences RMS Pulse	
1	2	3	4	5	6	7	8	9	10	11	12	13	14	15
310					2	2			1	5	6	12		
320					2	2				4	13	17		
330					6	6				2	18	20		
340					1	1			4	2	8	14		
350										5	3	8		
360					2	2			1	2	10	13		
370					1	1				2	4	6		
380					1	1			1		4	4	9		
390									1	1	5	3	10		
400					2	2			2	1	6	5	14		
410					2	2			2	2	4	9	17	1	1
420										1	10	12	23		

Run 7, Type I

Key to columns
Column 1 - ten second time interval ending at time indicated in seconds.
Column 2 - displacement pulses greater than 0.1 volts.
Column 3 - displacement pulses with pulse heights between 0.025 and 0.1 volts.
Column 4 - displacement pulses with pulse heights between 0.005 and 0.025 volts.
Column 5 - displacement pulses with pulse heights between 0.0025 and 0.005 volts.
Column 6 - total of columns 2 through 5.
Column 7 - emission pulses greater than 1 volt.
Column 8 - emission pulses with pulse heights between 0.5 and 1 volt.
Column 9 - emission pulses with pulse heights between 0.25 and 0.5 volts.
Column 10 - emission pulses with pulse heights between 0.1 and 0.25 volts.
Column 11 - emission pulses with pulse heights between 0.05 and 0.1 volts.
Column 12 - total of columns 7 through 11.
Column 13 - positively identified RMS coincidences.
Column 14 - confirmed coincidences between displacement and acoustic emission pulses.

Time Interval	Displacement pulses					Acoustic emission pulses						Coincidences RMS Pulse	
1	2	3	4	5	6	7	8	9	10	11	12	13	14
10										2	4	6	
20													
30										4	43	47	
40			1		1					22	58	80	
50									2	39	108	149	
60			1		1					1	39	40	
70											10	10	
80											2	2	

Run 7 continued

Time Interval	Displacement pulses					Acoustic emission pulses						Coincidences RMS Pulse	
1	2	3	4	5	6	7	8	9	10	11	12	13	14
90										3	3		
100										3	3		
110			1		1				5	15	20		
120			1		1					1	1		
130										5	5		
140		1			1					23	23		
150				1	1					3	3		
160			1		1								
170										2	2		
180										4	4		
190	1	1			2	2			1	4	7	1	1
200				1	1					13	13		1
210							1		4	37	42		
220							1		1	20	22		
230							2			24	26		
240							2		1	28	31		
250		1		1	2	2	2	3	3	4	14	2	2
260				1	1	1	3	1	6	6	17		1
270				6	6	2	2	4	8	5	21	1	6
280				2	2	1	1		2	9	13	1	1
290				2	2	1	2	1	1	16	21	1	2
300				2	2	2	2	3	6	19	32	2	2
310				2	2	2	1	2	6	15	26	2	2
320				1	1	2	1	2	3	9	17	1	1
330				3	3	2		1	5	13	21	1	3
340				5	5	1	2	2		4	9		5
350							1		4	3	8		
360						1		2	2	1	6		
370				1	1	1	1	1	1	3	6	1	
380		1		1	2	1				4	5	1	1
390				1	1	1			1		2	1	1
400			1	1	2		1		4		5		2
410									3	5	8		
420									1		1		
430										1	1		
440				2	2	1		1	1	2	5	1	2
450										8	8		
460									1	3	4		
470		1	1	3	5	3			1	2	6	1	5
480	2				2	3		2	7	11	23	1	1
490				2	2			2	5	1	8		
500				1	1		1	2	1	7	11		
510				1	1	1	1	4	4	4	14		1
520						1		2	1	4	8		
530							1	2	2	1	6		
540							1		1	9	11		
550				5	5		3	1		12	16	2	5

Run 7 continued

Time Interval	Displacement pulses					Acoustic emission pulses						Coincidences RMS Pulse	
1	2	3	4	5	6	7	8	9	10	11	12	13	14
560										30	30		
570								1	1	9	11		
580										5	5		
590									1	3	4		
600			1	1						3	3		
610									3	4	7		

Run 9, Type I

Key to columns

Column 1 - ten second time interval ending at time indicated in seconds.

Column 2 - displacement pulses with pulse heights between 0.1 and 0.5 volts.

Column 3 - displacement pulses with pulse heights between 0.025 and 0.1 volts.

Column 4 - displacement pulses with pulse heights between 0.01 and 0.025 volts.

Column 5 - total of columns 2 through 4.

Column 6 - emission pulses greater than 0.5 volts.

Column 7 - emission pulses with pulse heights between 0.25 and 0.5 volts.

Column 8 - emission pulses with pulse heights between 0.1 and 0.25 volts.

Column 9 - emission pulses with pulse heights between 0.05 and 0.1 volts.

Column 10 - emission pulses with pulse heights between 0.025 and 0.05 volts.

Column 11 - total of columns 6 through 10.

Column 12 - positively identified RMS coincidences.

Column 13 - confirmed coincidences between displacement and acoustic emission pulses.

Time Interval	Displacement pulses				Acoustic emission pulses						Coincidences RMS Pulse	
1	2	3	4	5	6	7	8	9	10	11	12	13
10												
20												
30												
40									1	1		1
50			2	2						29	29	
60										29	29	
70										11	11	
80										4	4	
90			1	1						17	17	
100			2	2						3	3	
110										11	11	

Run 9 continued

| Time Interval	Displacement pulses				Acoustic emission pulses						Coincidences	
1	2	3	4	5	6	7	8	9	10	11	RMS 12	Pulse 13
120			1	1					16	16		
130									5	5		
140									9	9		
150									5	5		
160									9	9		
170									2	2		
180									14	14		
190									5	5		
200			1	1					7	7		
210									3	3		
220									10	10		
230									7	7		
240	1	2		3	1				4	5	1	1
250			4	4			3	1	13	17	1	
260			2	2	1		1		9	11	1	1
270									19	19		
280					1	1		1	71	74	1	
290			1	1	3	3			45	51		
300			2	2	1	1			37	39	1	1
310									44	44		
320								1	44	45		
330			3	3	1	1	1	1	70	74		1
340					1	1	1		84	87		1
350					1	1	1	1	99	103		
360			2	2		1			96	97	1	1
370			2	2	6	4		9	67	86	1	4
380		2	3	5	4	4		15	87	110	1	2
390							1	1	29	31		
400			1	1		3	1		13	17		2
410						1	4	2	12	19		
420							1	1	9	11		
430						1	1	1	9	12		
440					1	1	1		10	13		
450							1		3	4		
460					1			1	12	14		
470							1	1	18	20		
480						1	2	2	38	43		
490			2	2		2		1	41	44		
500					1		1	1	56	59		
510							1	2	42	45	1	1
520			1	1			2	2	18	22		
530			1	1					7	7		

Appendix E. Additional data plots.
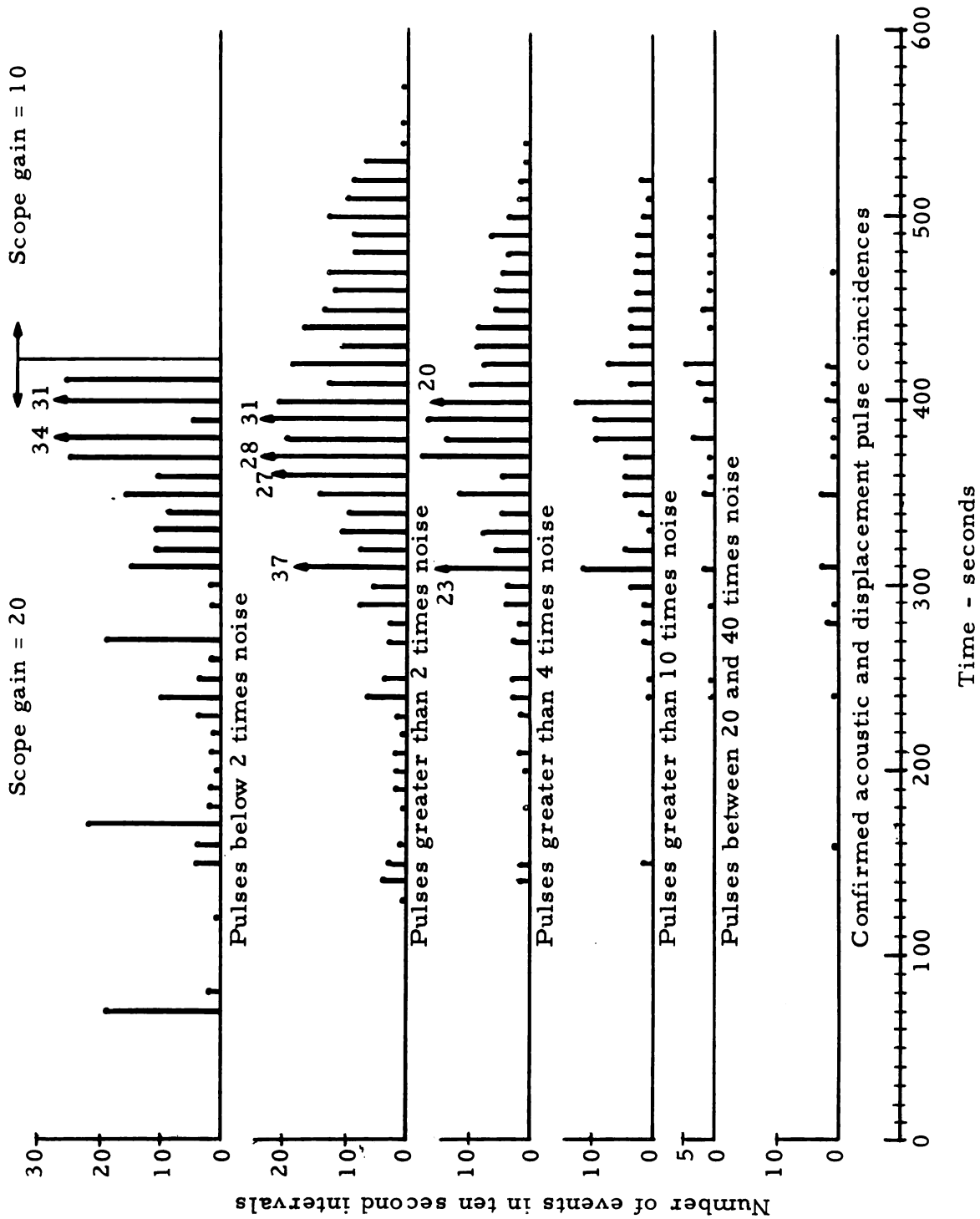
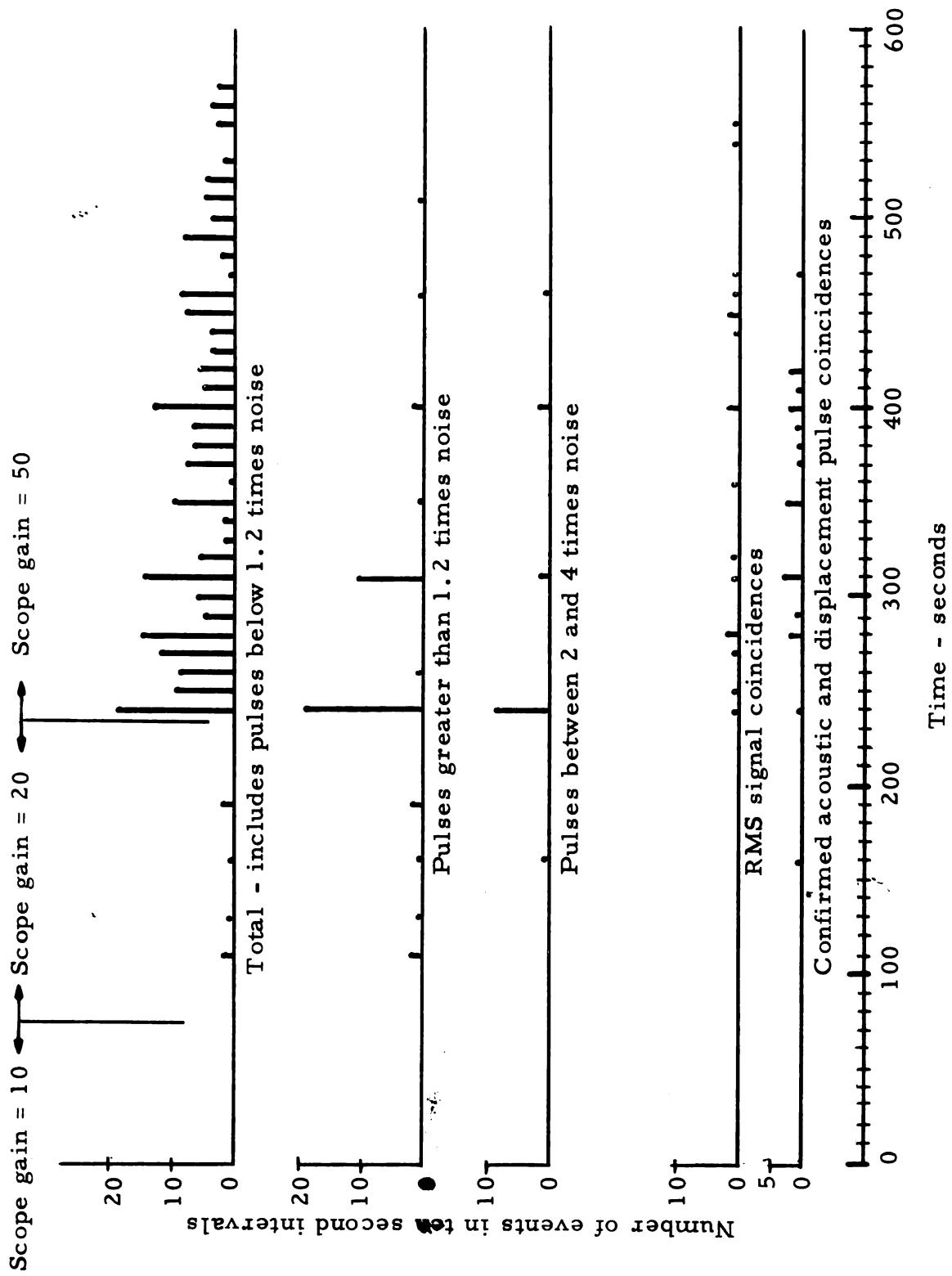Figure 48. Acoustic emission pulse distribution - Type I, Run 3.

117

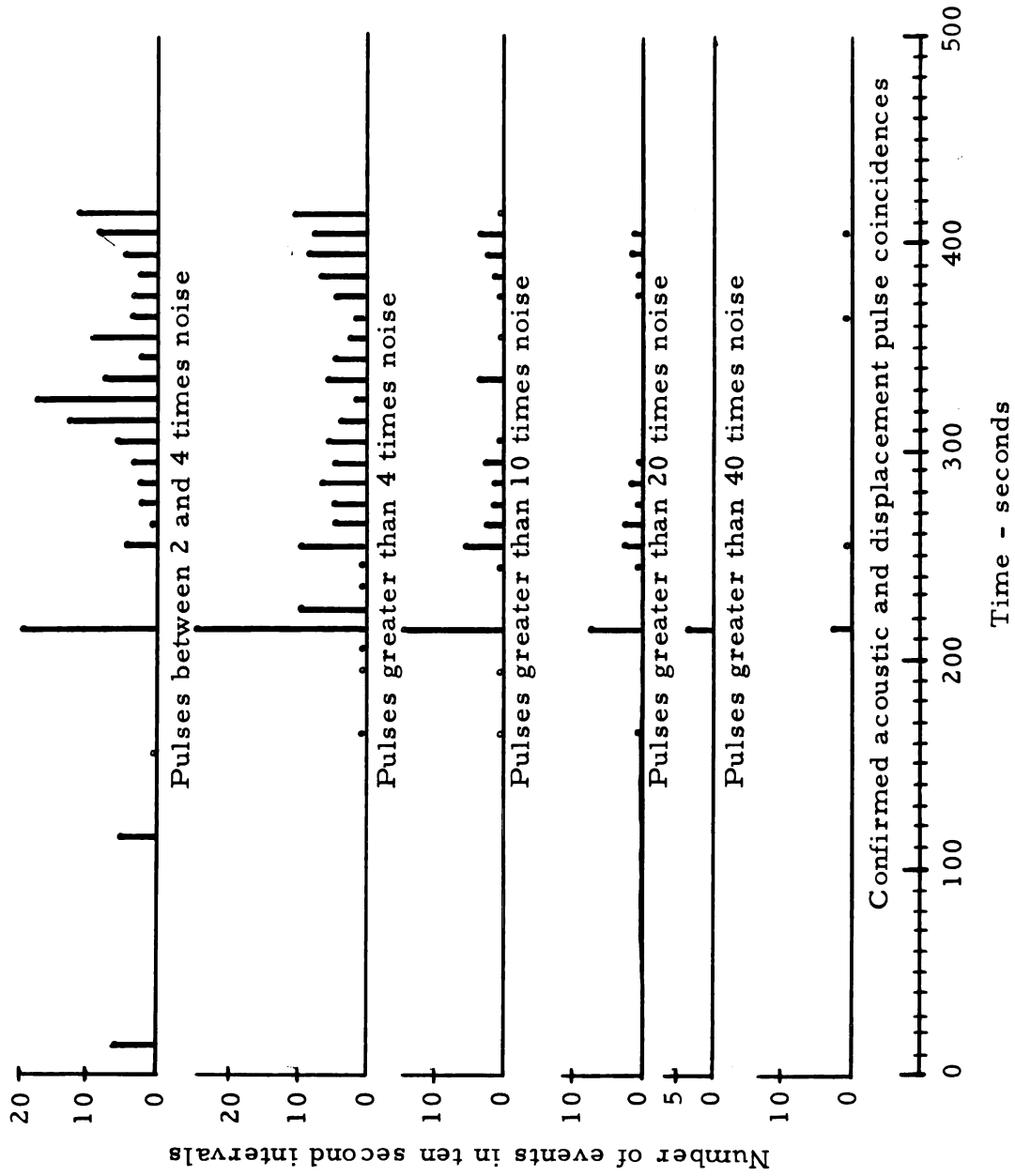Figure 49. Displacement pulse distribution – Type I, Run 3.

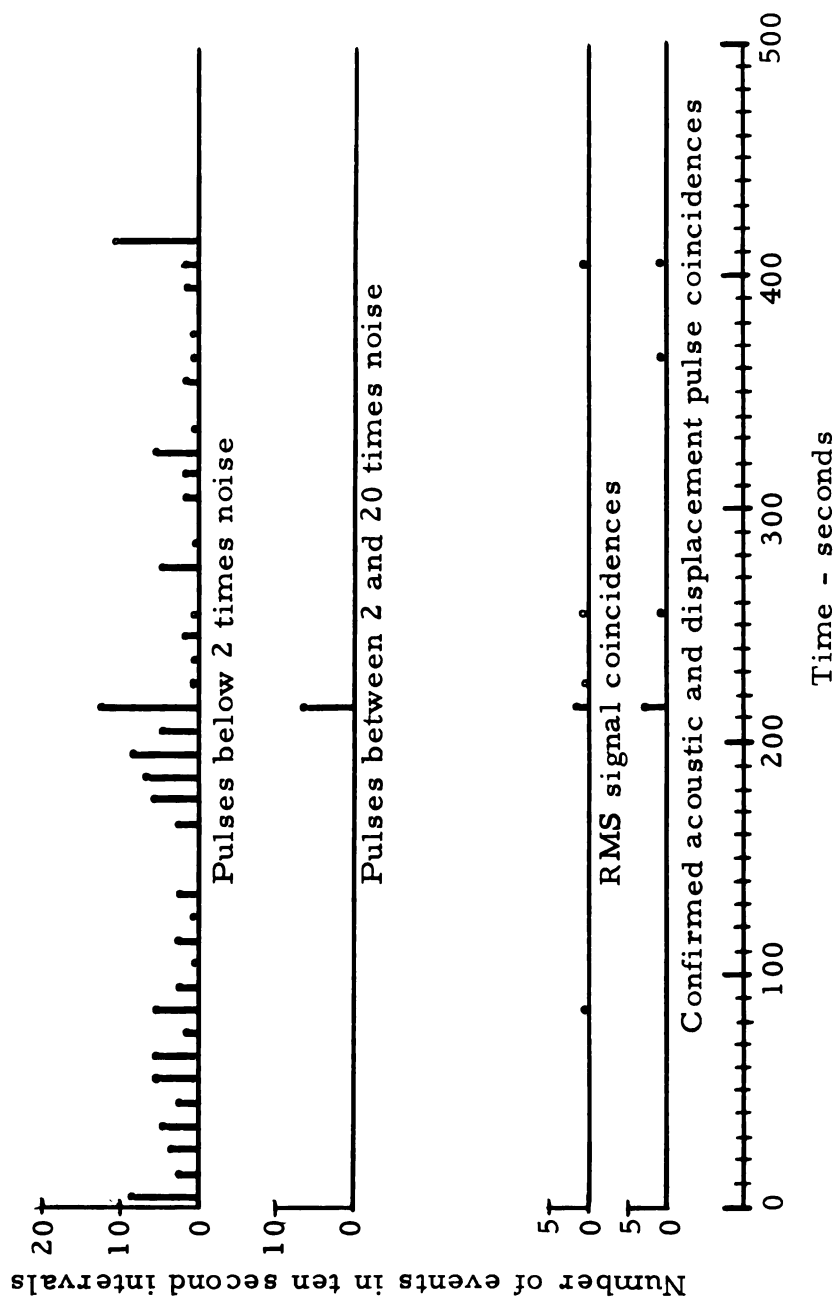Figure 50. Acoustic emission pulse distribution – Type I, Run 4.

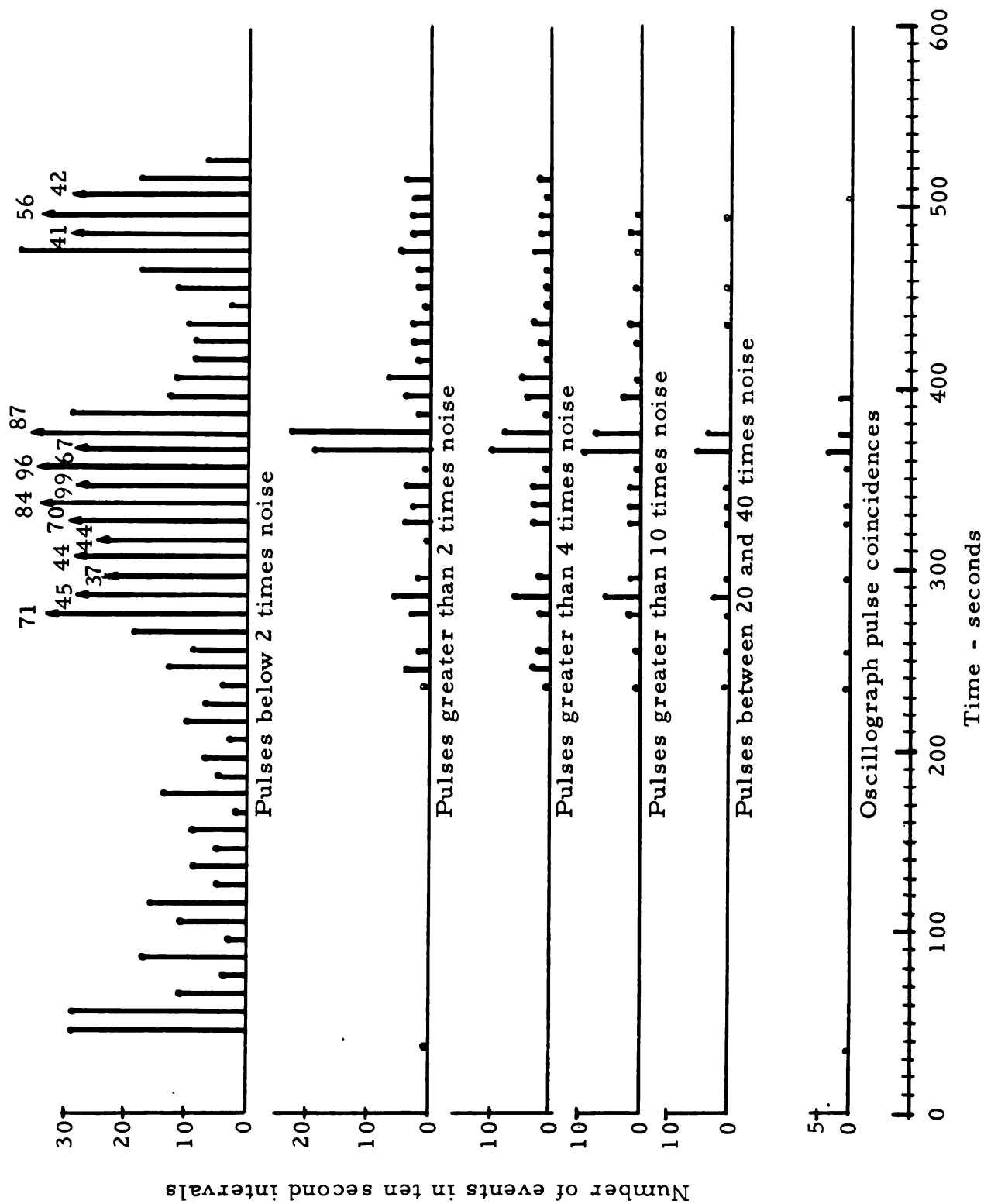Figure 51. Displacement pulse distribution - Type I, Run 4.

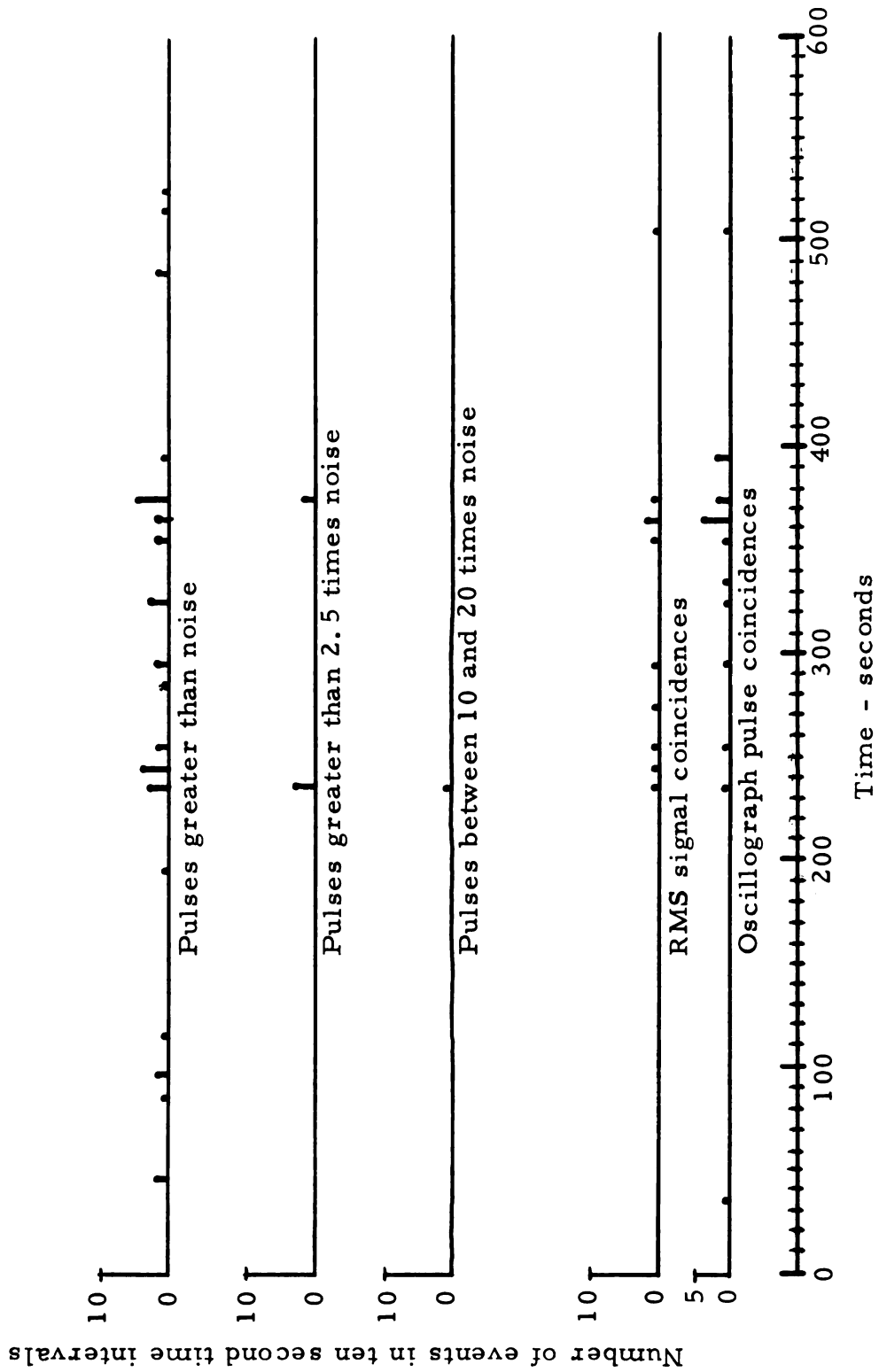Figure 52. Acoustic emission pulse distribution – Type I, Run 9.

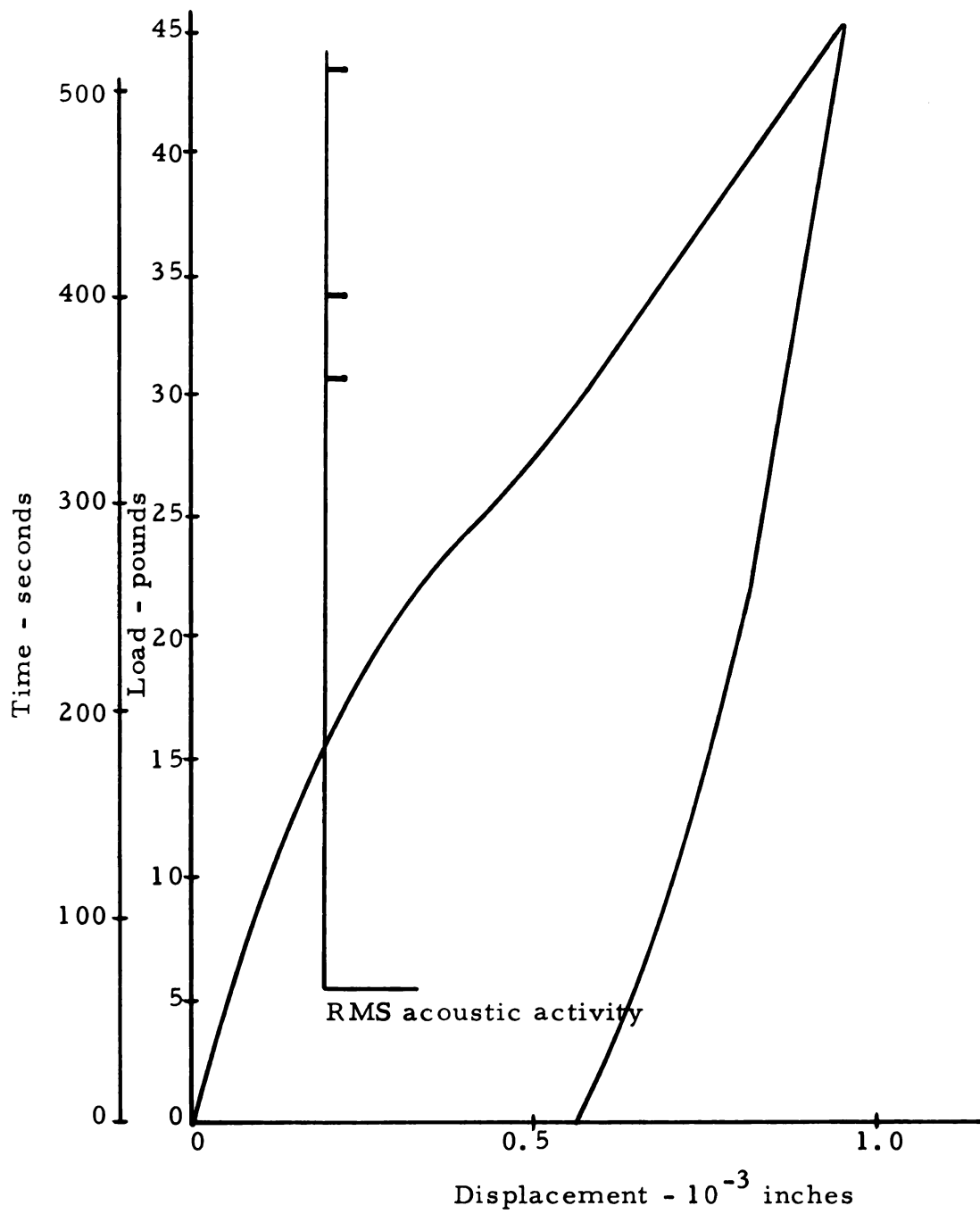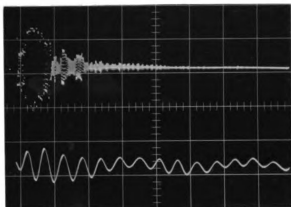Figure 53. Displacement pulse distribution - Type I, Run 9.

Figure 54. Load-displacement and acoustic activity - Type I, Run 10.

Emission   2 volts/cm

5 milliseconds/cm

Displacement 0.1 volts/cm

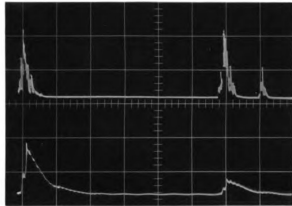Emission 1 volt/cm

5 milliseconds/cm

Displacement 0.01 volts/cm
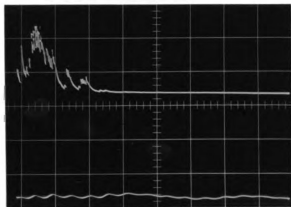
Figure 55. Oscilloscope traces - event at T = 292 seconds.

Emission 2 volts/cm

5 milliseconds/cm

Displacement 0.2 volts/cm
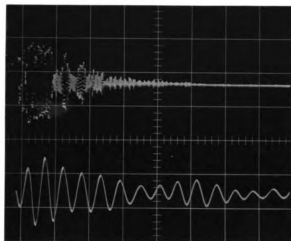
Emission 1 volt/cm

5 milliseconds/cm

Displacement 0.01 volts/cm
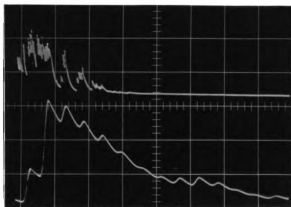
Figure 56. Oscilloscope traces - event at T = 381 seconds.

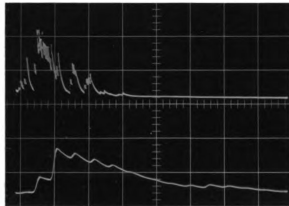Emission 1 volt/cm

140 milliseconds between
large pulses

Displacement 0. 05 volts/cm

Emission 1 volt/cm

5 milliseconds/cm
Leading pulses

Displacement 0. 05 volts/cm

Emission 1 volt/cm

5 milliseconds/cm
Double trace showing all
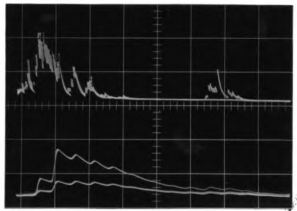three pulses

Displacement 0. 05 volts/cm

Figure 57.   Oscilloscope traces - events at T = 465-7 seconds.

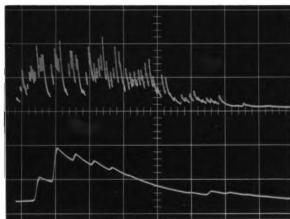Emission 1 volt/cm

5 milliseconds/cm

Displacement 0.2 volts/cm

Figure 58.   Oscilloscope traces - event at T = 478 seconds.